

## **All the Magnetisms and Electricisms in Wiki**

[\*\*http://en.wikipedia.org/wiki/Diamagnetism\*\*](http://en.wikipedia.org/wiki/Diamagnetism)

[\*\*http://en.wikipedia.org/wiki/Superdiamagnetism\*\*](http://en.wikipedia.org/wiki/Superdiamagnetism)

[\*\*http://en.wikipedia.org/wiki/Paramagnetism\*\*](http://en.wikipedia.org/wiki/Paramagnetism)

[\*\*http://en.wikipedia.org/wiki/Superparamagnetism\*\*](http://en.wikipedia.org/wiki/Superparamagnetism)

[\*\*http://en.wikipedia.org/wiki/Ferromagnetism\*\*](http://en.wikipedia.org/wiki/Ferromagnetism)

[\*\*http://en.wikipedia.org/wiki/Superferromagnetism\*\*](http://en.wikipedia.org/wiki/Superferromagnetism)

[\*\*http://en.wikipedia.org/wiki/Antiferromagnetism\*\*](http://en.wikipedia.org/wiki/Antiferromagnetism)

[\*\*http://en.wikipedia.org/wiki/Ferrimagnetism\*\*](http://en.wikipedia.org/wiki/Ferrimagnetism)

[\*\*http://en.wikipedia.org/wiki/Helimagnetism\*\*](http://en.wikipedia.org/wiki/Helimagnetism)

[\*\*http://en.wikipedia.org/wiki/Metamagnetism\*\*](http://en.wikipedia.org/wiki/Metamagnetism)

[\*\*http://en.wikipedia.org/wiki/Mictomagnetism\*\*](http://en.wikipedia.org/wiki/Mictomagnetism)

[\*\*http://en.wikipedia.org/wiki/Spin\\_glass\*\*](http://en.wikipedia.org/wiki/Spin_glass)

[\*\*http://en.wikipedia.org/wiki/Spin\\_ice\*\*](http://en.wikipedia.org/wiki/Spin_ice)

[\*\*http://en.wikipedia.org/wiki/Dielectric\*\*](http://en.wikipedia.org/wiki/Dielectric)

[\*\*http://en.wikipedia.org/wiki/Paraelectricity\*\*](http://en.wikipedia.org/wiki/Paraelectricity)

[\*\*http://en.wikipedia.org/wiki/Ferroelectricity\*\*](http://en.wikipedia.org/wiki/Ferroelectricity)

[\*\*http://en.wikipedia.org/wiki/Antiferroelectricity\*\*](http://en.wikipedia.org/wiki/Antiferroelectricity)

[\*\*http://en.wikipedia.org/wiki/Ferroelectric\\_RAM\*\*](http://en.wikipedia.org/wiki/Ferroelectric_RAM)

# **In 1845, Faraday discovered**

## **Diamagnetism**

dia ( $\delta\iota\alpha$ , across)

**perpendicular to the pole faces**

**parallel to the field lines**

## **Paramagnetism**

para ( $\pi\alpha\rho\alpha$ , beside)

**parallel to the pole faces**

**perpendicular to the field lines**

## **OED:**

**M. Faraday**

**Philosophical Transactions of the Royal Society**

**Volume 146 page 159 (1856)**

**The one form of power possessed by  
paramagnets, diamagnets, and electric  
currents.**

**The phenomena exhibited by a class of bodies, which, when freely suspended and acted on by magnetism, take up a position transverse to that of the magnetic axis, i.e. lie (approximately) east and west; the force to which these phenomena are attributed; the quality of being diamagnetic.**

1 H □ Ferromagnetic □ Antiferromagnetic 2 He

3 Li 4 Be □ Paramagnetic □ Diamagnetic 5 B 6 C 7 N 8 O 9 F 10 Ne

11 Na 12 Mg 13 Al 14 Si 15 P 16 S 17 Cl 18 Ar

19	20	21	22	23	24	25	26	27	28	29	30	31	32	33	34	35	36	
K	Ca	Sc	Ti	V	Cr	Mn	Fe	Co	Ni	Cu	Zn	Ga	Ge	As	Se	Br	Kr	
37	38	39	40	41	42	43	44	45	46	47	48	49	50	51	52	53	54	
Rb	Sr	Y	Zr	Nb	Mo	Tc	Ru	Rh	Pd	Ag	Cd	In	Sn	Sb	Te	I	Xe	
55	56	57		72	73	74	75	76	77	78	79	80	81	82	83	84	85	86
Cs	Ba	La		Hf	Ta	W	Re	Os	Ir	Pt	Au	Hg	Tl	Pb	Bi	Po	At	Rn

87 Fr 88 Ra 89 Ac

↓

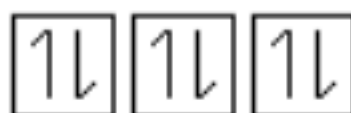
58	59	60	61	62	63	64	65	66	67	68	69	70	71
Ce	Pr	Nd	Pm	Sm	Eu	Gd	Tb	Dy	Ho	Er	Tm	Yb	Lu

## unpaired spins

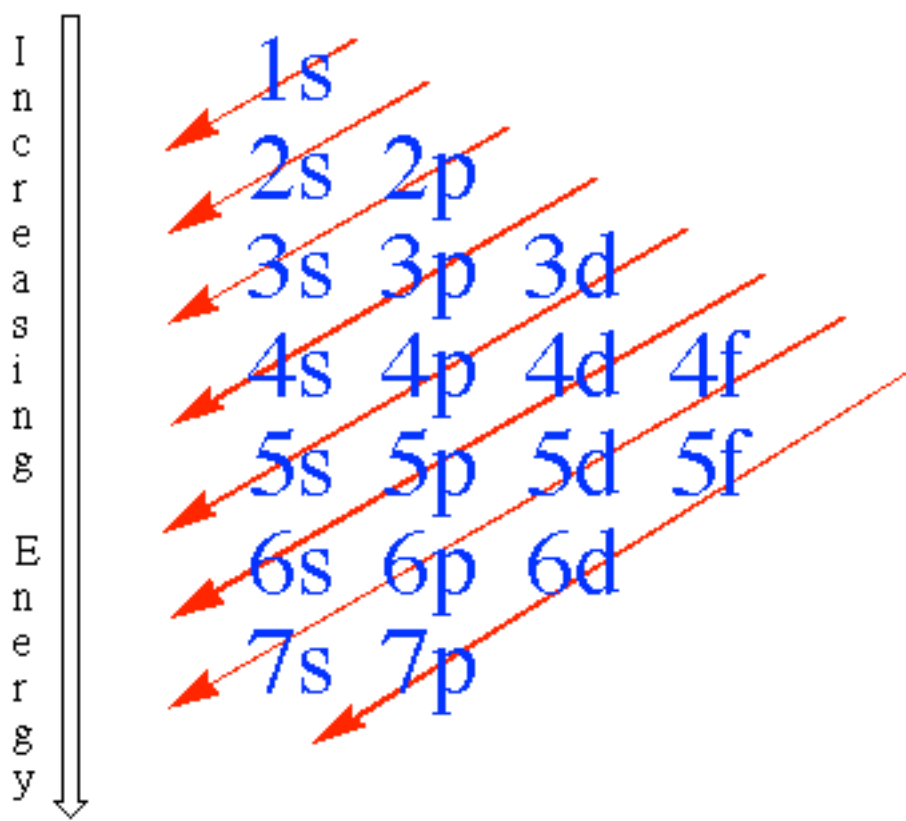


paramagnetic

diamagnetic



## electron filling



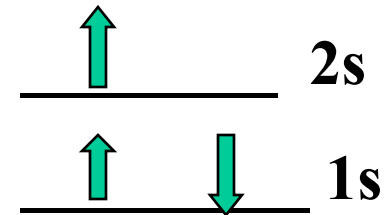
# THE PERIODIC TABLE

- **Magnetism**

A **Paramagnetic** atom is attracted to a magnetic field because it has one or more unpaired electrons.

**Paramagnetic**

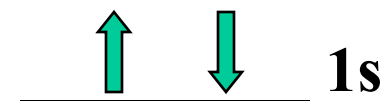
Li



A **Diamagnetic** atom is not attracted to (weakly repelled from) a magnetic field because all of the electrons are paired up.

**Diamagnetic**

He



# “Aufbau” principal

Hydrogen	1s ↑				
Helium	1s ↑ ↓				
Lithium	1s ↑ ↓	2s ↑			
Beryllium	1s ↑ ↓	2s ↑ ↓			
Boron	1s ↑ ↓	2s ↑ ↓	2p <sub>x</sub> ↑		
Carbon	1s ↑ ↓	2s ↑ ↓	2p <sub>x</sub> ↑	2p <sub>y</sub> ↑	
Nitrogen	1s ↑ ↓	2s ↑ ↓	2p <sub>x</sub> ↑	2p <sub>y</sub> ↑	2p <sub>z</sub> ↑
Oxygen	1s ↑ ↓	2s ↑ ↓	2p <sub>x</sub> ↑ ↓	2p <sub>y</sub> ↑	2p <sub>z</sub> ↑
Fluorine	1s ↑ ↓	2s ↑ ↓	2p <sub>x</sub> ↑ ↓	2p <sub>y</sub> ↑ ↓	2p <sub>z</sub> ↑
Neon	1s ↑ ↓	2s ↑ ↓	2p <sub>x</sub> ↑ ↓	2p <sub>y</sub> ↑ ↓	2p <sub>z</sub> ↑ ↓
Sodium	[Neon]	3s ↑			
Magnesium	[Neon]	3s ↑ ↓			
Aluminum	[Neon]	3s ↑ ↓	3p <sub>x</sub> ↑		

## Generally

Minimize number of electrons in each orbital of the same energy

There are five d-orbitals

Transition metals or ion can have 5 unpaired electrons



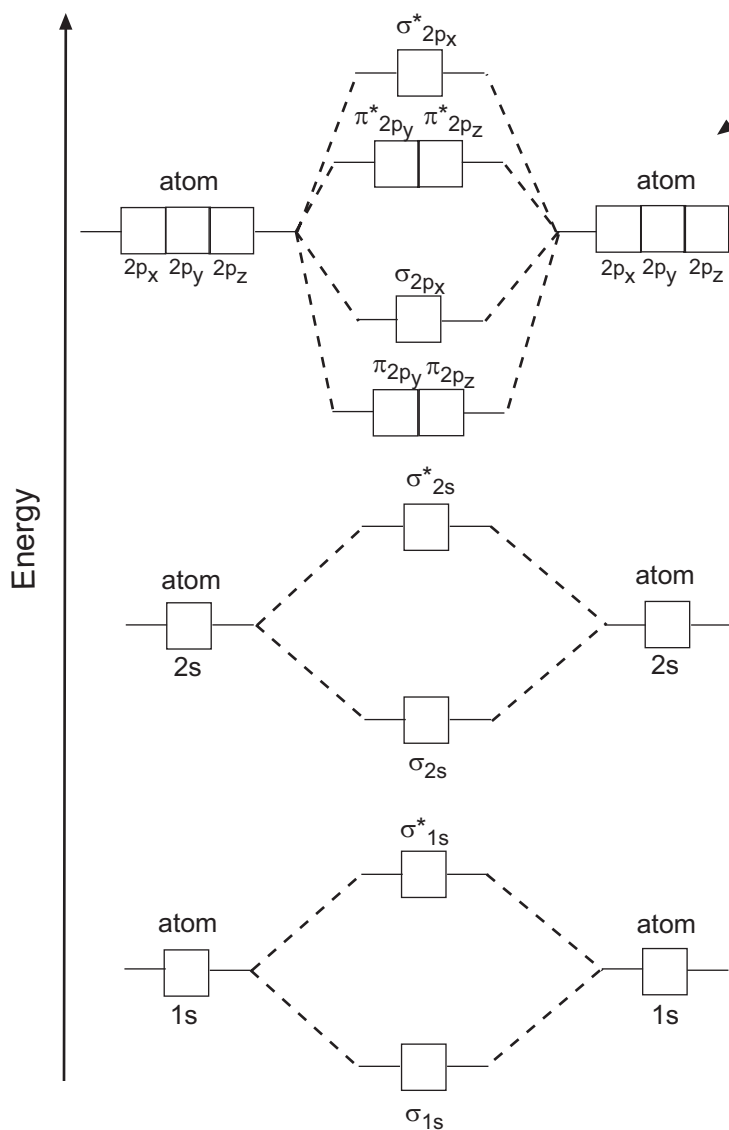
**Molecules: Covalent Bonding--Molecular Orbital Theory: Student Review Notes**

How do you tell if a molecule is paramagnetic or diamagnetic?

How do you tell if a molecule is possible?

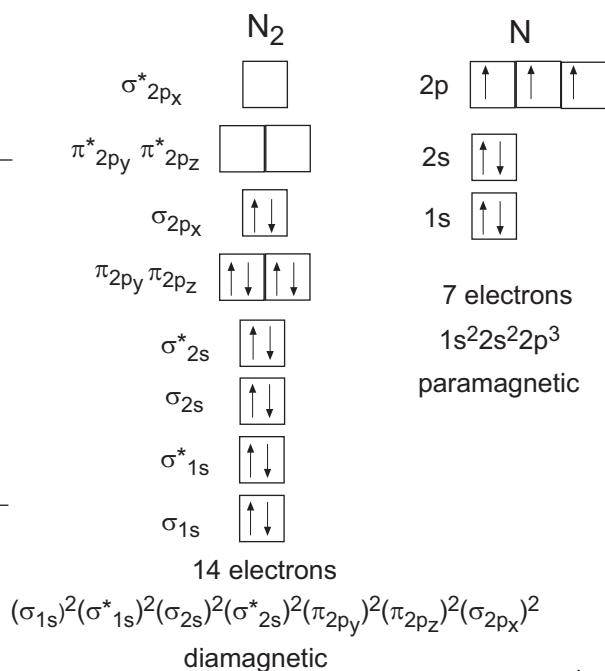
In some cases, valence bond theory cannot account for the observed properties of a molecule. Take diatomic oxygen for example. According to VB theory, each oxygen atom has 3  $sp^2$  hybrid orbitals, there is one sigma-bond formed by the overlap of a pair of  $sp^2$  hybrid orbitals from each atom, one pi-bond formed by the overlap of atomic p-orbitals and each oxygen atom has 2 non-bonding pairs in 2  $sp^2$  hybrid orbitals. From this picture, it appears that all of electrons in the molecule are paired up and therefore the molecule should be diamagnetic. It turns out that molecular oxygen is paramagnetic. VB theory is not complex enough to account for this physical property and here is where molecular orbital theory comes in. The other thing that MO theory is useful for at this level of chemistry, is to predict whether or not a molecule will actually form. This is done via a calculation of the bond order based on an MO diagram.

Molecular orbital theory describes the energy levels of bonding and non-bonding electrons in terms of molecular orbitals that result from the interaction of the atomic orbitals of the bonding atoms. Take a look, you need to understand this picture. It is the **general molecular orbital energy-level diagram for the first two energy levels**. In terms of using it, you just need to now how to make an MO diagram--this is analogous to an atomic orbital diagram, and fill in electrons.



Atomic orbitals combine to yield molecular bonding and antibonding orbitals (the ones with the \*). The bonding orbitals represent the space shared by the bonding atoms in which electrons can be located. The antibonding orbitals (\*) represent the space that is available to the electrons that is not shared by the two atoms in the bond.

It is useful to see the analogy between an MO electron configuration and an atomic electron configuration. Take a look at the MO diagram and electron configuration for molecular  $N_2$  and atomic N.



**Molecules: Covalent Bonding--Molecular Orbital Theory: Student Review Notes**

**Rules for writing the MO diagram for a molecule**

1. The number of molecular orbitals formed is equal to the number of atomic orbitals combined.
2. Filling electrons in the MOs occurs from lowest energy to highest energy.
3. Pauli Exclusion Principle still holds--two electrons per MO.
4. Hund's Rule still holds--use maximum spin multiplicity when filling MOs.
5. The number of electrons in MOs is equal to the sum of all electrons for the bonding atoms.

Okay, so you've seen an example of how to write out an MO diagram to examine the magnetic properties of a molecule. The second place where MO theory is useful to general chemistry is in determining if a molecule will form. At this level of chemistry, you'll typically only see MO questions that deal with diatomic species--i.e. for which it is easy to write out the MO diagram. The stability of a species can be examined by looking at the **Bond Order** of the molecule. Here is the formula,

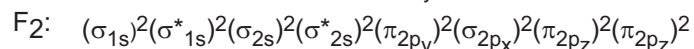
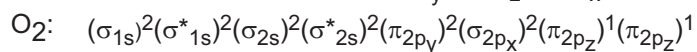
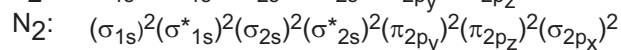
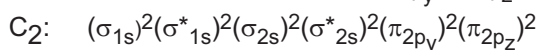
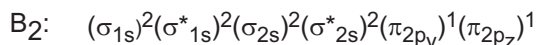
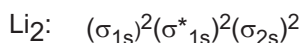
$$\text{Bond Order} = \frac{1}{2} \left[ \text{the sum of electrons in bonding MOs} - \text{the sum of electrons in antibonding MOs} \right]$$

1. A bond order of 0 (zero) means that the molecule cannot exist.
2. You can have fractional bond orders but integer values are more stable.
3. A single bond has order 1, a double bond has order 2, a triple bond has order 3.

Know how to examine the properties of diatomic molecules of the second period elements using MO Theory.

	Li <sub>2</sub>	B <sub>2</sub>	C <sub>2</sub>	N <sub>2</sub>	O <sub>2</sub>	F <sub>2</sub>
σ* <sub>2p<sub>x</sub></sub>	<input type="checkbox"/>	<input type="checkbox"/>	<input type="checkbox"/>	<input type="checkbox"/>	<input type="checkbox"/>	<input type="checkbox"/>
π* <sub>2p<sub>y</sub></sub> π* <sub>2p<sub>z</sub></sub>	<input type="checkbox"/>	<input type="checkbox"/>	<input type="checkbox"/>	<input type="checkbox"/>	<input type="checkbox"/>	<input type="checkbox"/>
σ <sub>2p<sub>x</sub></sub>	<input type="checkbox"/>	<input type="checkbox"/>	<input type="checkbox"/>	<input type="checkbox"/>	<input type="checkbox"/>	<input type="checkbox"/>
π <sub>2p<sub>y</sub></sub> π <sub>2p<sub>z</sub></sub>	<input type="checkbox"/>	<input type="checkbox"/>	<input type="checkbox"/>	<input type="checkbox"/>	<input type="checkbox"/>	<input type="checkbox"/>
σ* <sub>2s</sub>	<input type="checkbox"/>	<input type="checkbox"/>	<input type="checkbox"/>	<input type="checkbox"/>	<input type="checkbox"/>	<input type="checkbox"/>
σ <sub>2s</sub>	<input type="checkbox"/>	<input type="checkbox"/>	<input type="checkbox"/>	<input type="checkbox"/>	<input type="checkbox"/>	<input type="checkbox"/>
σ* <sub>1s</sub>	<input type="checkbox"/>	<input type="checkbox"/>	<input type="checkbox"/>	<input type="checkbox"/>	<input type="checkbox"/>	<input type="checkbox"/>
σ <sub>1s</sub>	<input type="checkbox"/>	<input type="checkbox"/>	<input type="checkbox"/>	<input type="checkbox"/>	<input type="checkbox"/>	<input type="checkbox"/>
No. electrons	6	10	12	14	16	18
Bond Order	1	2	2	3	2	1
Magnetic Props	diamagnetic	paramagnetic	diamagnetic	diamagnetic	paramagnetic	diamagnetic

Electron Configurations:



for O<sub>2</sub> and F<sub>2</sub>, σ<sub>2p<sub>x</sub></sub> is lower in energy than π<sub>2p<sub>y</sub></sub> and π<sub>2p<sub>z</sub></sub>



# Magnetic elements

## Curie Temperature


IUPAC Periodic Table of the Elements

1																	18	
H																	He	
Li	Be	symbol										B	C	N	O	F	Ne	
Na	Mg	AntiFerromagnetic										Al	Si	P	S	Cl	Ar	
K	Ca	Sc	Ti	V	Cr	Mn	Fe	Co	Ni	Cu	Zn	Ga	Ge	As	Se	Br	Kr	
Rb	Sr	Y	Zr	Nb	Mo	Tc	Ru	Rh	Pd	Ag	Cd	In	Sn	Sb	Te	I	Xe	
Cs	Ba	La	Hf	Ta	W	Re	Os	Ir	Pt	Au	Hg	Tl	Pb	Bi	Po	At	Rn	
Fr	Ra	Ac	Rf	Db	Sg	Bh	Hs	Mt	Ds	Uuu								
		La	Ce	Pr	Nd	Pm	Sm	Eu	Gd	Tb	Dy	Ho	Er	Tm	Yb	Lu		
		Ac	Th	Pa	U	Np	Pu	Am	Cm	Bk	Cf	Es	Fm	Md	No	Lr		

Ferromagnetic  
High  $T_C$   
 $T_C > 400^\circ$

AntiFerromagnetic

Ferromagnetic  
Low  $T_C$   
 $T_C \leq rt$



Curie Temperature – Transition temperature above which materials are no longer ferromagnetic

# Magnetic Susceptibilities of Paramagnetic and Diamagnetic Materials at 20°C

Material	$\chi_m = K_m - 1$ ( $\times 10^{-5}$ )
<b>Paramagnetic</b>	
Iron oxide (FeO)	720
Iron amonium alum	66
Uranium	40
Platinum	26
Tungsten	6.8
Cesium	5.1
Aluminum	2.2
Lithium	1.4
Magnesium	1.2
Sodium	0.72
Oxygen gas	0.19
<b>Diamagnetic</b>	
Ammonia	-0.26
Bismuth	-16.6
Mercury	-2.9
Silver	-2.6
Carbon (diamond)	-2.1
Carbon (graphite)	-1.6
Lead	-1.8
Sodium chloride	-1.4
Copper	-1.0
Water	-0.91

[Paramagnetism](#) | [Diamagnetism](#)

Here the quantity  $K_m$  is called the relative permeability, a quantity which measures the ratio of the internal magnetization to the applied magnetic field. If the material does not respond to the magnetic field by magnetizing, then the field in the material will be just the applied field and the relative permeability  $K_m = 1$ . A positive relative permeability greater than 1 implies that the material magnetizes in response to the applied magnetic field. The quantity  $\chi_m$  is called magnetic susceptibility, and it is just the permeability minus 1. The magnetic susceptibility is then zero if the material does not respond with any magnetization. So both quantities give the same information, and both are dimensionless quantities.

For ordinary solids and liquids at room temperature, the relative permeability  $K_m$  is typically in the range 1.00001 to 1.003. We recognize this weak magnetic character of common materials by the saying "they are not magnetic", which recognizes their great contrast to the magnetic response of [ferromagnetic](#) materials. More precisely, they are either paramagnetic or diamagnetic, but that represents a very small magnetic response compared to ferromagnets.

The gases  $N_2$  and  $H_2$  are weakly diamagnetic with susceptibilities  $-0.0005 \times 10^{-5}$  for  $N_2$  and  $-0.00021 \times 10^{-5}$  for  $H_2$ . That is in contrast to the large paramagnetic susceptibility of  $O_2$  in the table.

[Index](#)

[Tables](#)

Reference  
[Young](#)  
Section  
29-8

# Magnetic Properties of Ferromagnetic Materials

Material	Treatment	Initial Relative Permeability	Maximum Relative Permeability	Coercive Force (oersteds)	Remanent Flux Density (gauss)
Iron, 99.8% pure	Annealed	150	5000	1.0	13,000
Iron, 99.95% pure	Annealed in hydrogen	10,000	200,000	0.05	13,000
78 Permalloy	Annealed, quenched	8,000	100,000	.05	7,000
Superpermalloy	Annealed in hydrogen, controlled cooling	100,000	1,000,000	0.002	7,000
Cobalt, 99% pure	Annealed	70	250	10	5,000
Nickel, 99% pure	Annealed	110	600	0.7	4,000
Steel, 0.9% C	Quenched	50	100	70	10,300
Steel, 30% Co	Quenched	...	...	240	9,500
Alnico 5	Cooled in magnetic field	4	...	575	12,500
Silmanal	Baked	...	...	6,000	550
Iron, fine powder	Pressed	...	...	470	6,000

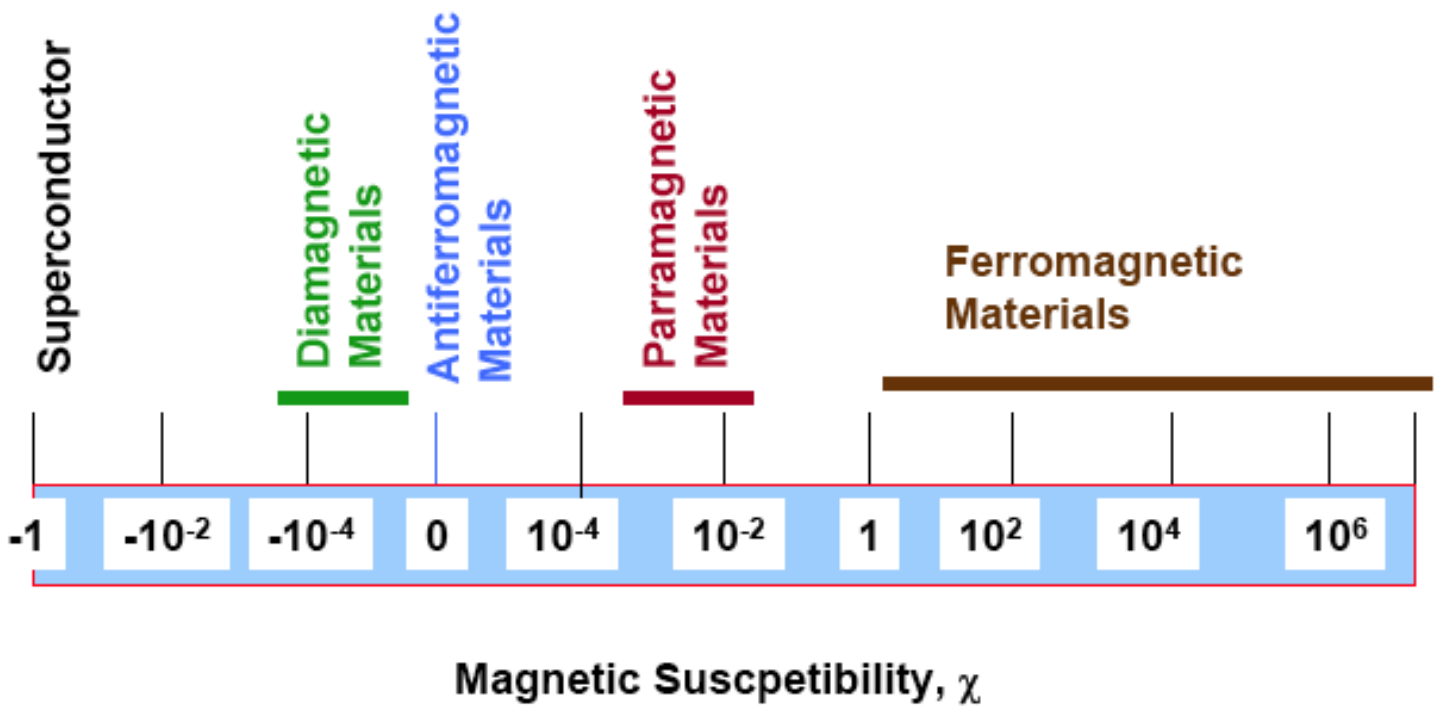
In this table the remanent flux density is the retained [magnetic field](#) B, and the SI unit for B is the Tesla (T). 1 Tesla = 10,000 gauss. The "coercive force" is the applied reverse [magnetic field strength](#) H required to force the net magnetic field back to zero after magnetization. The SI unit for H is A/m, and 1 A/m = 0.01257 oersteds.




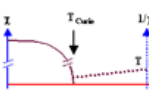

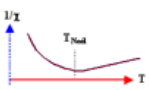

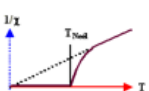
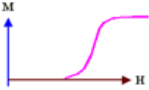
[Discussion of relative permeability](#)

[Coercivity and Remanence](#)

<b>Material</b>	<b>Curie temp. (K)</b>
Fe	1043
Co	1388
Ni	627
Gd	292
Dy	88
MnAs	318
MnBi	630
MnSb	587
CrO <sub>2</sub>	386
MnOFe <sub>2</sub> O <sub>3</sub>	573
FeOFe <sub>2</sub> O <sub>3</sub>	858
NiOFe <sub>2</sub> O <sub>3</sub>	858
CuOFe <sub>2</sub> O <sub>3</sub>	728
MgOFe <sub>2</sub> O <sub>3</sub>	713
EuO	69
Y <sub>3</sub> Fe <sub>5</sub> O <sub>12</sub>	560

# Summary



<p style="text-align: center;"><b>Magnetization</b> <math>M = M(H)</math></p>	<p style="text-align: center;"><b>Magnetic susceptibility</b> <math>c_{\text{mag}} = c_{\text{mag}}(T)</math></p>	<p style="text-align: center;"><b>Remarks</b></p>
		<p>For <b>diamagnets</b> the susceptibility is negative and close to zero; and there is no temperature dependence.</p>
		<p>For <b>paramagnets</b>, the susceptibility is (barely) larger than zero and decreases with <math>T</math>. Plotted as <math>1/c(T)</math> we find a <i>linear</i> relationship.</p>
		<p>For <b>ferromagnets</b> the susceptibility is large; the magnetization increases massively with <math>H</math>. Above a critical temperature <math>T_{\text{Cu}}</math>, the <i>Curie temperature</i>, paramagnetic behavior is observed.</p>
		<p><b>Antiferromagnets</b> are like paramagnets <i>above</i> a critical temperature <math>T_{\text{Ne}}</math> called <b>Neél temperature</b>. Below <math>T_{\text{Ne}}</math> the susceptibility is small, but with a <math>T</math>-dependence quite different from paramagnets.</p>
		<p><b>Ferrimagnets</b> behave pretty much like <i>ferromagnets</i>, except that the effect tends to be smaller. The <math>1/c(T)</math> curve is very close to zero <i>below</i> a critical temperature, also called Neél temperature.</p>
	<p>Just for good measure, the behaviour of one of the more exotic magnetic materials. Shown is a <b>metamagnet</b>, behaving like a <i>ferro</i> magnet, but only <i>above</i> a critical magnetic field strength.</p>	

# **Torn from Today's Headlines**

**Everybody is doing it!**

# Ferroelectric RAM

---

From Wikipedia, the free encyclopedia

*This article is about an information storage medium. For other uses, see [Fram \(disambiguation\)](#).*

**Ferroelectric RAM** (**FeRAM** or **FRAM**<sup>[1]</sup>) is a [random access memory](#) similar in construction to [DRAM](#) but uses a [ferroelectric](#) layer instead of a [dielectric](#) layer to achieve non-volatility. FeRAM is one of a growing number of alternative [non-volatile memory](#) technologies that offer the same functionality as [Flash memory](#). FeRAM advantages over Flash include: lower power usage, faster write performance<sup>[*citation needed*]</sup> and a much greater maximum number (exceeding 10<sup>16</sup> for 3.3 V devices) of write-erase cycles. FeRAM disadvantages are: much lower [storage densities](#) than Flash devices, storage capacity limitations and higher cost.



# Ferroelectric RAM



## FRAM Advantage

### What is FRAM?

FRAM (Ferroelectric Random Access Memory) is a non-volatile memory combining both ROM and RAM advantages in addition to non-volatility features. Its higher speed in write mode, its lower power consumption as well as its higher endurance, make FRAM superior to any other memory type. As a high-speed non-volatile memory, FRAM can be used in the wide range of offerings.

## FRAM Benefits

- High speed
- High security
- Low power consumption
- Minimum 10 year data retention
- High endurance of minimum 10E10
- Random access
- Byte access
- Low cell internal voltage of 5V for 0.5um and 3.3V for 0.35um
- No need for booster circuit for voltage matching with CMOS

## FRAM™ Advantages over EEPROM

### 1. Transaction Time:

- 30,000 times faster than EEPROM
- 1kByte R/W as a general use in transportation (contact-less cards)

### 2. Energy Consumption:

- 100,000 times higher endurance over EEPROM
- Energy Consumption @64Byte Write Cycle

### 3. Endurance:

- 200 times lower power consumption compare to EEPROM
- 1 FRAM Cycle: Read
- 1 EEPROM Cycle: Erase/Write/Read

## FRAM Comparison with other memory products

	<b>FRAM</b>	<b>EEPROM</b>	<b>Flash</b>
Nonvolatile Principle	Ferroelectricity	Charge Storage	Charge Storage
Cell Access Mode	Random	Random	Random & Serial
Read Cycle	85 -110nsec	200nsec	90nsec
Internal Program Voltage	5V/3.3V	18V	12V
Write Cycle	85-110nsec	5msec	1sec
Program Block	Byte	Sector	Sector
Endurance	10 <sup>10</sup>	10 <sup>5</sup>	10 <sup>5</sup>
Data Retention	10 years	10 years	10 years
Scalability	Good	Restricted	Restricted
CMOS Compatibility	Good	Restricted	Restricted

## Ultra-Low Power MCU Uses Ferroelectric Memory Writes 100 times faster than Flash; uses 1/250th of the power.

Charles J. Murray, Senior Technical Editor, *Electronics & Test – Design News*, May 3, 2011

A new ultra-low power microcontroller (MCU) with on-board ferroelectric memory could give a big boost to remote monitoring systems.

# May 3, 2011



TI's FRAM microcontroller writes 100 times faster than Flash and uses 1/250th of the power. Source: Texas Instruments

Known as the **MSP430FR57xx**, the new microcontroller is said to be the industry's first ultra-low power ferroelectric random access memory (FRAM) 16-bit microcontroller. Texas Instruments has been working on FRAM technology for about a decade, but this is the first time that the memory has been integrated into a microcontroller. The new MCU is said to reduce the industry's best active power by up to 50 percent when executing code from FRAM, operating at 100  $\mu\text{A}/\text{MHz}$  in active mode and 3  $\mu\text{A}$  in real-time clock mode. It also offers virtually limitless write endurance at 100 trillion cycles.

For product designers, the new technology provides the ability to deploy and monitor sensors for years at a time. TI engineers foresee it being used on many of the country's 600,000 bridges, or on other types of remote structures where safety and security is critical.

"Imagine employing underwater seismic sensors for years at a time, so we can identify seismic threats and get notifications out faster," Adair says. "You could also use it for asset tracking, or you could monitor pharmaceuticals from the day they leave the factory until the day they hit your medicine cabinet."

The new microcontroller, introduced at the **Embedded Systems Conference** here, could be especially important for monitoring of bridges, buildings and other remote structures. It also could make it easier for manufacturers to track products, such as pharmaceuticals, as they get shipped around the world.

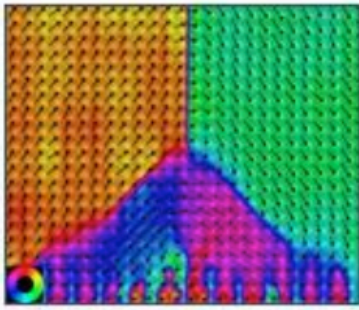
"It's going to allow you to put more sensors in more places and monitor more things," notes Miller Adair, MSP430 product marketing manager for **Texas Instruments**, maker of the new microcontroller. "The key is the fact that FRAM writes 100 times faster than Flash (memory) and gives you a 250-times power savings. So you can do significantly more things with the same battery than you could with a Flash controller."

Known as the **MSP430FR57xx**, the

# Discovery Could Lead to Better Memory Chips

Tuesday, April 19, 2011 | University of Michigan

## April 19, 2011



Engineering researchers at the University of Michigan have found a way to improve the performance of ferroelectric materials, which have the potential to make memory devices with more storage capacity than magnetic hard drives and faster write speed and longer lifetimes than flash memory.

In ferroelectric memory the direction of molecules' electrical polarization serves as a 0 or a 1 bit. An electric field is used to flip the polarization, which is how data is stored.

With his colleagues at U-M and collaborators from Cornell University, Penn State University, and University of Wisconsin, Madison, Xiaoqing Pan, a professor in the U-M Department of Materials Science and Engineering, has designed a material system that spontaneously forms small nano-size spirals of the electric polarization at controllable intervals, which could provide natural budding sites for the polarization switching and thus reduce the power needed to flip each bit.

"To change the state of a ferroelectric memory, you have to supply enough electric field to induce a small region to switch the polarization. With our material, such a nucleation process is not necessary," Pan said. "The nucleation sites are intrinsically there at the material interfaces."

To make this happen, the engineers layered a ferroelectric material on an insulator whose crystal lattices were closely matched. The polarization causes large electric fields at the ferroelectric surface that are responsible for the spontaneous formation of the budding sites, known as "vortex nanodomains."

The researchers also mapped the material's polarization with atomic resolution, which was a key challenge, given the small scale. They used images from a sub-angstrom resolution transmission electron microscope at Lawrence Berkeley National Laboratory. They also developed image processing software to accomplish this.

"This type of mapping has never been done," Pan said. "Using this technique, we've discovered unusual vortex nanodomains in which the electric polarization gradually rotates around the vortices."

A paper on the research, titled "Spontaneous Vortex Nanodomain Arrays at Ferroelectric Heterointerfaces" is available online at NanoLetters.

This research is funded by the Department of Energy, the National Science Foundation and the U.S. Army Research Office.

# Novel Properties of Ferroelectrics to Drive Nanoelectronics and Electronic Memory Storage Research

Published on April 29, 2011 at 12:41 AM

**April 29, 2011**

By Cameron Chai

**A new research on the innovative characteristics of ferroelectrics made at the Department of Energy's Oak Ridge National Laboratory (ORNL) has revealed the source of dynamic conductivity of the domain walls of ferroelectrics.**

The research team was headed by Peter Maksymovych and their findings were published in the Nano Letters of American Chemical Society.

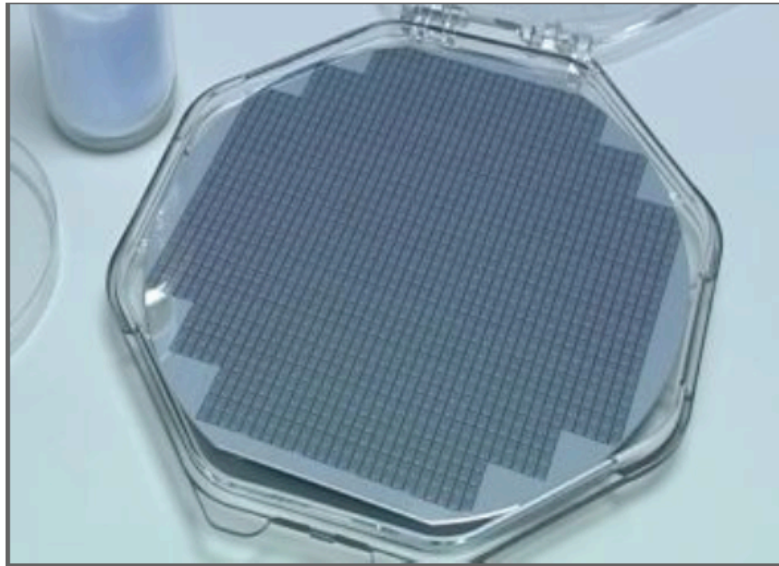
Domain walls are the divisional areas between contrasting polarization states in ferroelectric substances. The domain walls are known to be conductors, yet their source of the conductivity has not been understood. Maksymovych has stated that their measurements recognized that mild and microscopically reversible deformations present in the domain wall offer dynamic conductivity to the walls. He added that the domain wall does not serve as an ideal conductor when placed in its equilibrium position. When an electric field is applied, it gets deformed and turns out to be a dynamic conductor.

Ferroelectrics are a novel group of materials that react to electric field by altering their polarization microscopically. They are used in several applications like medical imaging, sensors, fuel injectors and sonar. Scientists are working on deploying ferroelectric materials in fields like nanoelectronics and memory storage. Obtaining a comprehensive understanding regarding conductivity of domain walls is a critical footstep towards improving these applications.

Maksymovych has mentioned that their research has revealed for the first time that the dynamics of domain walls serves as a major origin of the performance of memory. He added that the tunable conductivity level in the domain wall can serve as a dynamic memory element.

The adaptability of the domain wall signifies its deferred reaction to variations in conductivity and closing down an electric field does not result in a sudden fall in conductance. The previous conductance level will be remembered by the domain wall for a particular span of time, followed by relaxation to its initial state. This type of behavior is termed as memristance. Conventional electronics depends on silicon transistors that serve as on-off switches during the application of electric fields.

According to Maksymovych, their new breakthrough discovery in electronics offers a possible substitute to silicon and will not serve as a path to contend with silicon. The research team worked on samples of bismuth ferrite and they hope that the discovered characteristics of the domain walls will be same for other ferroelectric materials as well. Sergei Kalinin, ORNL Co-author, has stated that the memristive phenomenon is expected to be common in ferroelectric domain walls of multiferroics as well as semiconducting ferroelectrics.



### **Abstract:**

There is a big demand for flash memories that can store even more data. However, it is now necessary to use new materials and technologies to improve flash memories and researchers worldwide are trying different approaches to achieve this aim. The project REALISE has developed a material and a processing technique now ready for industrial application

## **Different approaches to increase the storage capacity of flash memories**

Italy | Posted on April 19th, 2011

**April 19, 2011**

Researchers are investigating different ways to increase the storage capacity of the computer storage chips called flash memories. Within the EU-funded project REALISE (Rare earth oxide atomic layer deposition for innovations in electronics), coordinated by Tyndall National Institute in Ireland, scientists are developing flash memories with improved storage capacity. To achieve this improvement new materials have to be introduced.

In REALISE low-cost rare earth oxides form very good electronic insulators, which are reducing the interference between adjacent memory cells. The scientists have made an insulator, containing zirconium oxide and a smaller amount of lanthanum oxide, named LZO. This structure will respond heavily to electric fields. Through electrical tests the scientists found that nanometer-thin films of LZO with a designed structure showed a three-fold improvement, in insulating properties of importance, compared to alumina. Alumina was earlier the best material in this regard. This result means that it is possible to manufacture electronic devices three times smaller than before and the working lifetime is doubled. The researchers use a process called ALD, atomic layer deposition, to put the rare earth oxides atom by atom onto the flash memories and integrate them properly.

Another way towards better memory chips having longer lifetimes and faster write speed than today's flash memories is investigated by scientists from University of Wisconsin-Madison, Nanjing University, University of Michigan, Penn State University and Cornell University. They are improving ferroelectric materials' performance through a system that, in a spontaneous manner, forms nanosized spirals of the electric polarization at controllable intervals, which could give the polarization switching natural budding sites. This would decrease the power necessary to flip each bit. Researchers at the Chung Hua University, the Industrial Technology Research Institute and the National Chiao Tung University in Taiwan have instead worked on highly thermal stable iridium nanocrystals embedded in SiO<sub>2</sub> matrix, which they suggest could improve the performance of flash memories.

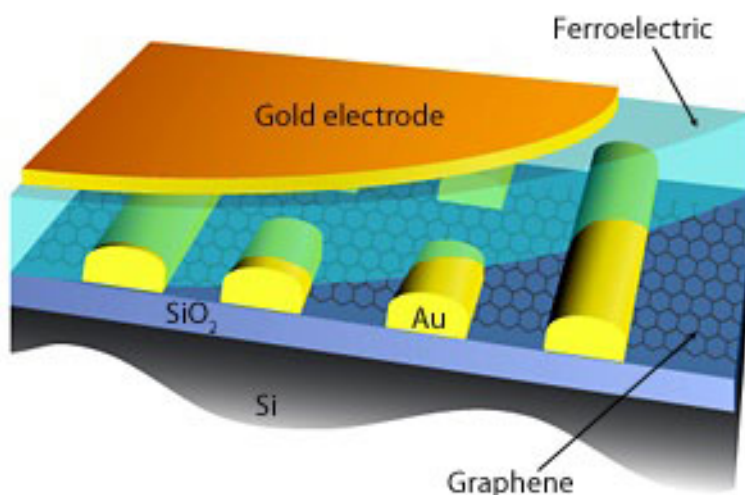
We will soon be able to store much more on our flash memories if everything goes according to plans. The REALISE project's researchers anticipate that if a large flash memory producer uses LZO for making flash memories better, these devices may be on the market within a few years.

# February 16, 2011

Posted: Feb 16th, 2011

## Data storage: Carbon-ferroelectric memory

(*Nanowerk News*) A fundamental component of a field-effect transistor (FET) is the gate dielectric, which determines the number of charge carriers—electrons or electron vacancies—that can be injected into the active channel of the device. Graphene has recently become the focus of attention as a viable, high-performance replacement for silicon in FETs, and in recent studies on graphene-based FETs, scientists have investigated the use of thin films of a ferroelectric material for the gate dielectric. Such films offer several interesting advantages for use in graphene-based FETs: their strong electrical polarization makes it possible to introduce a much higher density of carriers than can be achieved using standard dielectrics, and they have remnant electric polarization—a property that could allow graphene-ferroelectric FETs to be used for nonvolatile memory by storing a certain level of carrier density in the absence of an electrical field.



*Schematic illustration of an improved graphene-ferroelectric FET with SiO<sub>2</sub> basal layer.*

Two collaborating teams from the A\*STAR Institute of Materials Research and Engineering and the National University of Singapore, led by Kui Yao and Barbaros Özyilmaz, respectively, previously demonstrated a basic graphene-ferroelectric memory device in which the polarization in the ferroelectric film was controlled by the electrical bias applied to the gate terminal. In that structure, a thin ferroelectric film was deposited on top of a graphene layer, where it injects charge carriers and thus modulates the resistance of the graphene. Unfortunately, however, the two distinct resistance states that could be read as an information bit could only be realized by polarizing and depolarizing the ferroelectric film, which presented problems due to the instability of the depolarization state.

# Memristor

From Wikipedia, the free encyclopedia

**Memristor** (pronounced /ˈmɛmrɪstər/; a portmanteau of "memory resistor") is a name of passive two-terminal circuit elements in which there is a functional relationship between charge and magnetic flux linkage. Memristor theory was formulated and named by Leon Chua in a 1971 paper.<sup>[3]</sup> In 2008, a team at HP Labs announced the development of a switching memristor based on a thin film of titanium dioxide.<sup>[4]</sup> It has a regime of operation with an approximately linear charge-resistance relationship as long as the time-integral of the current stays within certain bounds.<sup>[5][6][7][8]</sup> These devices are being developed for application in nanoelectronic memories, computer logic, and neuromorphic computer architectures.<sup>[4]</sup>

## Theory

[\[edit\]](#)

The memristor is essentially a two-terminal variable resistor, with resistance dependent upon the amount of charge *q* that has passed between the terminals.

$$V = I \cdot M(q)$$

To relate the memristor to the resistor, capacitor, and inductor, it is helpful to isolate the term *M(q)*, which characterizes the device, and write it as a differential equation.

Device	Characteristic property (units)	Differential equation
<span>Resistor</span>	Resistance (V per A, or <span>ohm</span> , Ω)	$R = dV / dI$
<span>Capacitor</span>	Capacitance (C per V, or <span>farad</span> )	$C = dQ / dV$
<span>Inductor</span>	Inductance (Wb per A, or <span>henry</span> )	$L = d\Phi_m / dI$
Memristor	Memristance (Wb per C, or <span>chua</span> )	$M = d\Phi_m / dQ$

$$V(t) = M(q(t))I(t)$$

# BASIC EQUATIONS OF ELECTRODYNAMICS

---

## Maxwell's Equations

*In general :*

$$\left\{ \begin{array}{l} \nabla \cdot \mathbf{E} = \frac{1}{\epsilon_0} \rho \\ \nabla \times \mathbf{E} = -\frac{\partial \mathbf{B}}{\partial t} \\ \nabla \cdot \mathbf{B} = 0 \\ \nabla \times \mathbf{B} = \mu_0 \mathbf{J} + \mu_0 \epsilon_0 \frac{\partial \mathbf{E}}{\partial t} \end{array} \right.$$

*In matter :*

$$\left\{ \begin{array}{l} \nabla \cdot \mathbf{D} = \rho_f \\ \nabla \times \mathbf{E} = -\frac{\partial \mathbf{B}}{\partial t} \\ \nabla \cdot \mathbf{B} = 0 \\ \nabla \times \mathbf{H} = \mathbf{J}_f + \frac{\partial \mathbf{D}}{\partial t} \end{array} \right.$$

## Auxiliary Fields

*Definitions :*

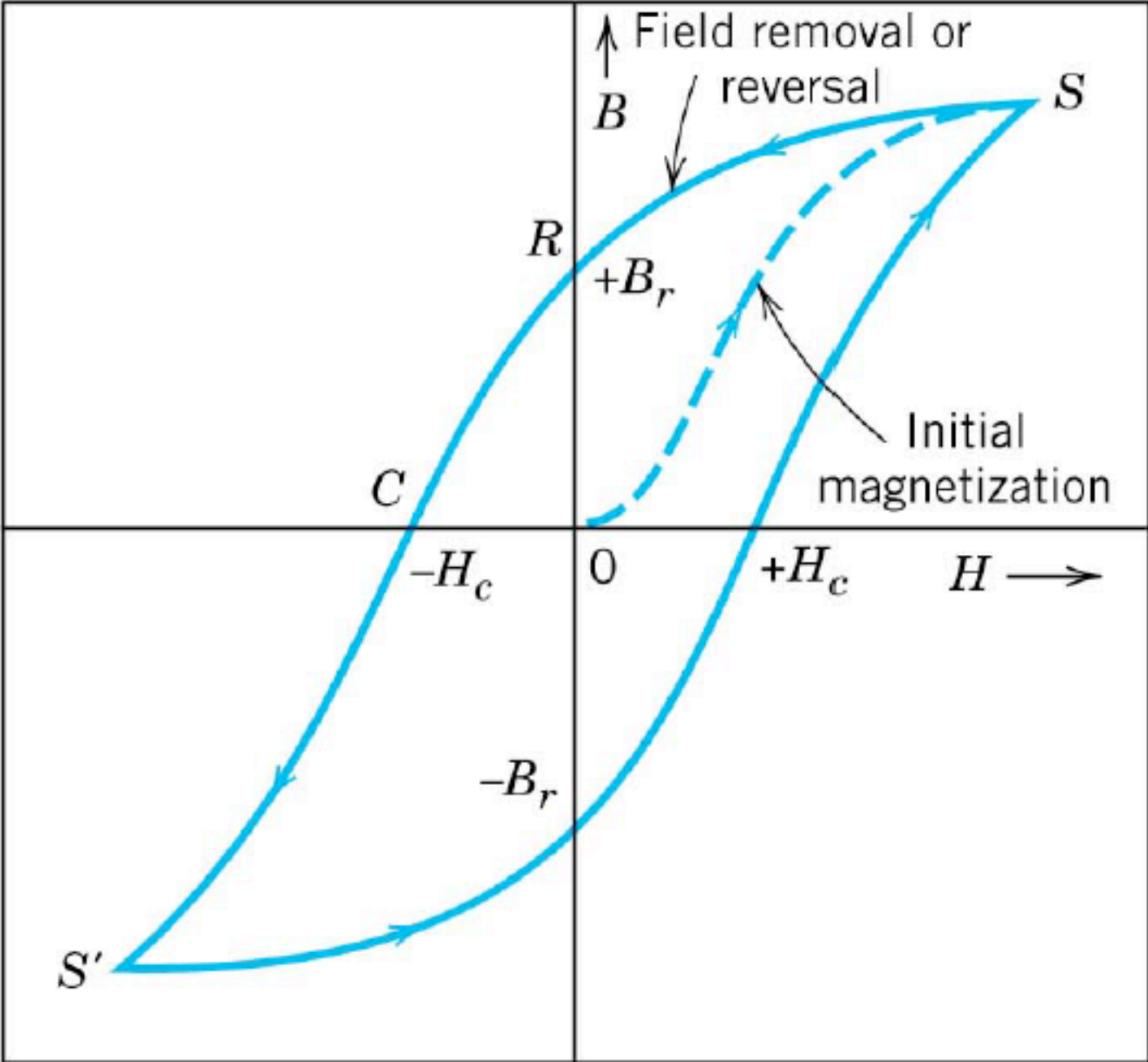
$$\left\{ \begin{array}{l} \mathbf{D} = \epsilon_0 \mathbf{E} + \mathbf{P} \\ \mathbf{H} = \frac{1}{\mu_0} \mathbf{B} - \mathbf{M} \end{array} \right.$$

*Linear media :*

$$\left\{ \begin{array}{l} \mathbf{P} = \epsilon_0 \chi_e \mathbf{E}, \quad \mathbf{D} = \epsilon \mathbf{E} \\ \mathbf{M} = \chi_m \mathbf{H}, \quad \mathbf{H} = \frac{1}{\mu} \mathbf{B} \end{array} \right.$$

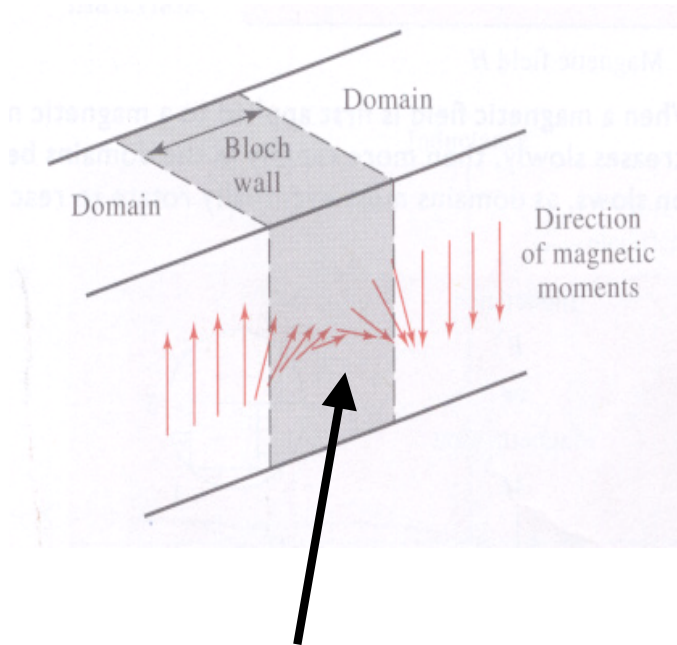


# Simple Magnetic Hysteresis



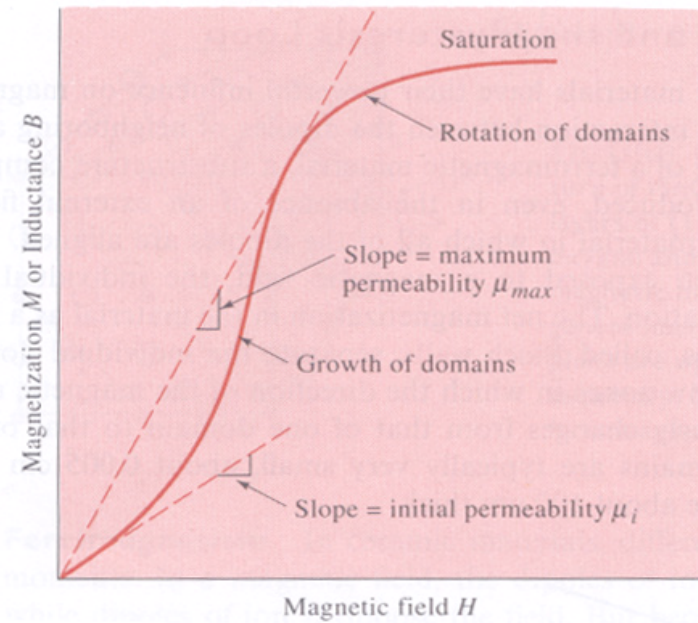
## Theory and Principle

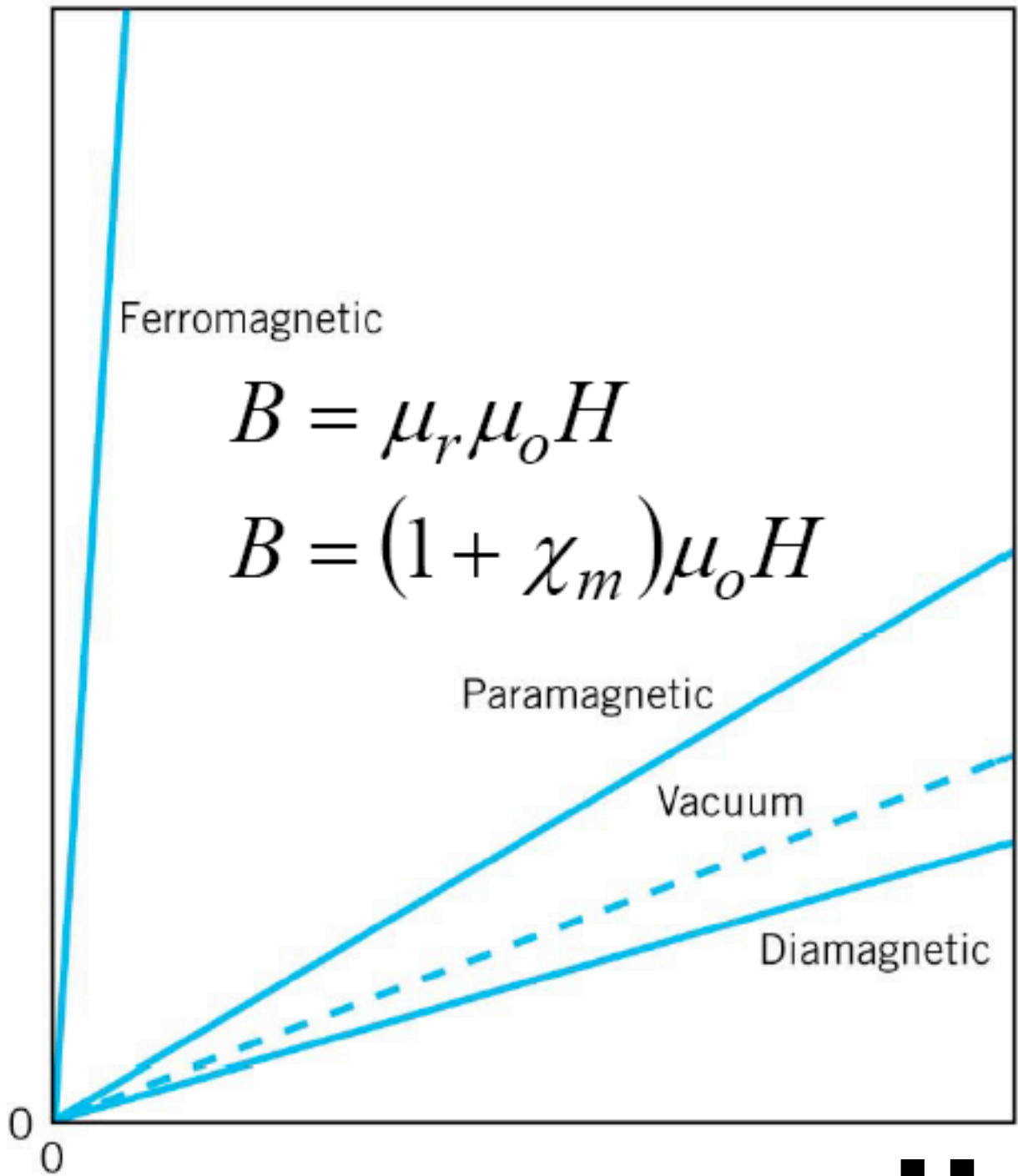
### □ B-H curve



The magnetic moments change direction continuously for ferromagnetic material

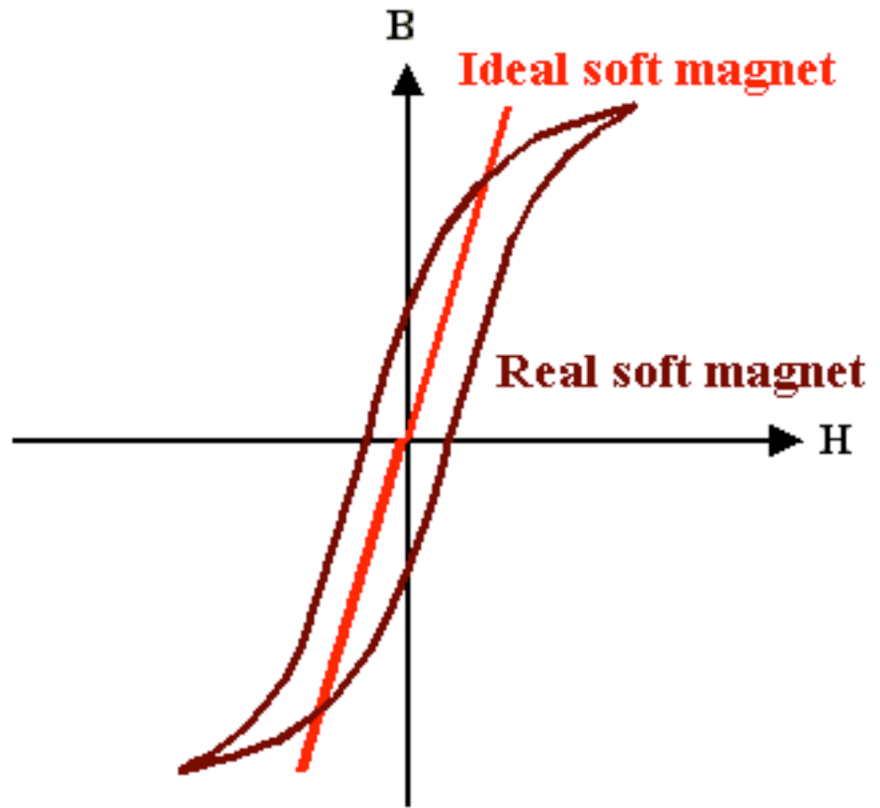
### B-H curve



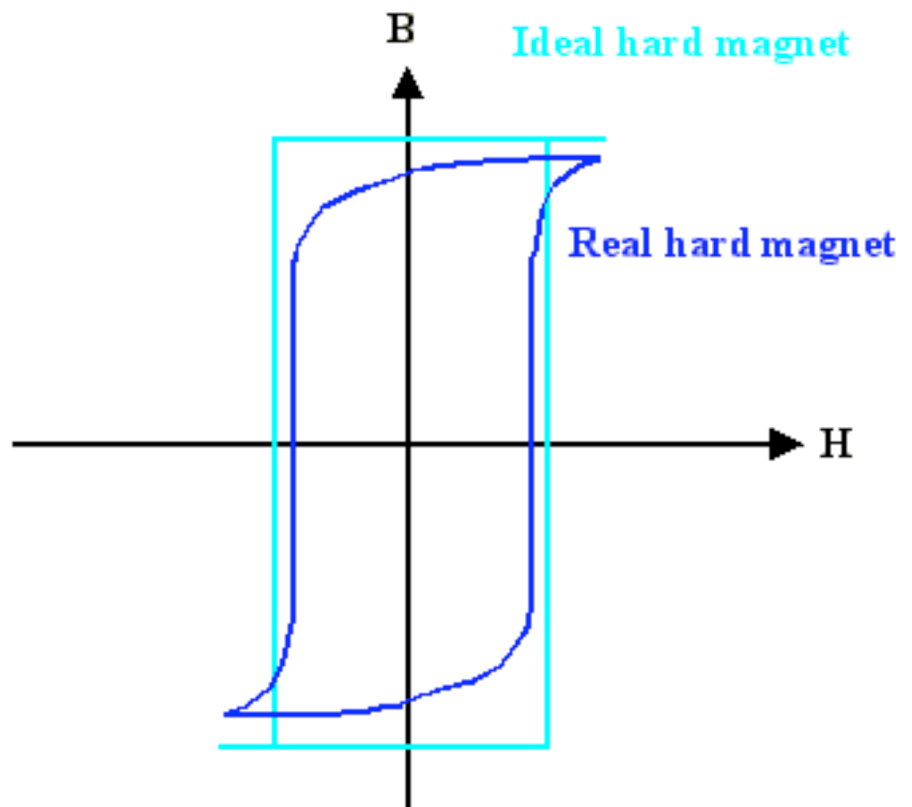
**B****0****H**

# Two kinds of magnets:

## Soft Magnets

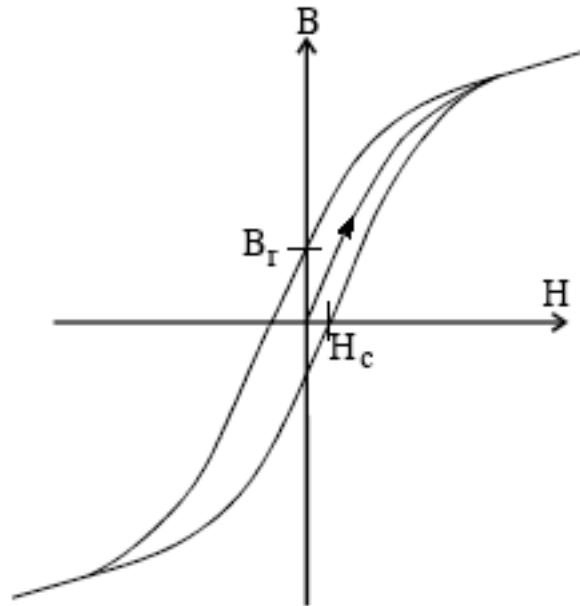


## Hard Magnets

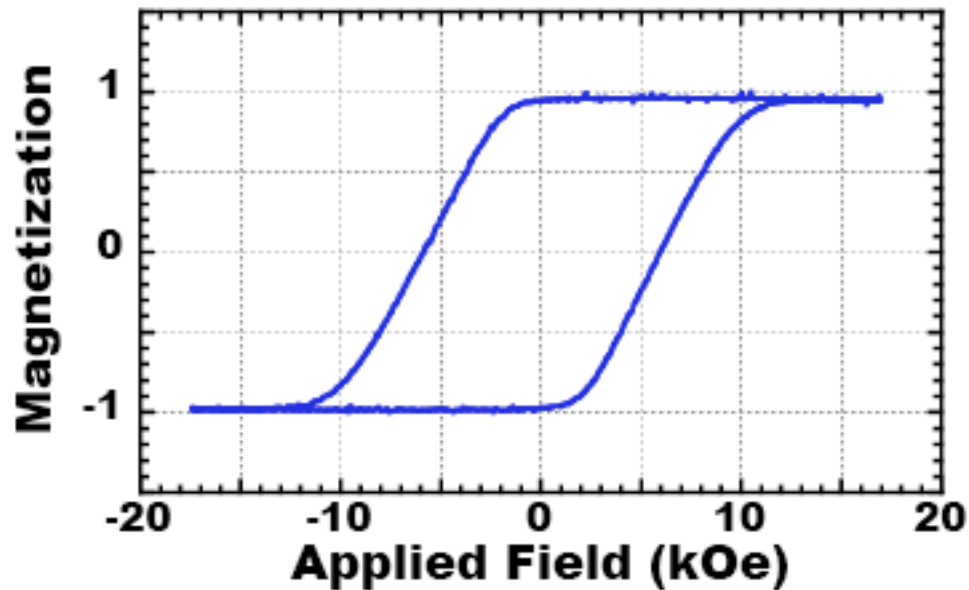


# Two kinds of plots:

## B versus H



## M versus H



# **Different Applications:**

## **Soft Magnets:**

**Need small energy loss**

**transformers**

**electric motors**

**electric generators**

**electromagnets**

## **Hard Magnets**

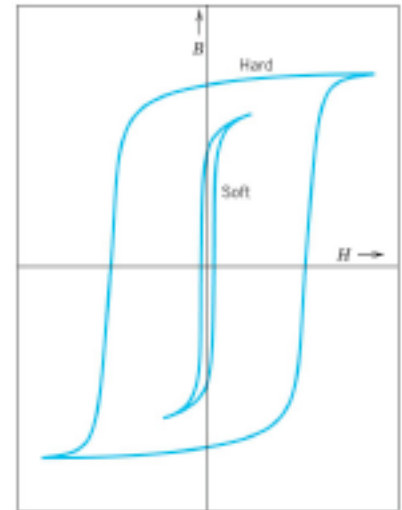
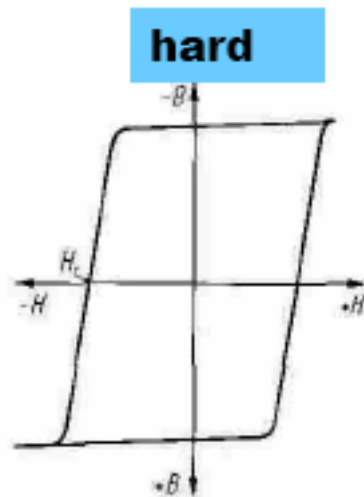
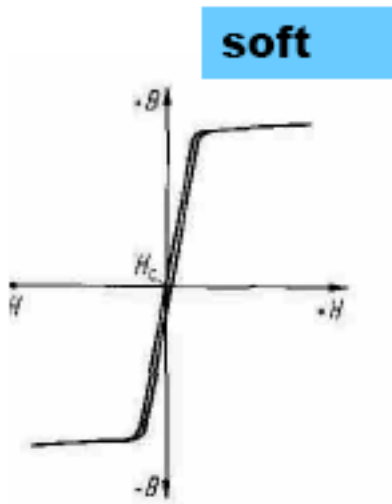
**Need remnance**

**magnetic recording**

**permanent magnets**

**motors and actuators**

# Two Important Ideas: Coercivity and Remnance



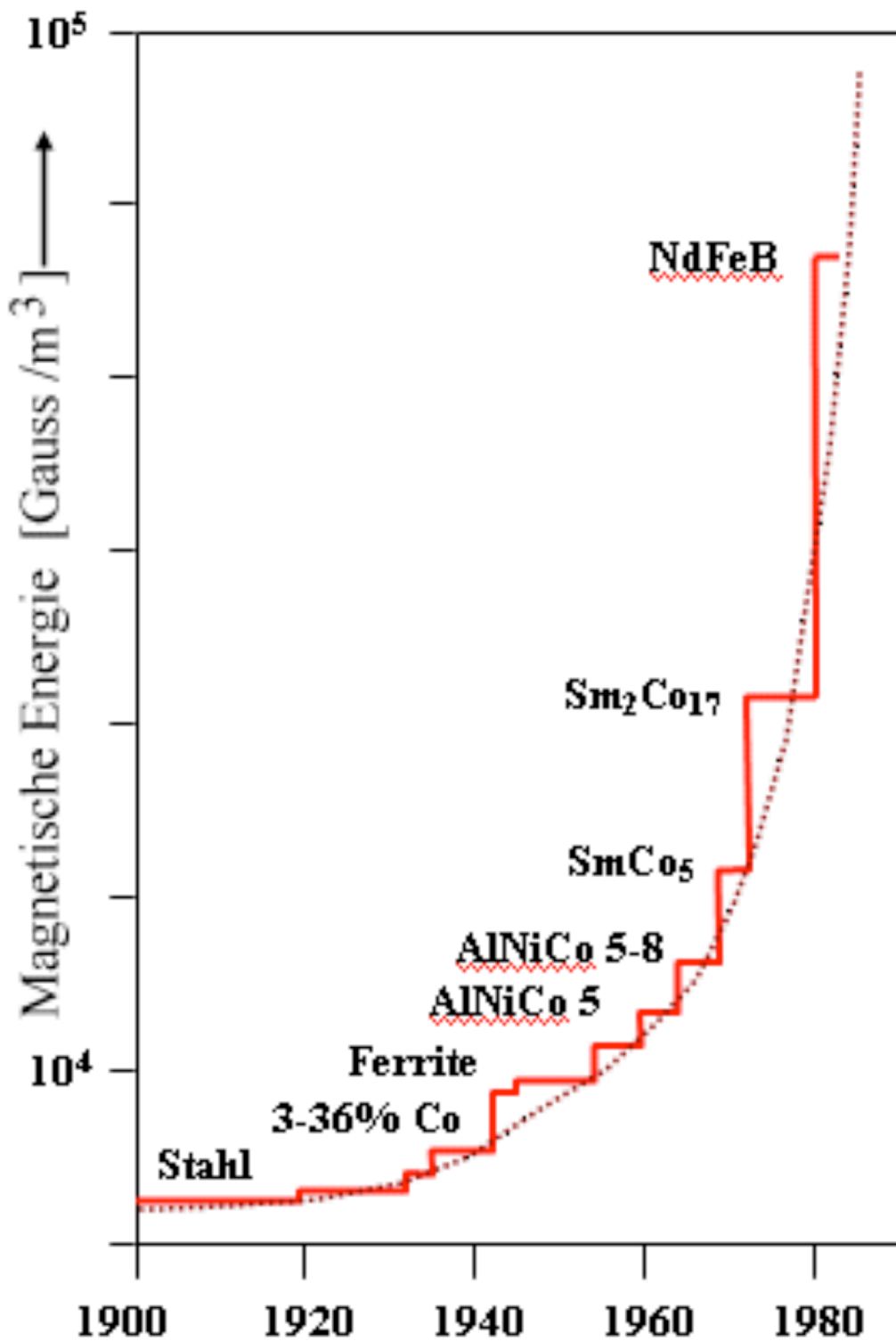
**Soft = Low  
Remnance**

**Hard = High  
Remnance and  
High Coercivity**

**Soft = Low  
Coercivity**

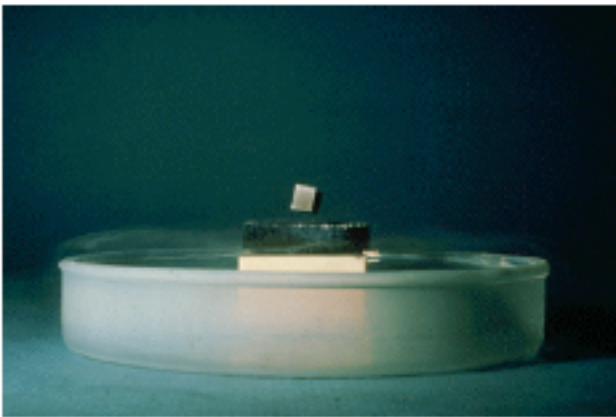
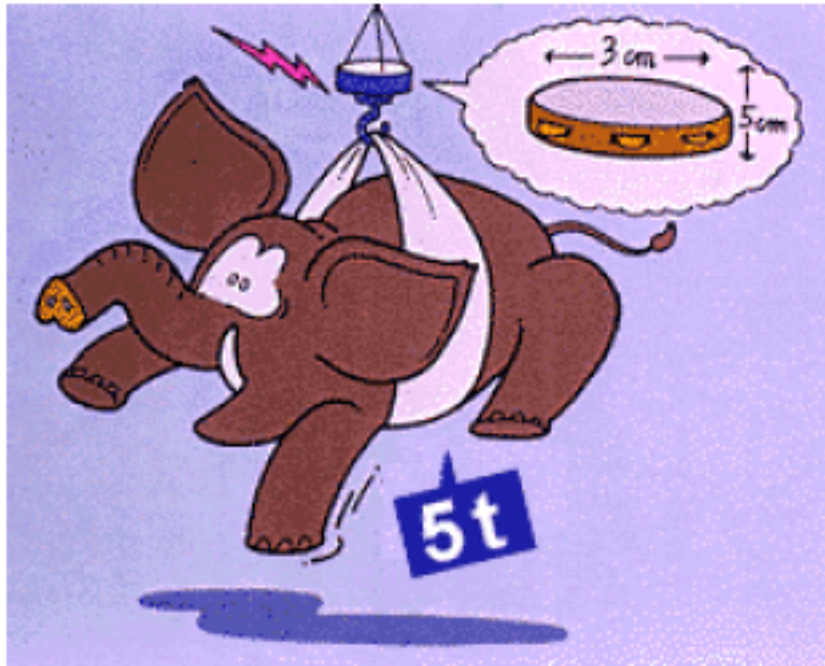
**Soft Loops Have Small Areas  
Hard Loops Have Large Areas  
Work  $\sim$  Area**

# Permanent Magnets

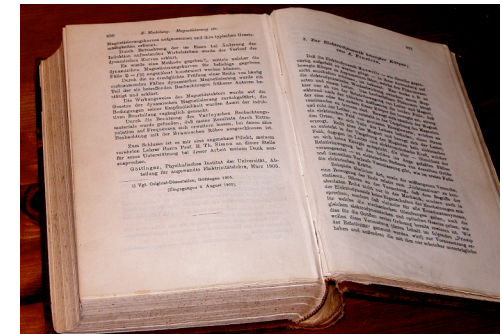
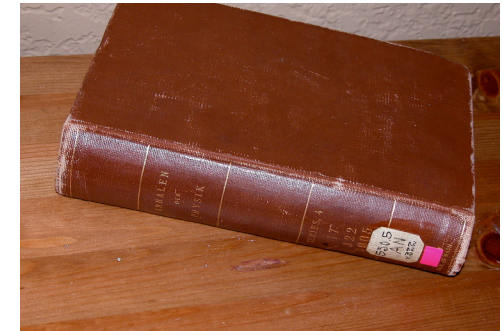
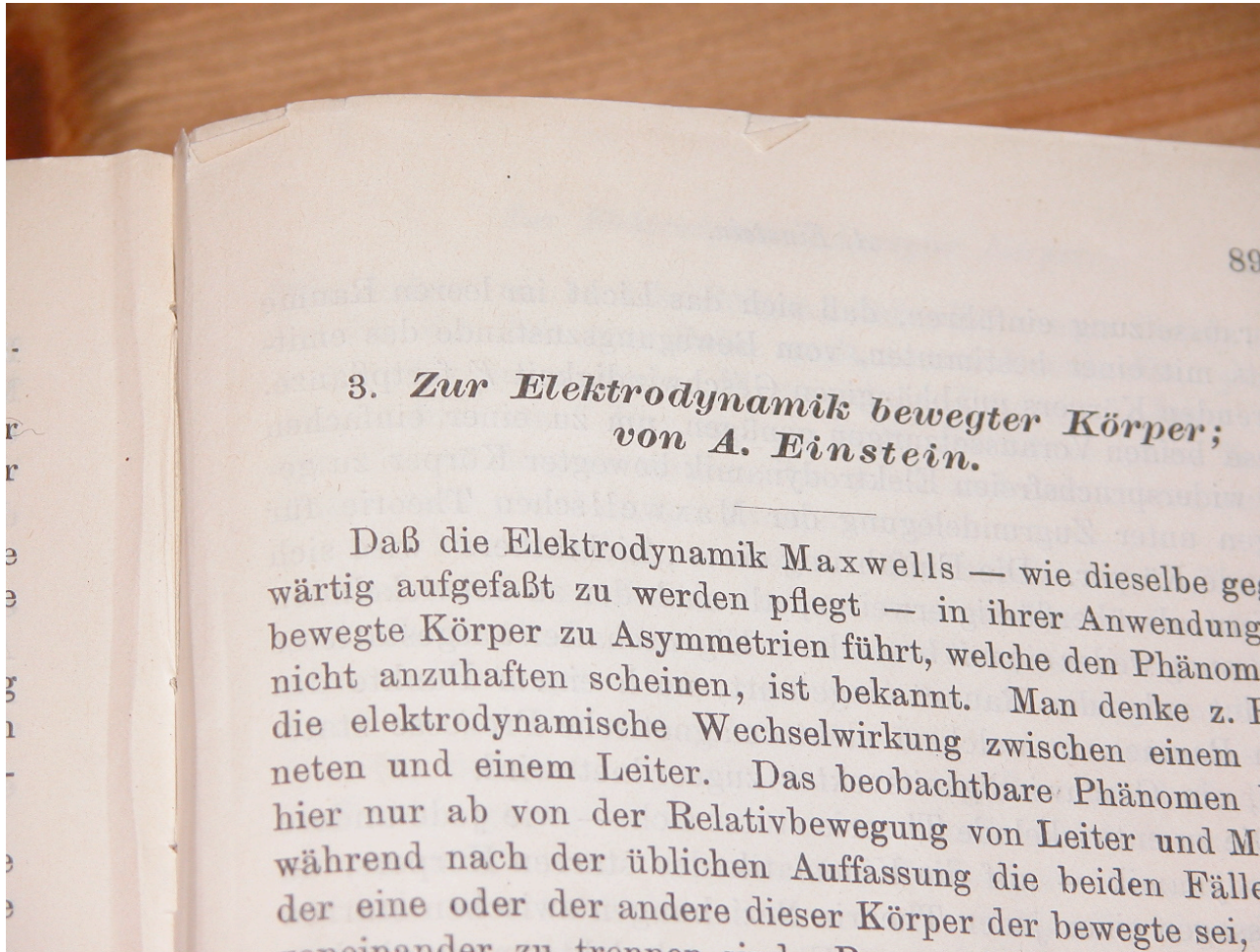




# Powerful Magnet

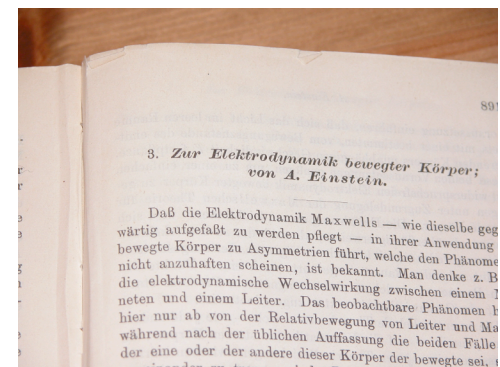
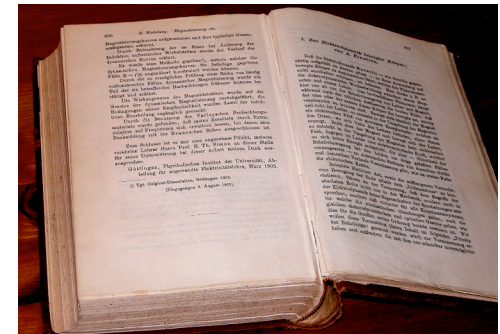
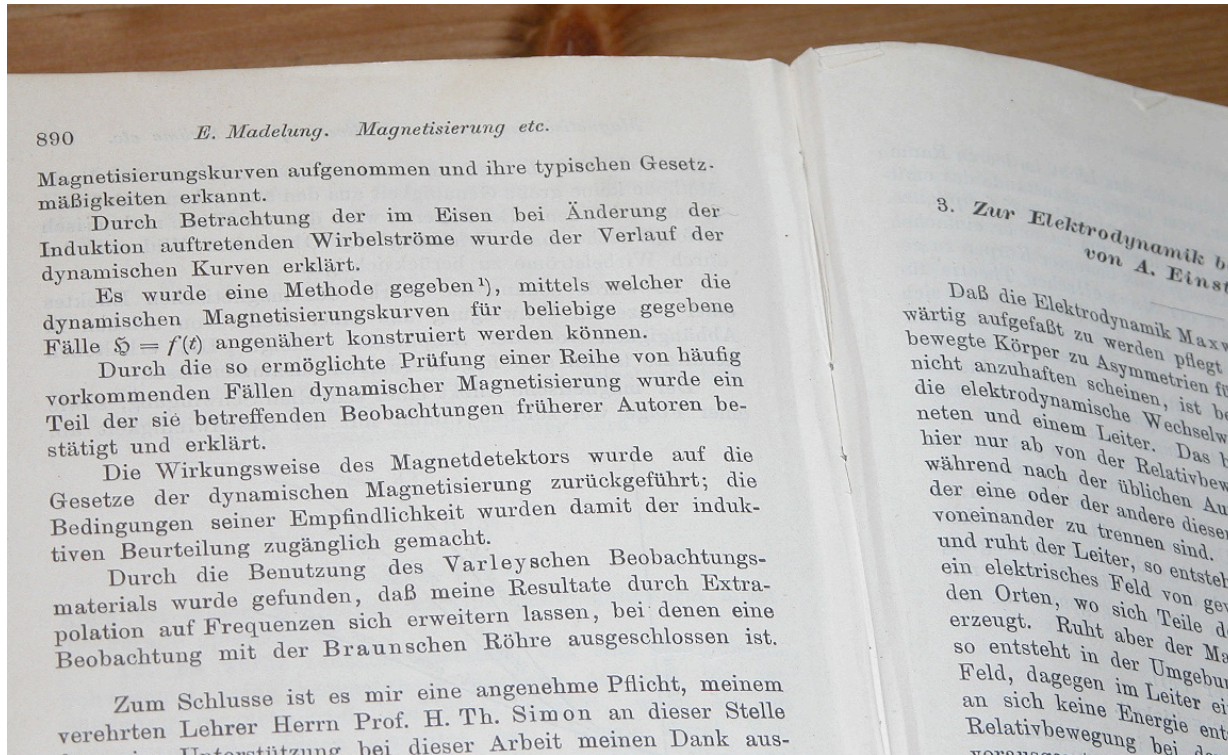
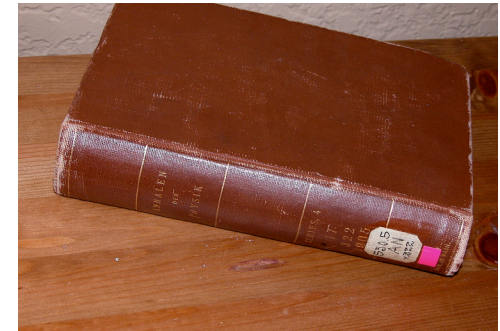


# The Most Famous Paper?



**Annalen der Physik Volume 322, 891 (1905)**

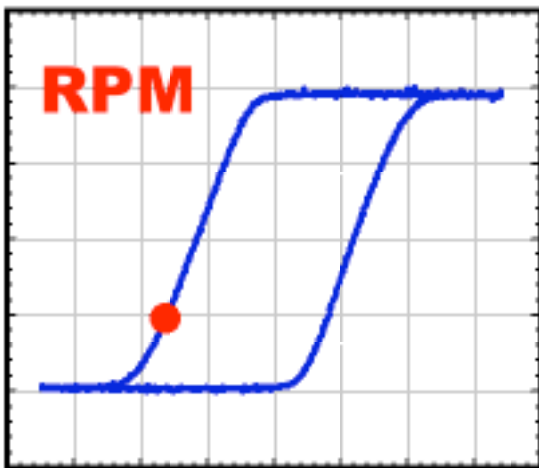
# But what is the paper just before Einstein's?



**It is Erwin Madelung's thesis on macroscopic magnetic hysteresis!**

# Return-Point Memory (RPM)

Along the major hysteresis loops, the **macroscopic** magnetization is completely determined by the applied field. **Madelung 1905**

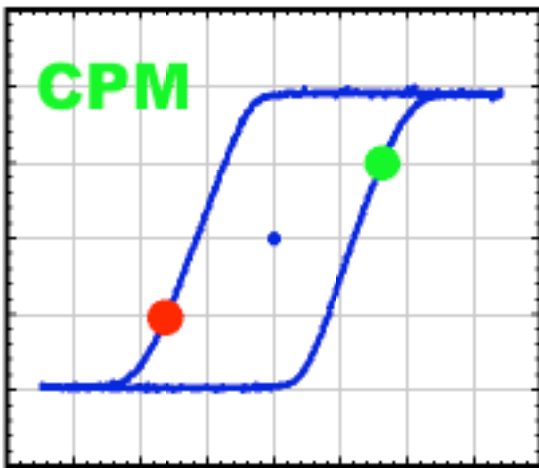


But are the **microscopic** domains precisely the same every time or is only the ensemble average the same?

We find about half of the domains are the same every time and about half of the domains are different every time.

# Complementary-Point Memory (CPM)

Major loops are inversion symmetric through the origin => the **macroscopic** magnetization is also inverted.



But are the **microscopic** domains precisely inverted every time or is only the ensemble average inverted?

We find about half of the domains are inverted every time and about half of the domains are different every time.

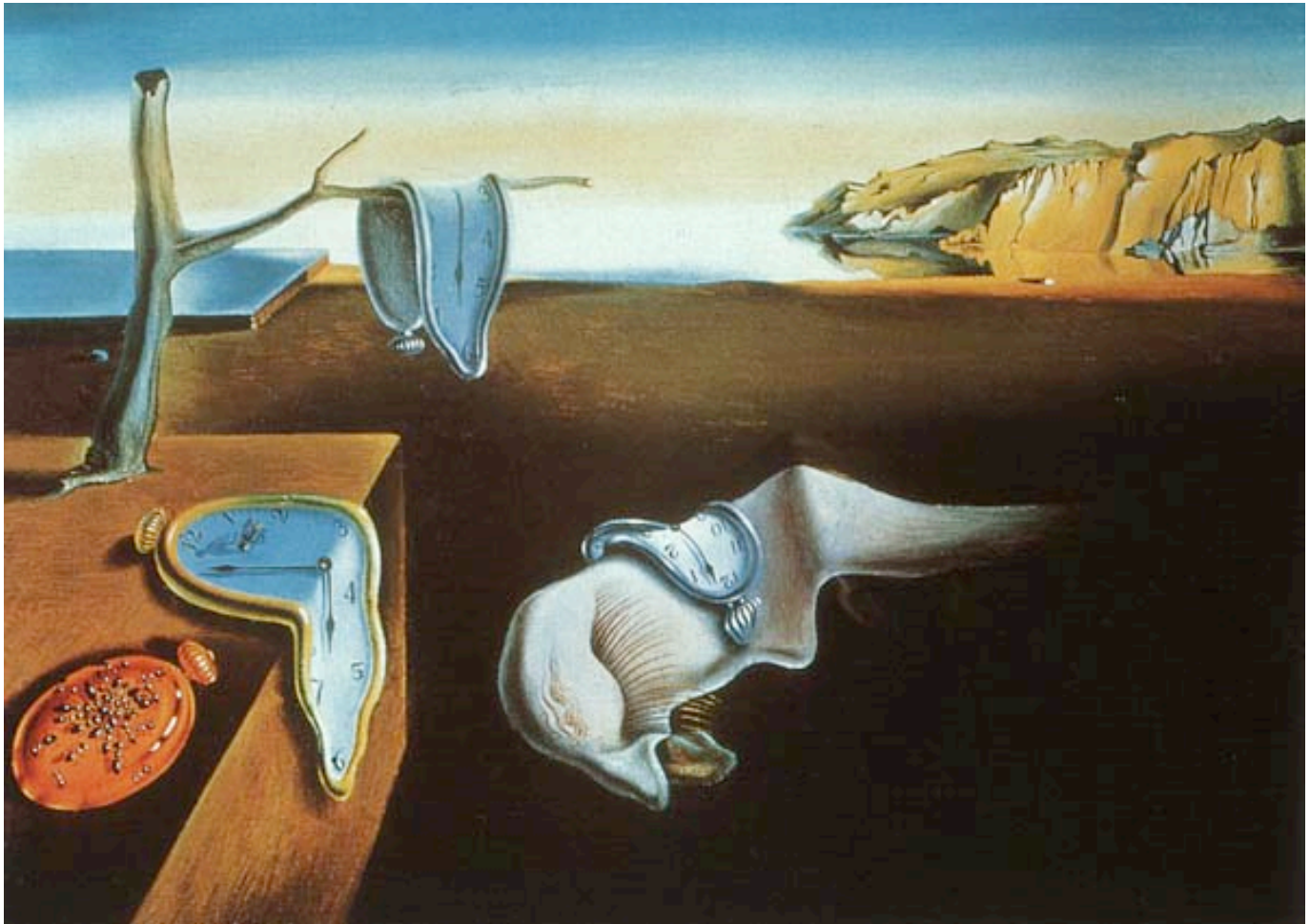
# **How Do Magnets Remember?**

**Same domain patterns every time?**

**Different domain patterns every time?**

**Some the same others different?**

# The Persistence of Memory



# **How Do Magnets Forget?**

**Same domain patterns every time?**

**Different domain patterns every time?**

**Some the same others different?**



# The Disintegration of Memory



# The Persistence of Memory



## The Influence of Disorder on Magnetic Memory

Michael S. Pierce  
University of Washington  
Physics Department

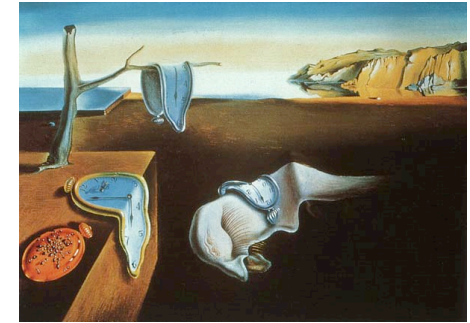
Los Alamos National Laboratory  
December 15<sup>th</sup>, 2005

The nation that controls magnetism  
controls the universe.

-Dick Tracy (Chester Gould)



# Colleagues & Friends



## Experimentalists

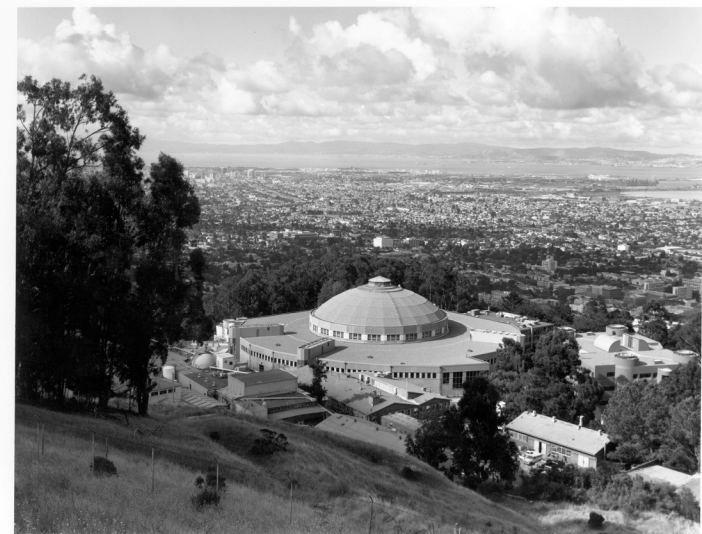
Larry B. Sorensen (my advisor!)  
Conor Buechler (UW)  
Steve Kevan (UO)  
Olav Hellwig (Hitachi)  
Eric Fullerton (Hitachi)  
Jeff Kortright (LBL)  
Kai Lui (UCD)

## Theorists

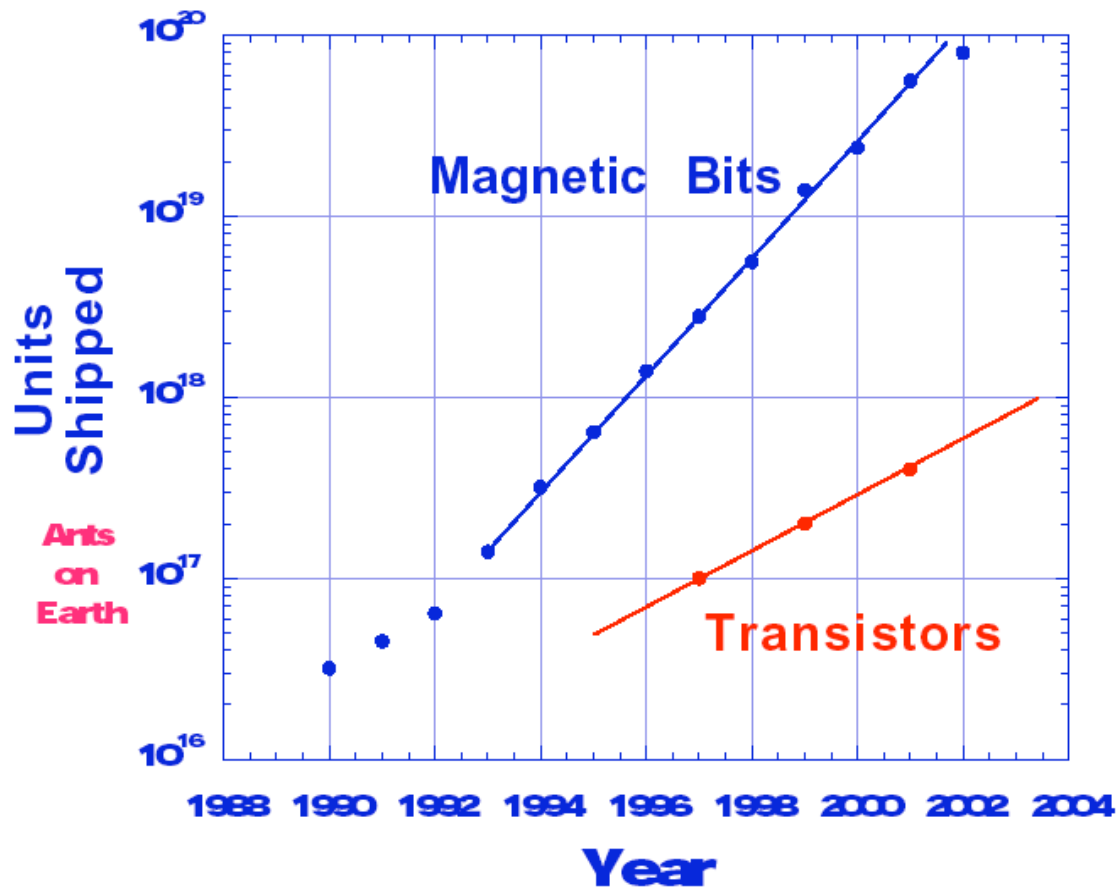
Eduardo A. Jagla (CAS)  
Josh M. Deutsch (UCSC)  
Trieu Mai (UCSC)  
Onuttom Narayan (UCSC)  
Gergely Zimanyi (UCD)  
Helmut Katzberger (ETH)

We performed our experiments at the Advanced Light Source at Berkeley National Lab.

Our work is supported by the DoE.



# Why study magnetic films?



Will this trend continue without stopping?

No!

As the density becomes higher, the thermal energy in the media becomes a serious problem.

What can be done?

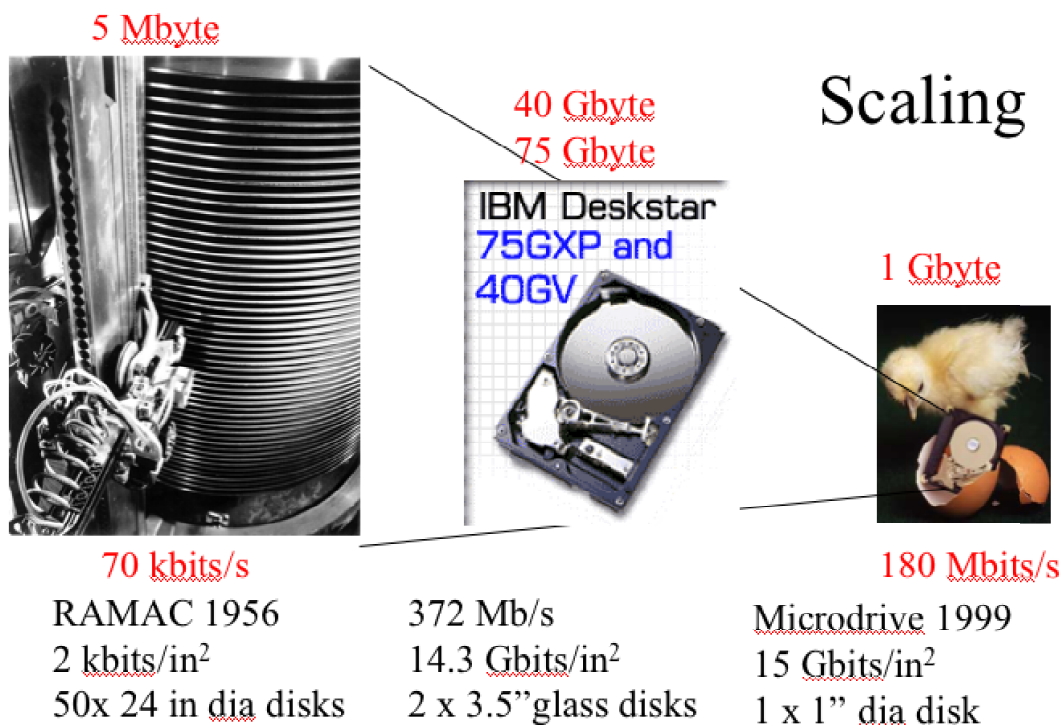
Perpendicular Media!

---

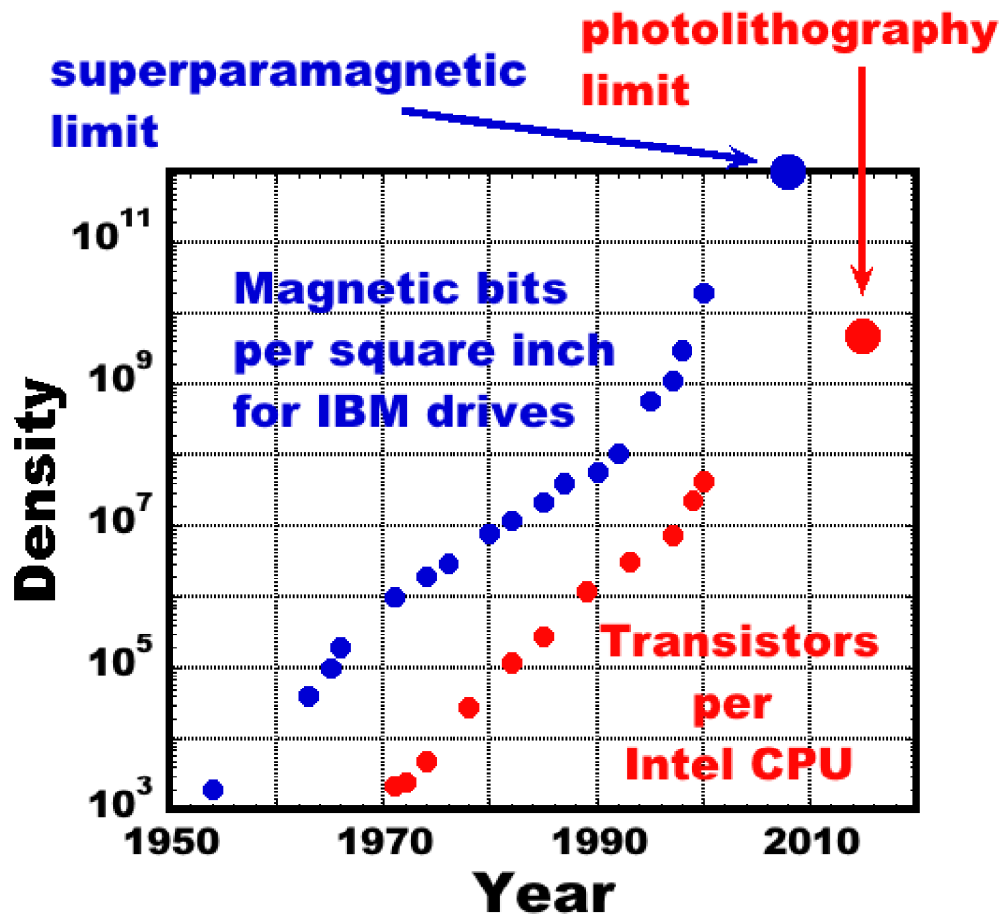
Hitachi released the first perpendicular media disk drive this year!

# What is the fundamental microscopic physics for magnetic memory?

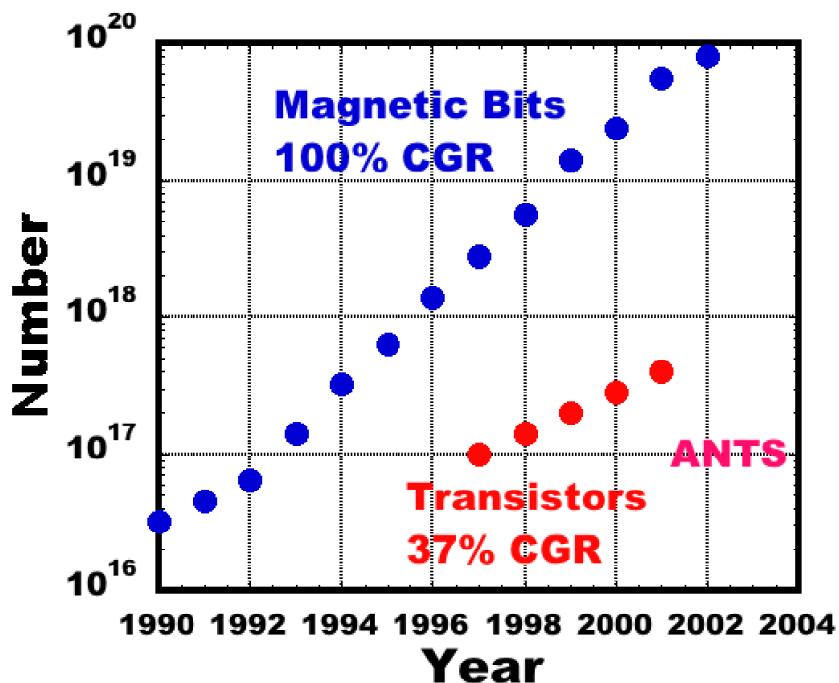
**Disorder => magnetic hardening**  
**Speckle => to study this disorder**  
**Rapid growth and miniaturization of magnetic storage => nanoscale disorder**



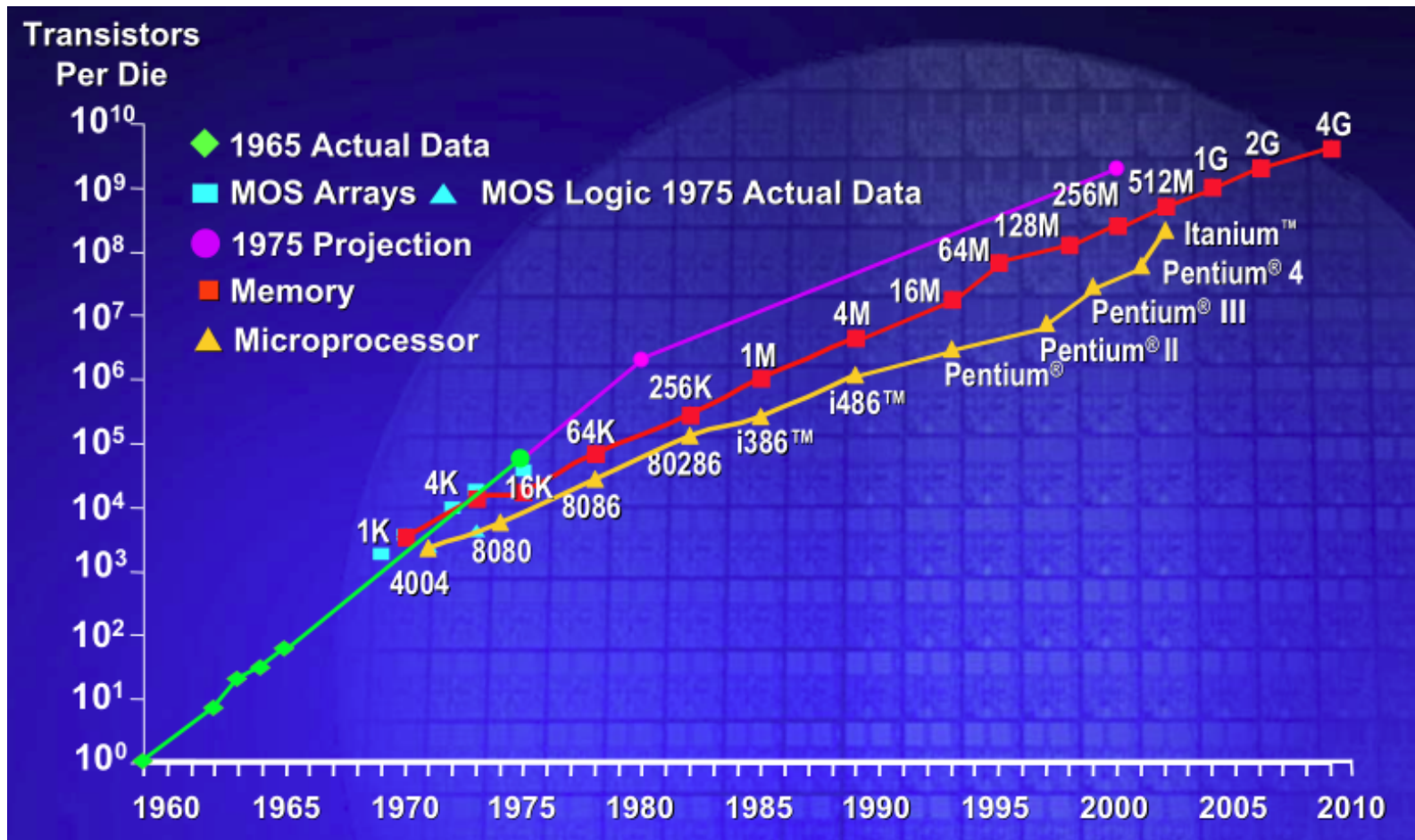
# Approaching the Physical Limits



## Units Shipped per Year

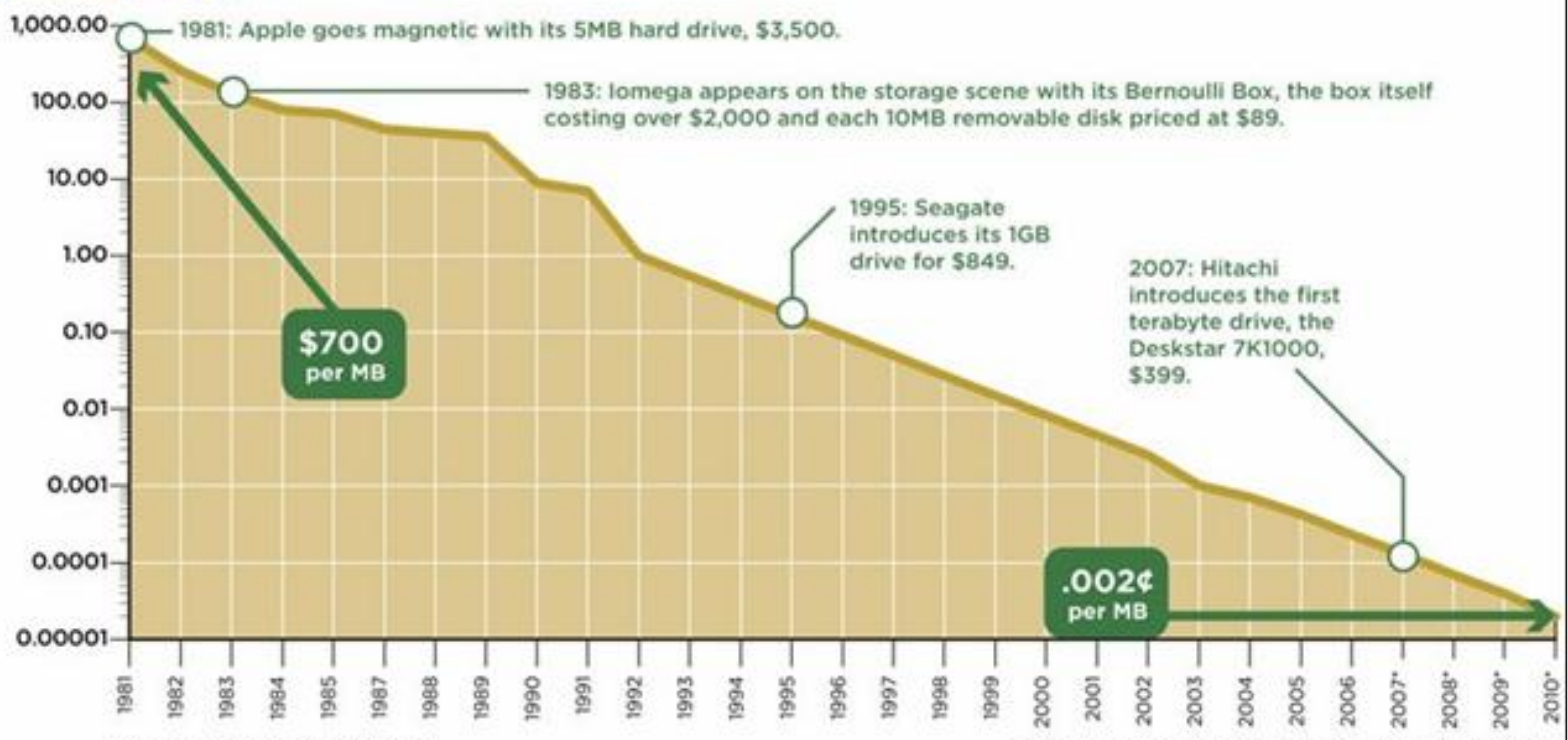


# Moore's Law



# STORAGE: FROM HIGHWAY ROBBERY TO RUNAWAY BARGAIN

\$ per megabyte



\*Projected. No data is available for 1986.

Sources: Ars Technica, Little Tech Shoppe, Steve Gilheany, ExtremeTech



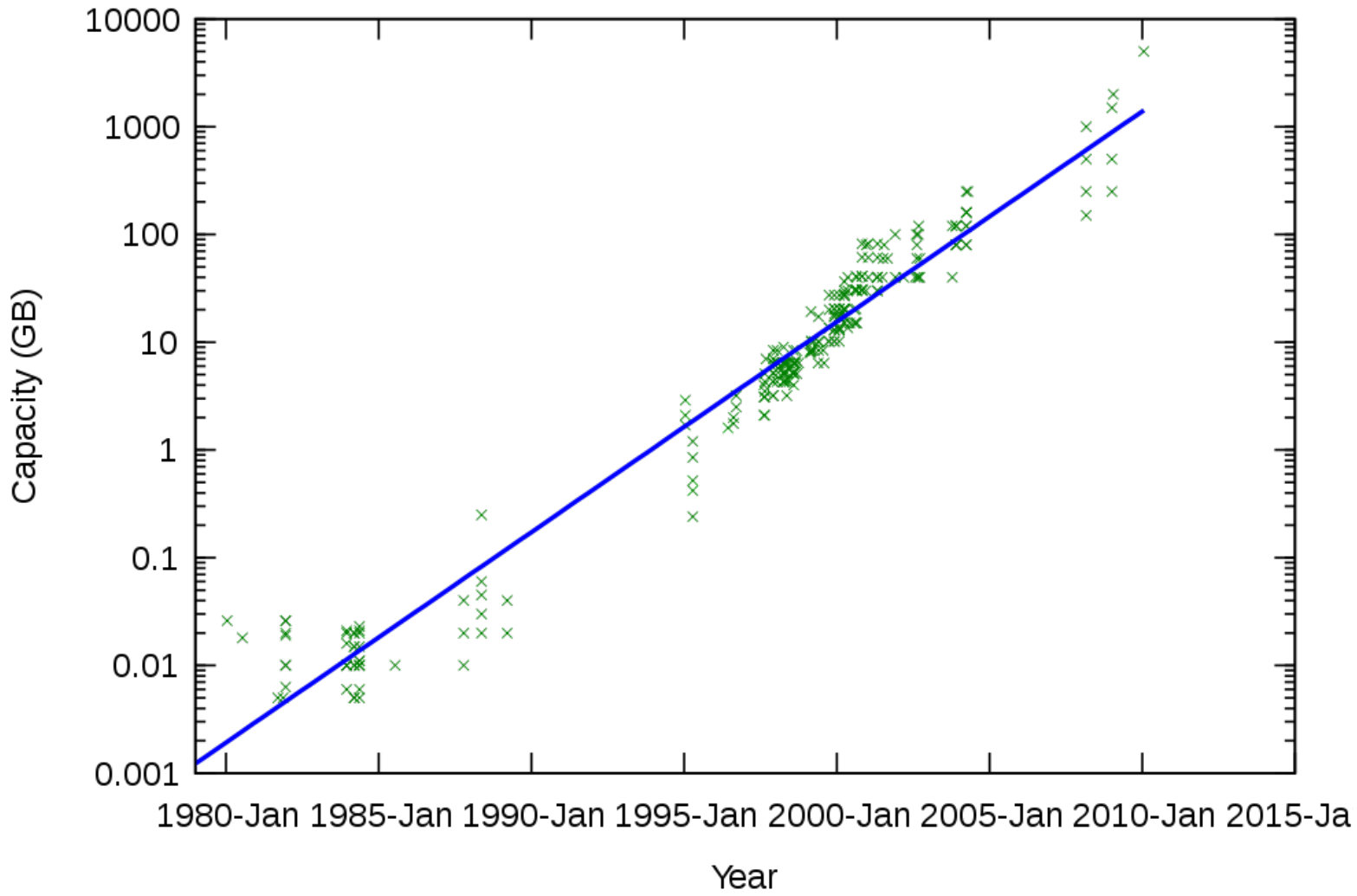
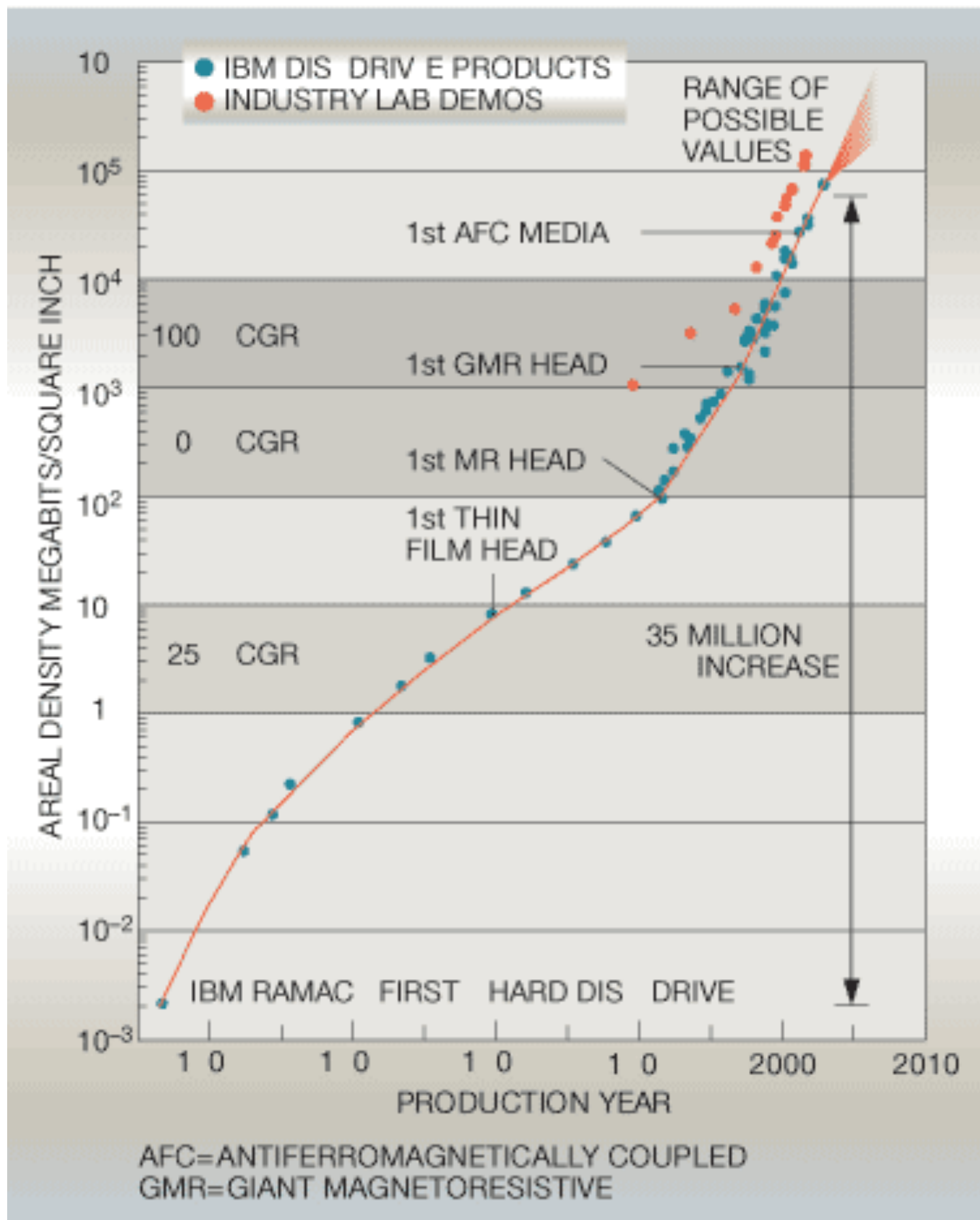
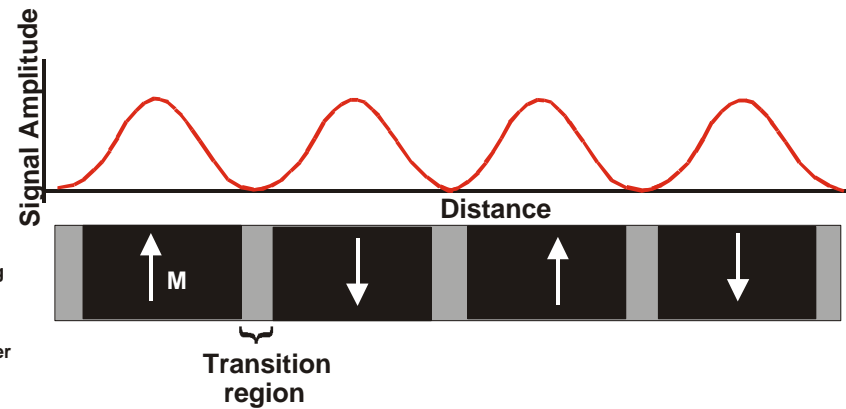
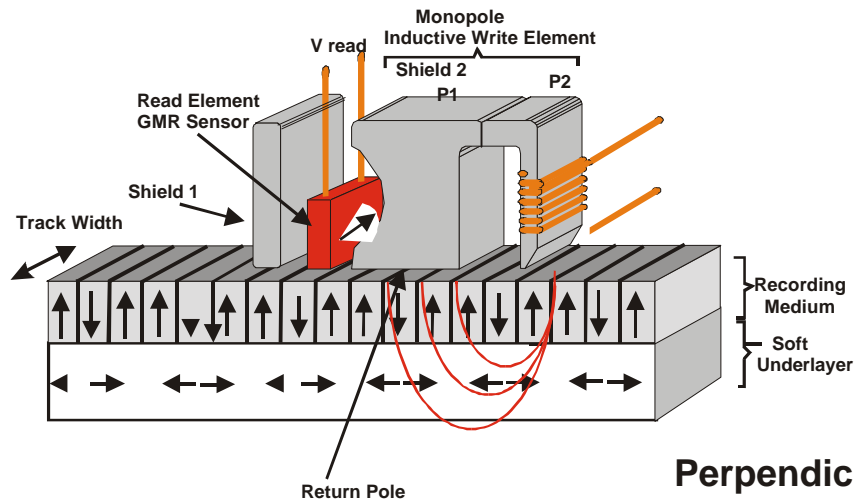
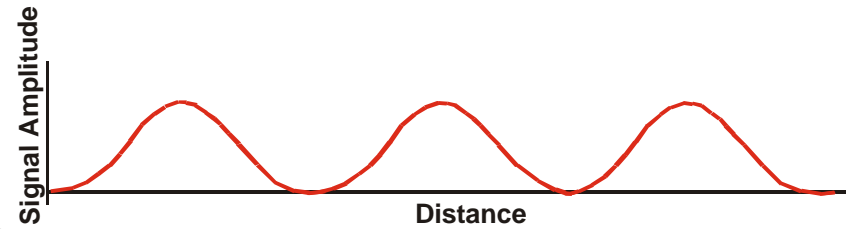
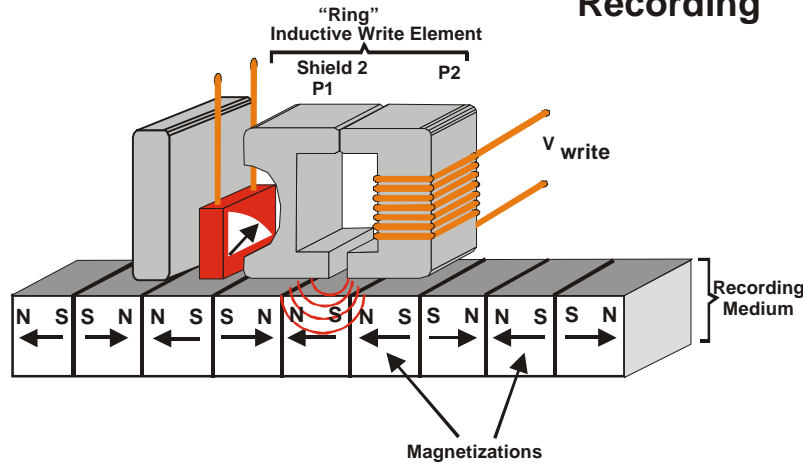


Figure 1 Hard disk drive areal density trend



## Longitudinal Recording



## Perpendicular Recording

### Recording Technologies

Ed Grochowski

# **Perpendicular Magnetic Media**

**<http://gprime.net/flash.php/getperpendicular>**

# MAGNETS

# Our X-ray Scattering Experiment

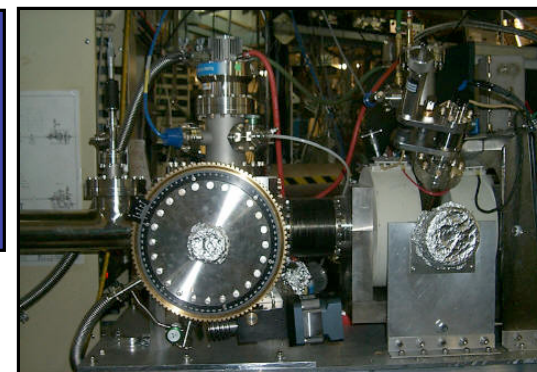
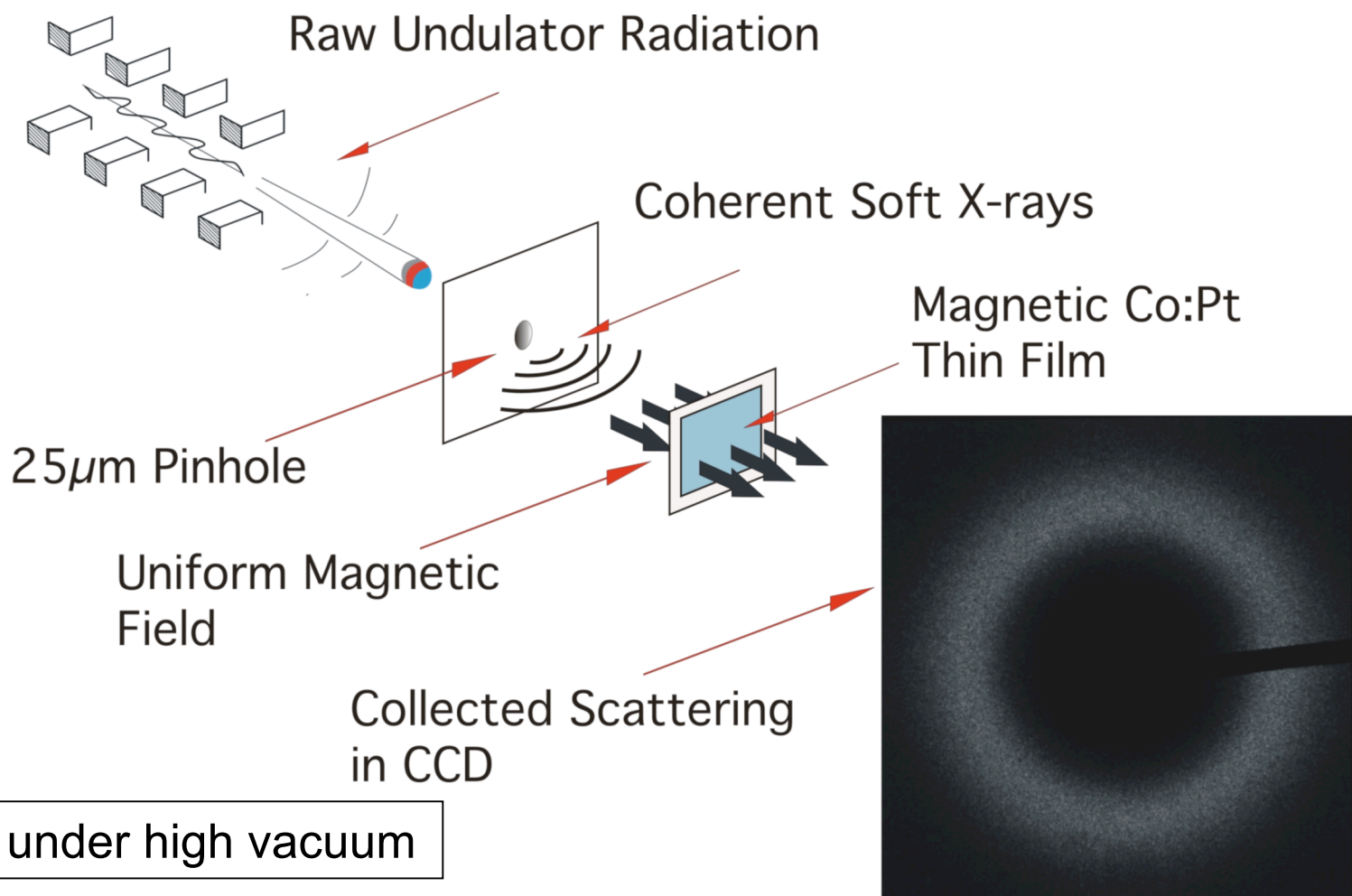
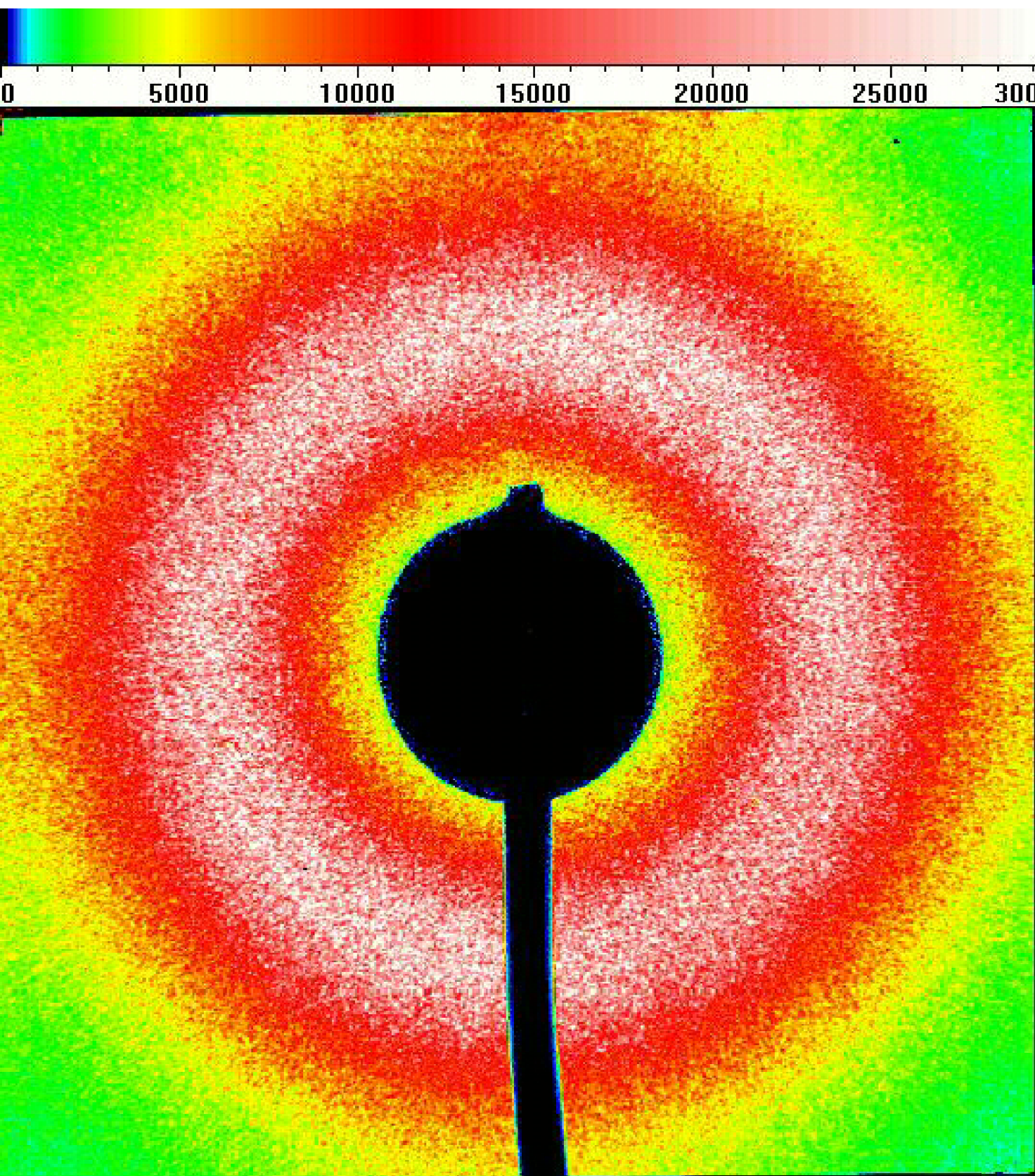


Table top science connected to a giant light-bulb.



# Typical Speckle Pattern



# Speckle pattern

From Wikipedia, the free encyclopedia

A **speckle pattern** is a random **intensity** pattern produced by the mutual **interference** of a set of **wavefronts**.<sup>[1]</sup> This phenomenon has been investigated by scientists since the time of **Newton**, but speckles have come into prominence since the invention of the laser and have now found a variety of applications.

## Contents [hide]

1 Occurrence

2 Explanation

2.1 Subjective speckles

2.2 Objective speckles

3 Near-field speckles

4 Applications

5 Reduction

6 See also

7 References

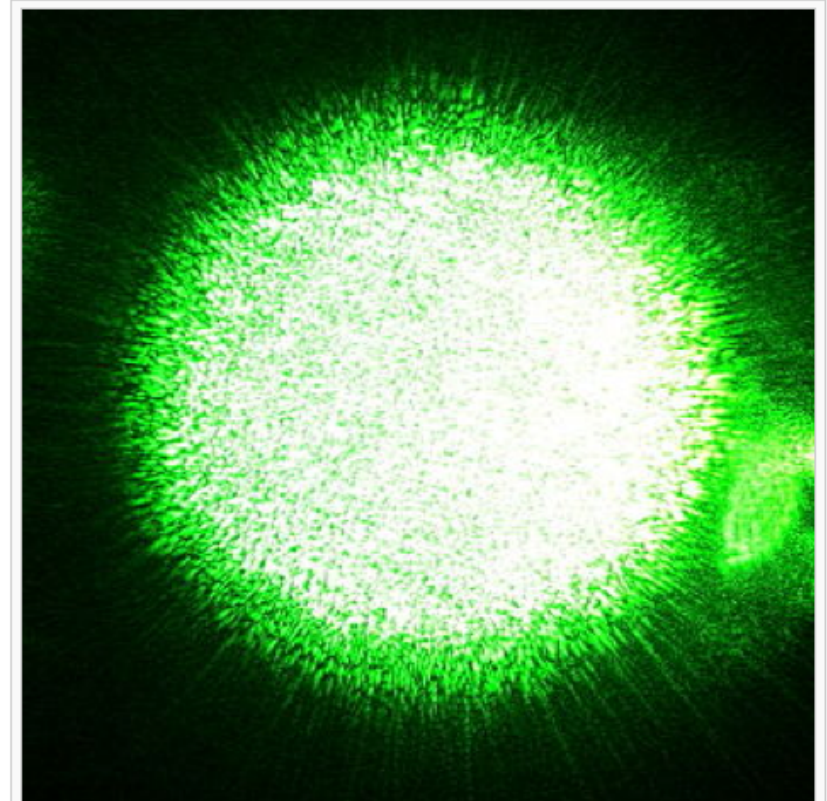
8 External links

## Occurrence

[edit]

A familiar example is the random pattern created when a **laser** beam is scattered off a rough surface - see picture. A less familiar example of speckle is the highly magnified image of a **star** through imperfect optics or through the **atmosphere** (see **speckle imaging**). A speckle pattern can also be seen when sunlight is scattered by a fingernail.<sup>[2]</sup>

The speckle effect is observed when **radio waves** are scattered from rough surfaces such as ground or sea, and can also be found in ultrasonic imaging. In the output of a **multi-mode optical fiber**, a speckle pattern results from a superposition of **mode** field patterns. If the relative modal **group velocities** change with **time**, the speckle pattern will also change with time. If **differential mode attenuation** occurs, **modal noise** results.<sup>[3]</sup>



Laser speckle on a digital camera image from a green laser pointer. This is a subjective speckle pattern. (Note that the color differences in the image are introduced by limitations of the camera system.)



## **Random Walk Applets**

<http://math.furman.edu/~dcs/java/rw.html>

<http://polymer.bu.edu/java/java/2drw/RandWalk2D.html>

<http://www.rbyter.com/java/randomWalkDescription.html>

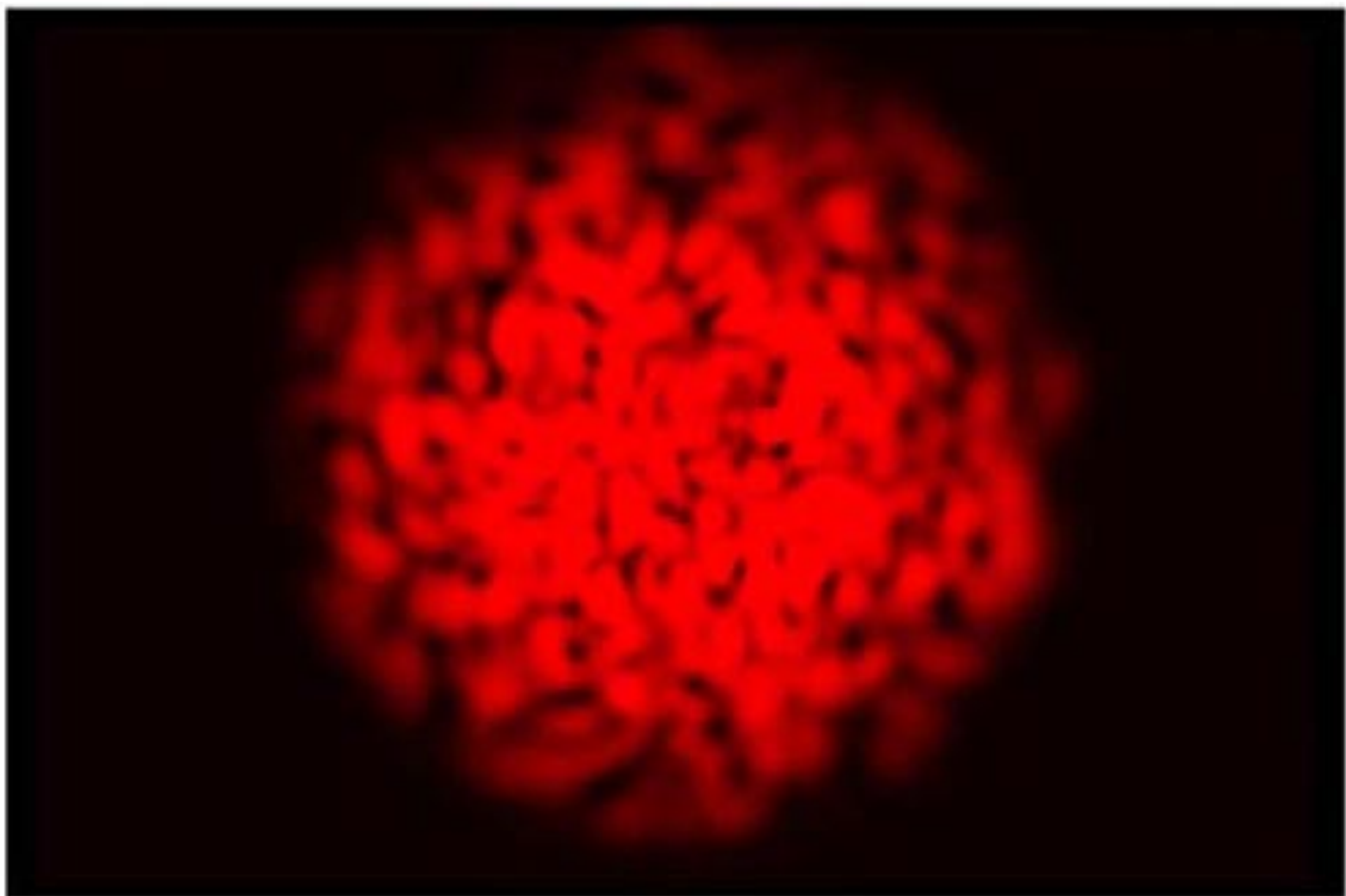
## **Ising Model Applets**

<http://physics.ucsc.edu/~peter/ising/ising.html>

<http://www.pha.jhu.edu/~javalab/ising/ising.html>

<http://www.ibiblio.org/e-notes/Perc/ising.htm>

<http://www-reynal.ensea.fr/applets/spin-models/en/afising.html>



# Speckle noise

From Wikipedia, the free encyclopedia

**Speckle noise** is a granular noise that inherently exists in and degrades the quality of the active [radar](#) and [synthetic aperture radar](#) (SAR) images.

Speckle noise in conventional radar results from random fluctuations in the return signal from an object that is no bigger than a single image-processing element. It increases the mean grey level of a local area.<sup>[1]</sup>

Speckle noise in SAR is generally more serious, causing difficulties for image interpretation.<sup>[1][2]</sup> It is caused by coherent processing of backscattered signals from multiple distributed targets. In SAR oceanography, for example, speckle noise is caused by signals from elementary scatterers, the gravity-capillary ripples, and manifests as a pedestal image, beneath the image of the sea waves.<sup>[3][4]</sup>

Several different methods are used to eliminate speckle noise, based upon different mathematical models of the phenomenon.<sup>[3]</sup> One method, for example, employs *multiple-look processing* (a.k.a. *multi-look processing*), averaging out the speckle noise by taking several "looks" at a target in a single radar sweep.<sup>[1][2]</sup> The average is the *incoherent average* of the looks.<sup>[2]</sup>

A second method involves using adaptive and non-adaptive filters on the signal processing (where adaptive filters adapt their weightings across the image to the speckle level, and non-adaptive filters apply the same weightings uniformly across the entire image). Such filtering also eliminates actual image information as well, in particular high-frequency information, and the applicability of filtering and the choice of filter type involves tradeoffs. Adaptive speckle filtering is better at preserving edges and detail in high-texture areas (such as forests or urban areas). Non-adaptive filtering is simpler to implement, and requires less computational power, however.<sup>[1][2]</sup>

There are two forms of non-adaptive speckle filtering: one based on the [mean](#) and one based upon the [median](#) (within a given rectangular area of pixels in the image). The latter is better at preserving edges whilst eliminating noise spikes, than the former is. There are many forms of adaptive speckle filtering, including the Lee filter, the Frost filter, and the Refined Gamma Maximum-A-Posteriori (RGMAP) filter. They all rely upon three fundamental assumptions in their mathematical models, however.<sup>[1]</sup>

- Speckle noise in SAR is a *multiplicative* noise, i.e. it is in direct proportion to the local grey level in any area.<sup>[1]</sup>
- The signal and the noise are statistically independent of each other.<sup>[1]</sup>
- The sample mean and [variance](#) of a single pixel are equal to the mean and variance of the local area that is centred on that pixel.<sup>[1]</sup>

The Lee filter converts the multiplicative model into an additive one, thereby reducing the problem of dealing with speckle noise to a known tractable case.<sup>[5]</sup>

The speckle can also represent some useful information, particularly when it is linked to the [laser speckle](#) and to the [dynamic speckle](#) phenomenon, where the changes of the [speckle pattern](#), in time, can be a measurement of the surface's activity.

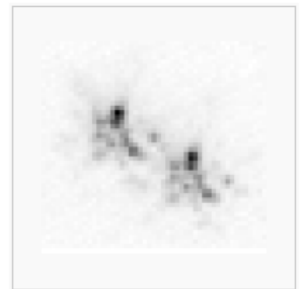
# Speckle imaging

From Wikipedia, the free encyclopedia

**Speckle imaging** (also known as *video astronomy*) describes a range of high-resolution astronomical imaging techniques based either on the [shift-and-add](#) ("*image stacking*") method or on **speckle interferometry** methods. These techniques can dramatically increase the [resolution](#) of ground-based [telescopes](#).

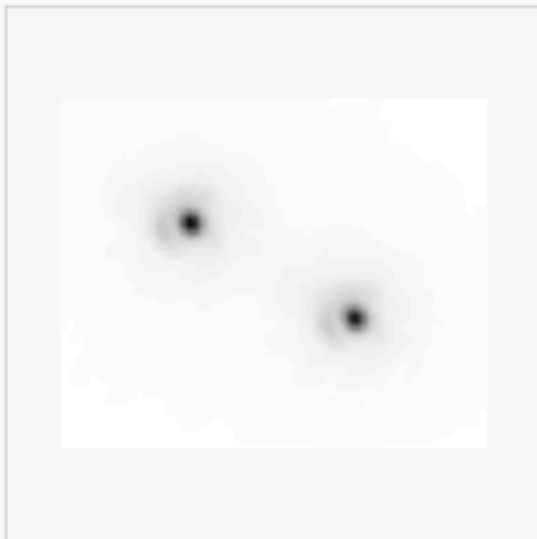
## Contents [\[hide\]](#)

- 1 Explanation
- 2 Types of speckle imaging
  - 2.1 Techniques based on the shift-and-add method
  - 2.2 Techniques based on speckle interferometry
- 3 Biology
- 4 See also
- 5 Example images
- 6 References

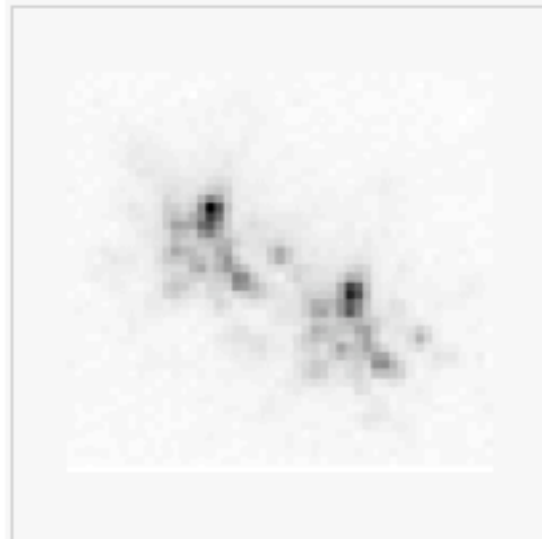


Typical short-exposure image of a binary star ([Zeta Bootis](#) in this case) as seen through atmospheric seeing. Each star should appear as a single point,

Both components are white **A-type giants**, with **apparent magnitudes** of +4.43 and +4.83.

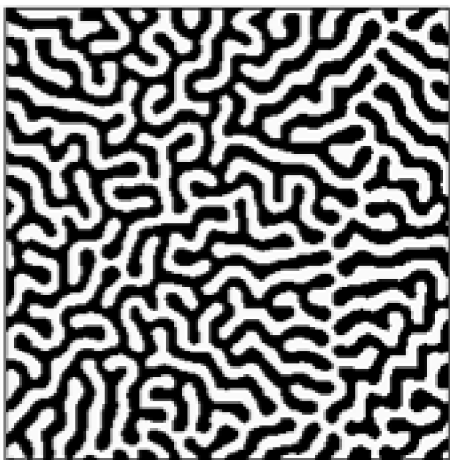
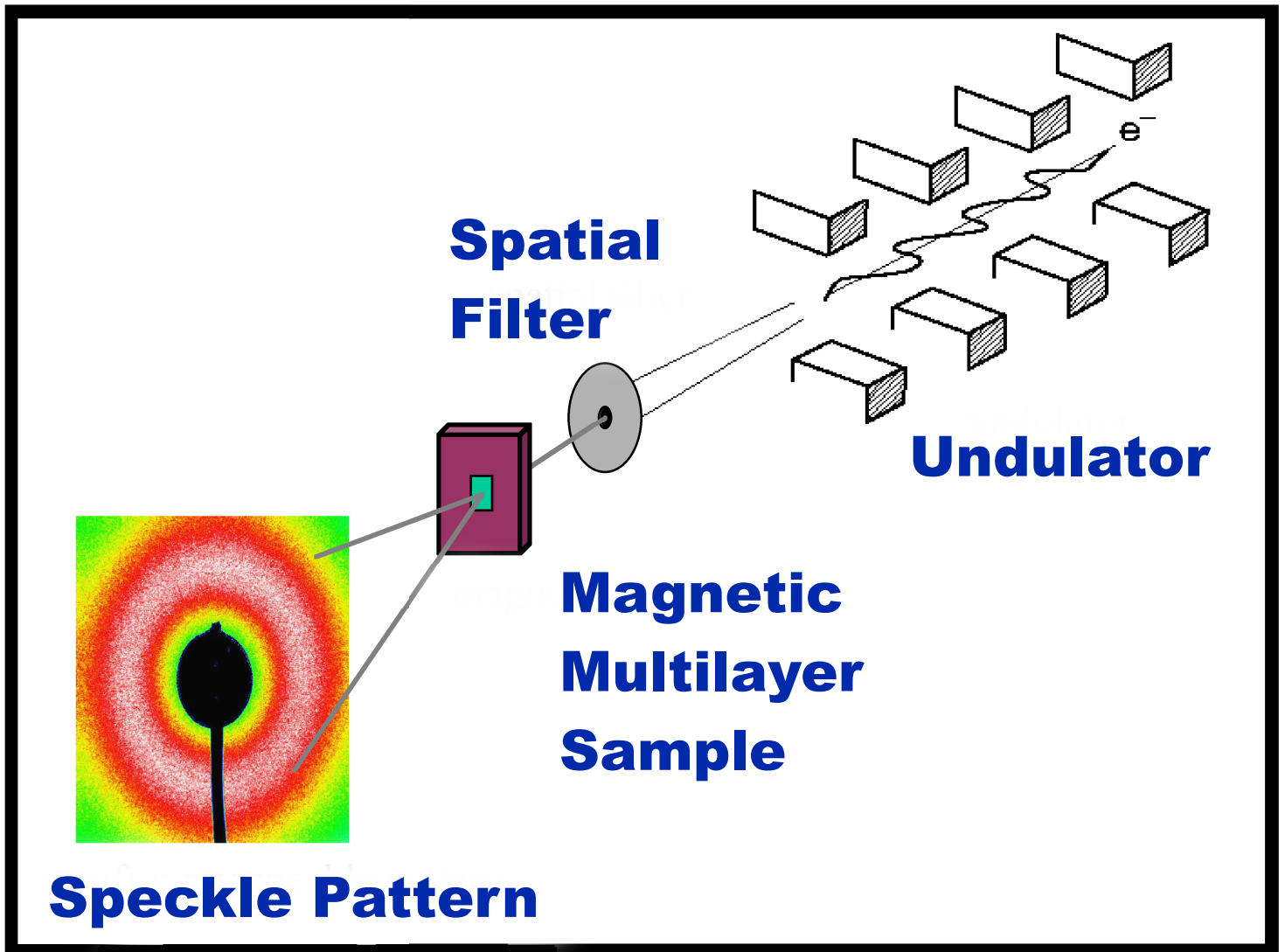


Zeta Bootis imaged with the **Nordic Optical Telescope** on 13 May 2000 using the **lucky imaging** method. (The **Airy discs** around the stars is **diffraction** from the 2.56m telescope aperture.)

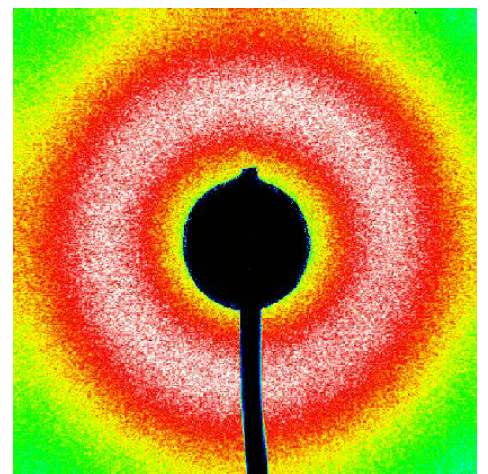


Typical short-exposure image of a binary star, as seen using **speckle imaging** through the Earth's atmosphere.

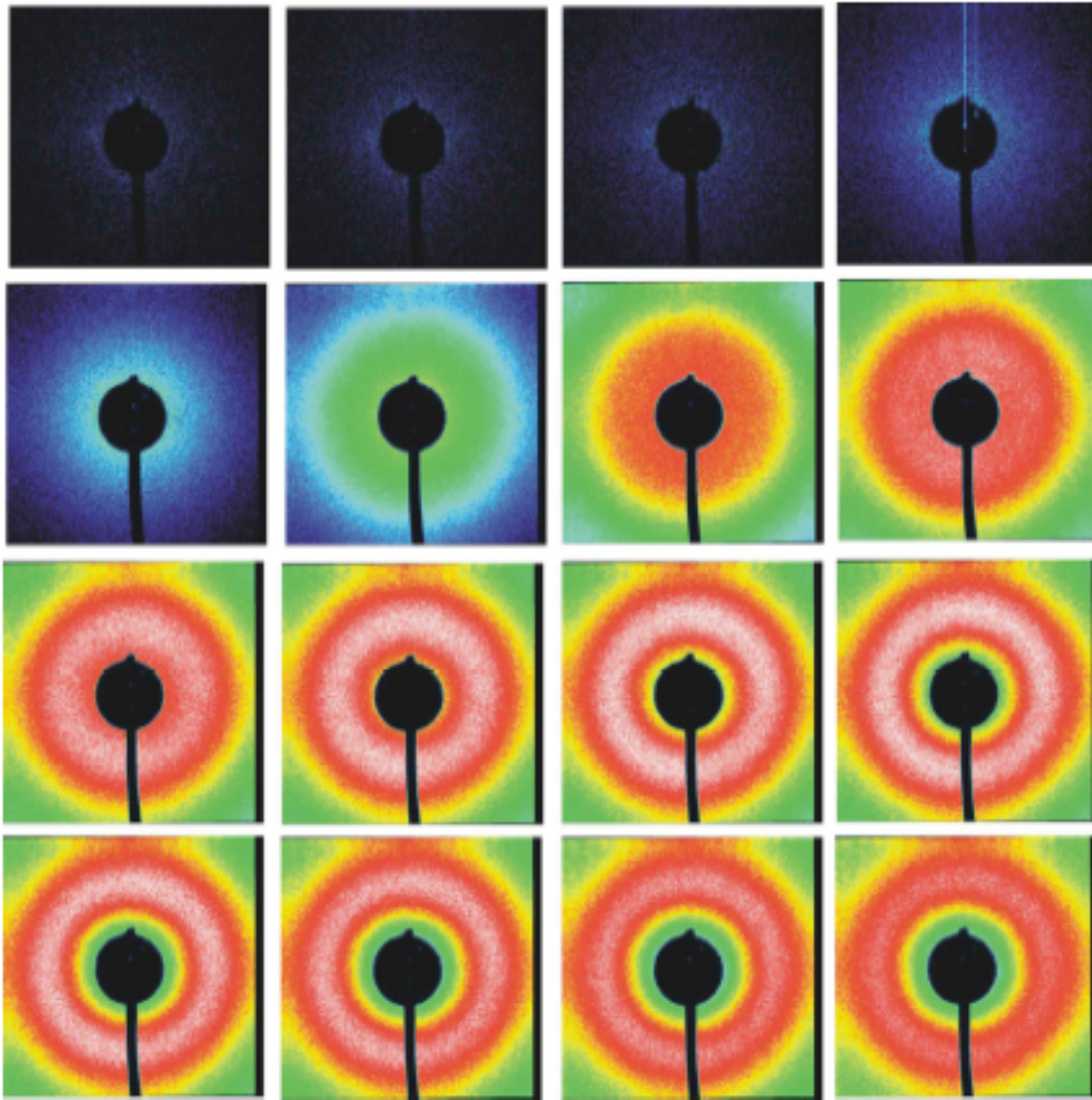
# Our Experiment



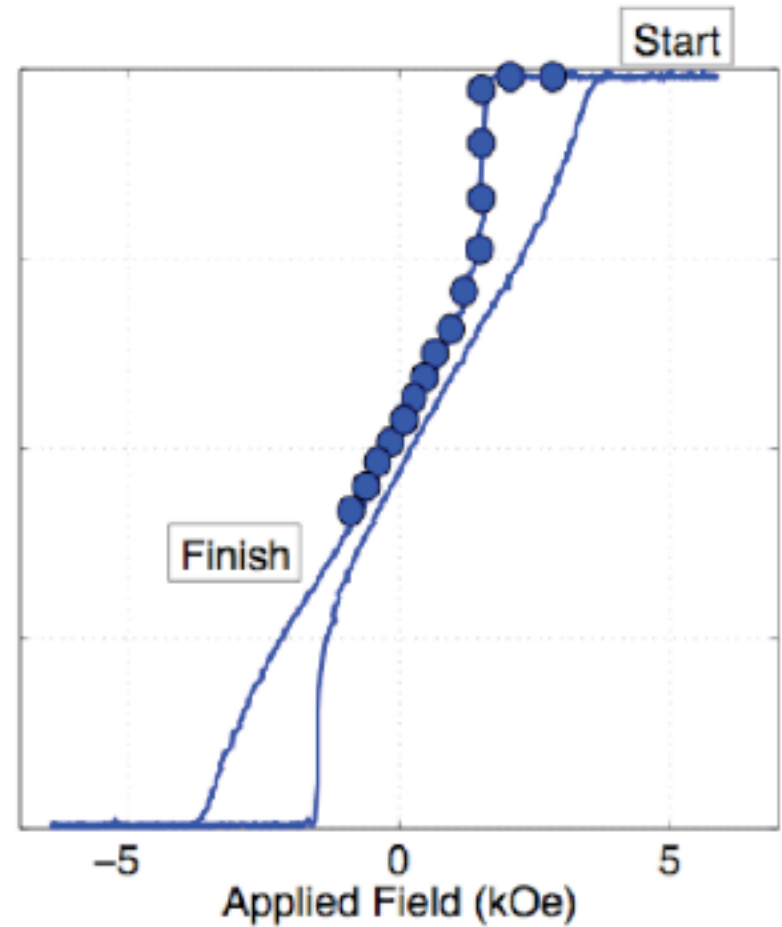
$$| FT |^2 = \Rightarrow$$

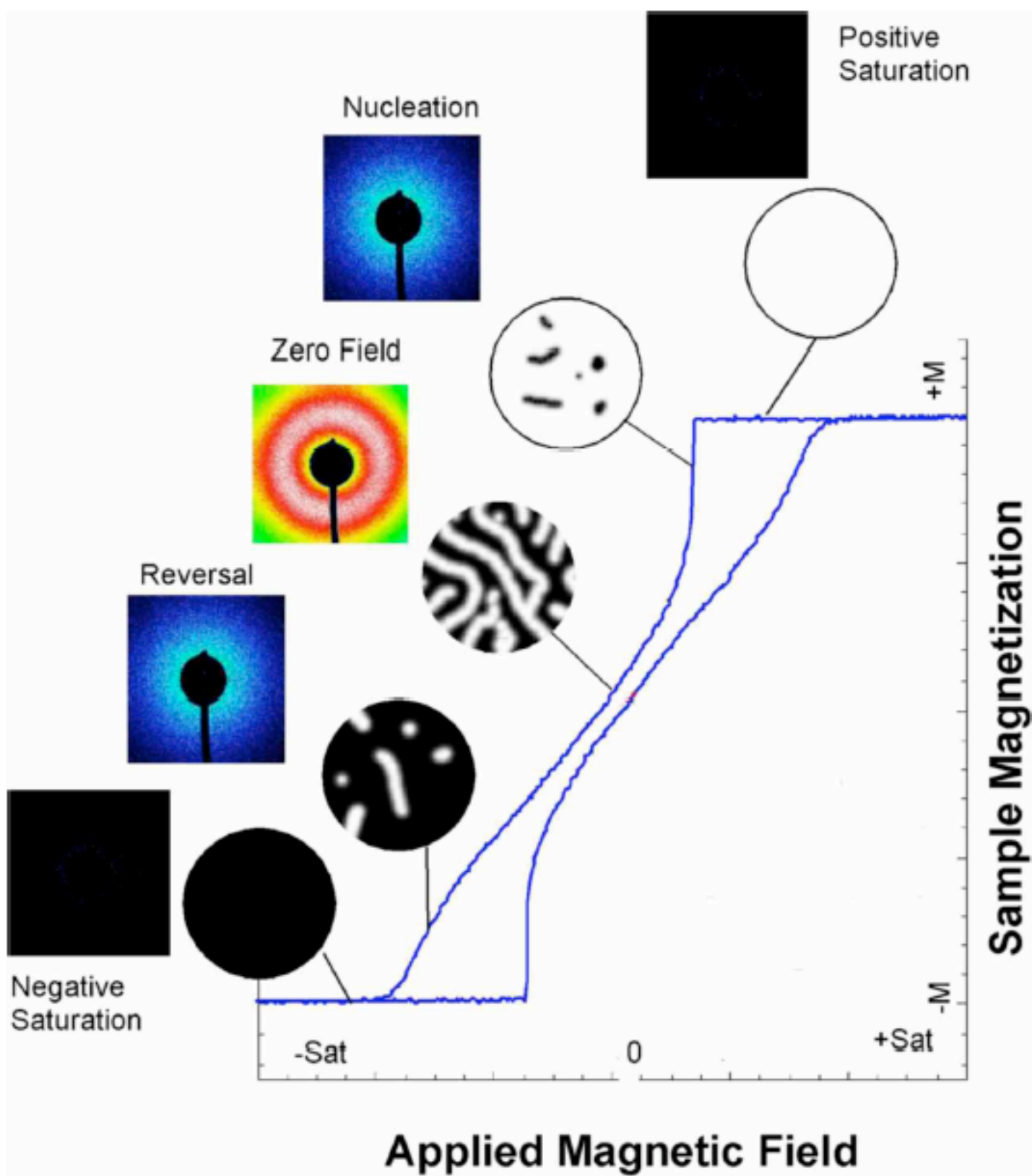


# Cookie to Donut Transition



## Magnetization







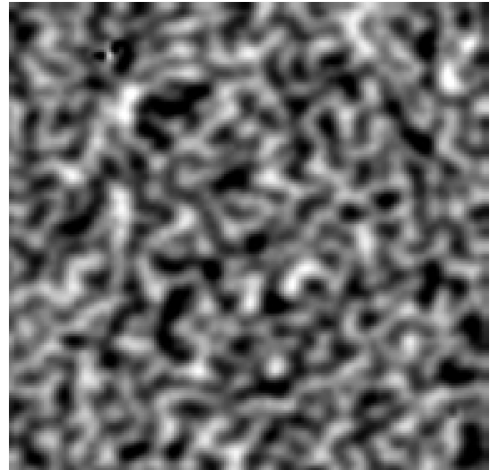
# Effect of the Disorder in Real Space

## MFM Images of the Magnetic Domains

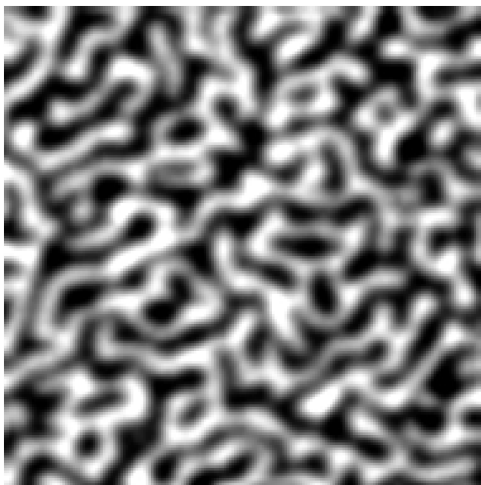
**3**



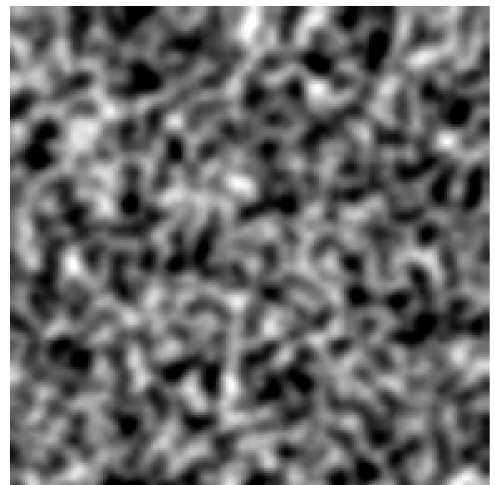
**10**



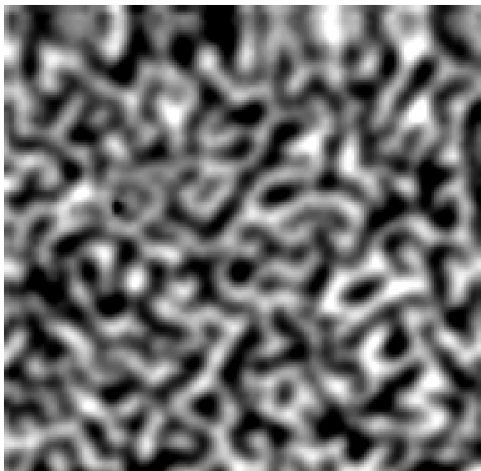
**7**



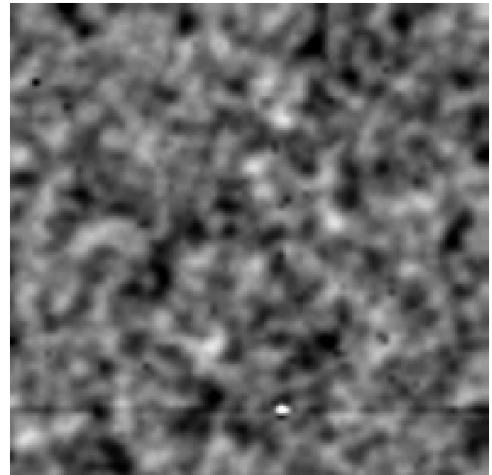
**12**



**8.5**

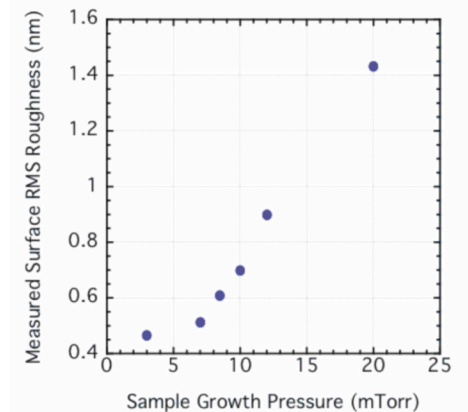


**20**



# The Six Sisters

Co:Pt multilayer magnetic films, grown at different sputtering pressure.



3mTorr

7mTorr

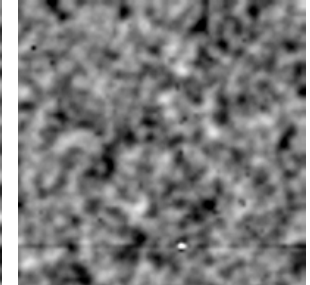
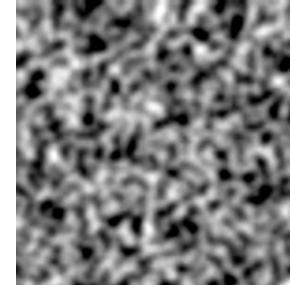
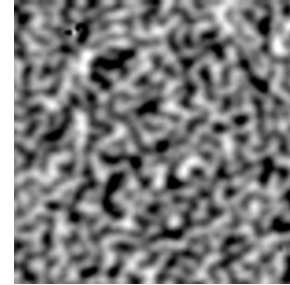
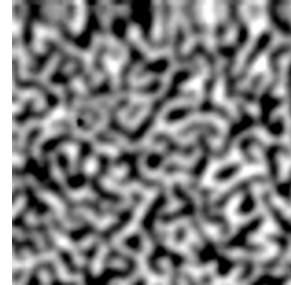
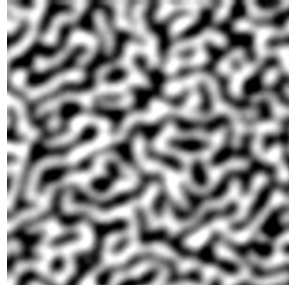
8.5mTorr

10mTorr

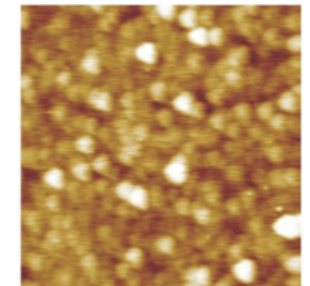
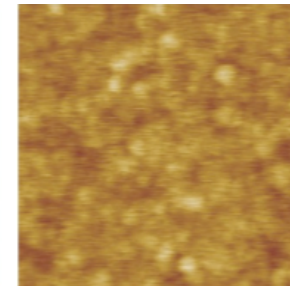
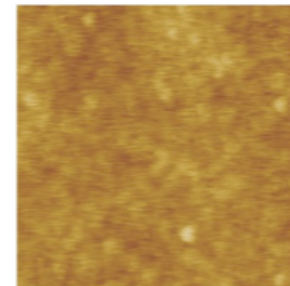
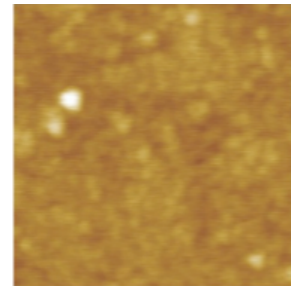
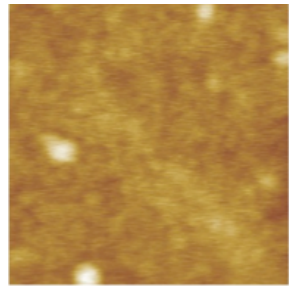
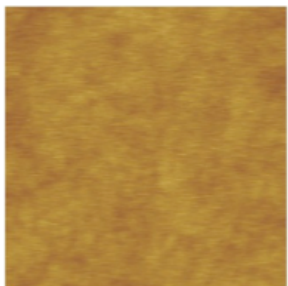
12mTorr

20mTorr

MFM ( $3\mu\text{m}^2$ )



AFM ( $1\mu\text{m}^2$ )

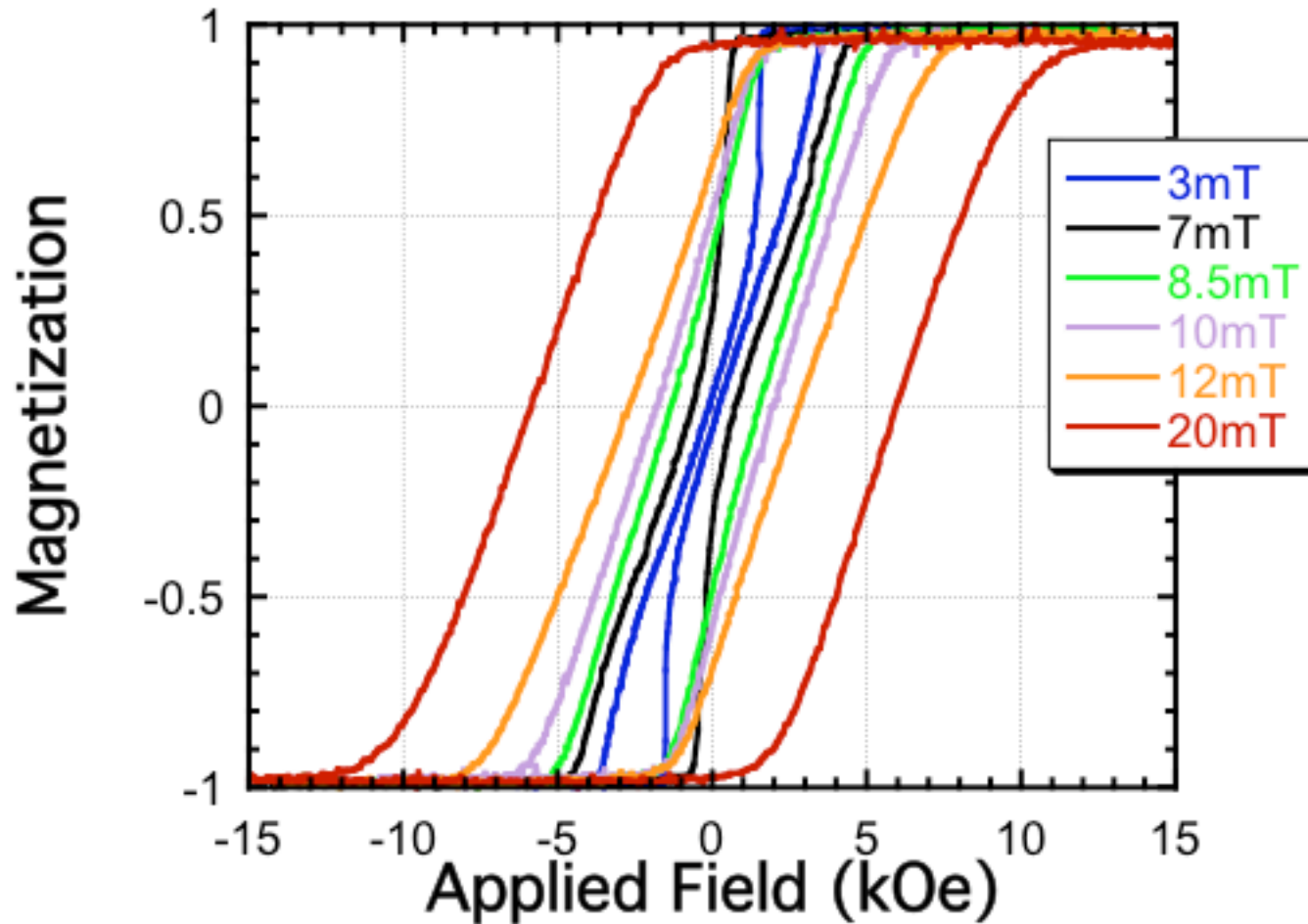


Each sample was grown with 50 repeats of 0.4nm Co & 0.7nm Pt.

As the sputtering pressure increases, the interfacial roughness between layers also increases. More roughness = more disorder!

# Major Hysteresis Loops: 3, 7, 8.5, 10, 12, & 20mT

---

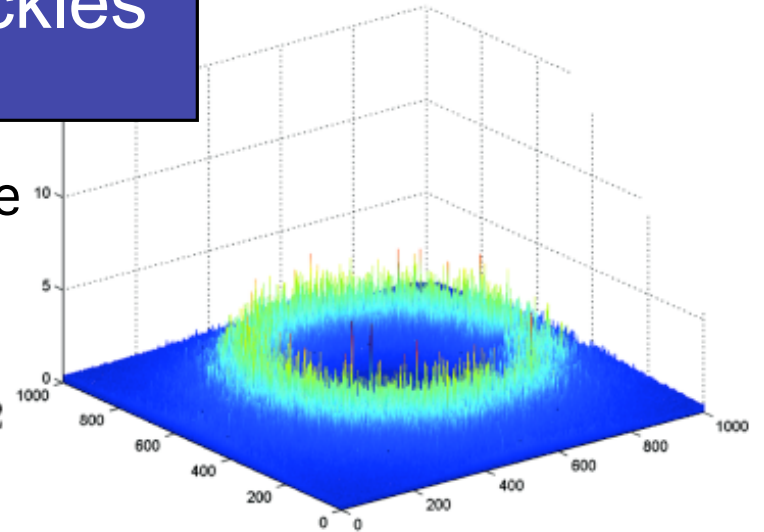


And is becoming bigger... And bigger... And bigger!!!

# A closer look at comparing speckles

For quantitative comparison of two speckle patterns take the standard correlation coefficient:

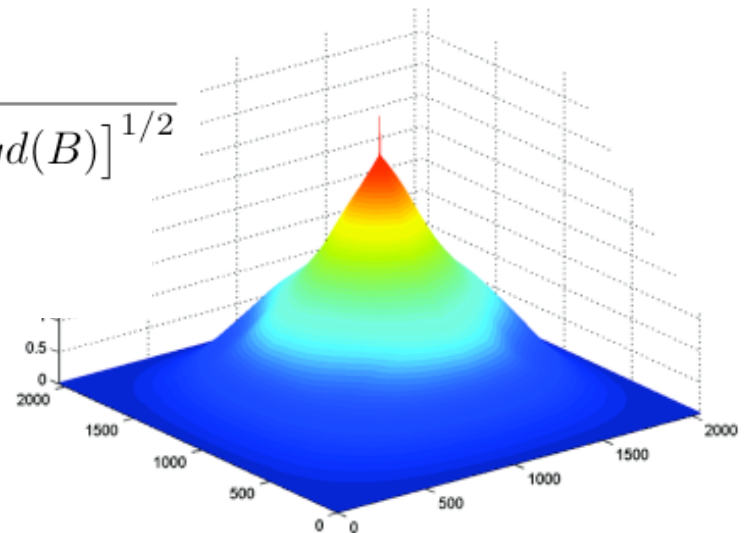
$$\rho(a, b) = \text{Cov}(a, b) \times \{ \text{Var}(a) \text{Var}(b) \}^{-1/2}$$



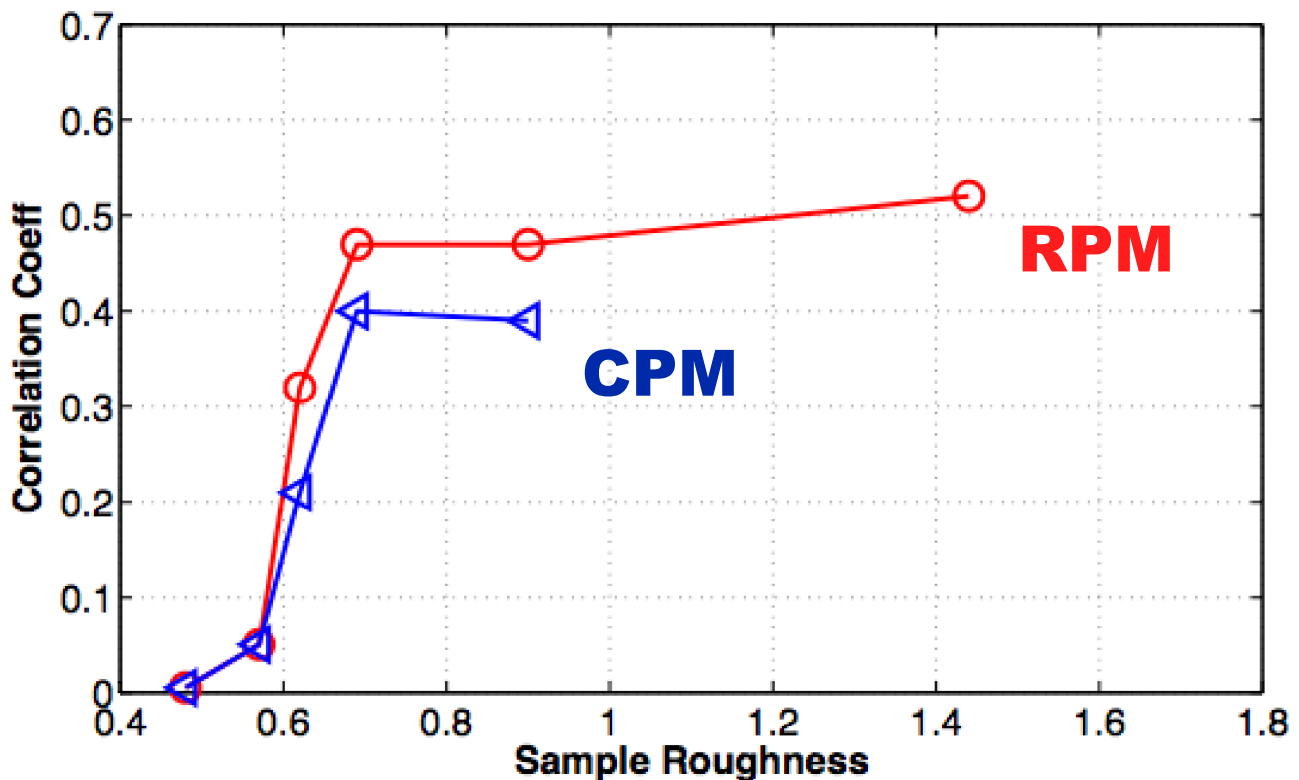
And write it in terms of auto and cross-correlation functions

$$\rho(A, B) = \frac{\sum [ \text{CCF}(A, B) - \text{Bkgd}(A, B) ]}{\sum [ \text{ACF}(A) - \text{Bkgd}(A) ] \sum [ \text{ACF}(B) - \text{Bkgd}(B) ]^{1/2}}$$

$r = 1$  for perfect correlation and  
 $\rho = 0$  for no correlation



# Experimental Results



**(1) Abrupt onset of memory**

**(2) Apparent saturation**

**(3) Max half of the domains remember**

**=> imperfect memory for  $T > 0$**

**(4) RPM slightly larger than CPM**

**=> partial RPM-CPM symmetry breaking**

**When we started there  
were no good theories**

**Now there are four!**

**Disorder-induced magnetic memory: Experiments and theories**

M. S. Pierce,<sup>1,2</sup> C. R. Buechler,<sup>1</sup> L. B. Sorensen,<sup>1</sup> S. D. Kevan,<sup>3</sup> E. A. Jagla,<sup>4</sup> J. M. Deutsch,<sup>4</sup> T. Mai,<sup>5</sup> O. Narayan,<sup>5</sup> J. E. Davies,<sup>6</sup> Kai Liu,<sup>6</sup> G. T. Zimanyi,<sup>6</sup> H. G. Katzgraber,<sup>7</sup> O. Hellwig,<sup>8</sup> E. E. Fullerton,<sup>8</sup> P. Fischer,<sup>9</sup> and J. B. Kortright<sup>9</sup>

<sup>1</sup>*Department of Physics, University of Washington, Seattle, Washington 98195, USA*

<sup>2</sup>*Materials Science Division, Argonne National Laboratory, Argonne, Illinois 60439, USA*

<sup>3</sup>*Department of Physics, University of Oregon, Eugene, Oregon 97403, USA*

<sup>4</sup>*Centro Atómico Bariloche, Comisión Nacional de Energía Atómica, (8400) Bariloche, Argentina*

<sup>5</sup>*Department of Physics, University of California, Santa Cruz, California 95064, USA*

<sup>6</sup>*Department of Physics, University of California, Davis, California 95616, USA*

<sup>7</sup>*Theoretische Physik, ETH Zürich, CH-8093 Zürich, Switzerland*

<sup>8</sup>*Hitachi Global Storage Technologies, San Jose, California 95120, USA*

<sup>9</sup>*Lawrence Berkeley National Laboratory, Berkeley, California 94720, USA*

(Received 4 January 2007; published 5 April 2007)

Beautiful theories of magnetic hysteresis based on random microscopic disorder have been developed over the past ten years. Our goal was to directly compare these theories with precise experiments. To do so, we first developed and then applied coherent x-ray speckle metrology to a series of thin multilayer perpendicular magnetic materials. To directly observe the effects of disorder, we deliberately introduced increasing degrees of disorder into our films. We used coherent x rays, produced at the Advanced Light Source at Lawrence Berkeley National Laboratory, to generate highly speckled magnetic scattering patterns. The apparently “random” arrangement of the speckles is due to the exact configuration of the magnetic domains in the sample. In effect, each speckle pattern acts as a unique fingerprint for the magnetic domain configuration. Small changes in the domain structure change the speckles, and comparison of the different speckle patterns provides a quantitative determination of how much the domain structure has changed. Our experiments quickly answered one long-standing question: How is the magnetic domain configuration at one point on the major hysteresis loop related to the configurations at the same point on the loop during subsequent cycles? This is called microscopic return-point memory (RPM). We found that the RPM is partial and imperfect in the disordered samples, and completely absent when the disorder is below a threshold level. We also introduced and answered a second important question: How are the magnetic domains at one point on the major loop related to the domains at the complementary point, the inversion symmetric point on the loop, during the same and during subsequent cycles? This is called microscopic complementary-point memory (CPM). We found that the CPM is also partial and imperfect in the disordered samples and completely absent when the disorder is not present. In addition, we found that the RPM is always a little larger than the CPM. We also studied the correlations between the domains within a single ascending or descending loop. This is called microscopic half-loop memory and enabled us to measure the degree of change in the domain structure due to changes in the applied field. No existing theory was capable of reproducing our experimental results. So we developed theoretical models that do fit our experiments. Our experimental and theoretical results set benchmarks for future work.

DOI: [10.1103/PhysRevB.75.144406](https://doi.org/10.1103/PhysRevB.75.144406)

PACS number(s): 75.60.Ej, 61.10.-i, 78.70.Dm, 07.85.Qe

**I. INTRODUCTION**

What causes magnetic hysteresis and how is it induced and influenced by coexisting microscopic disorder? This is the question that we address and provide answers to in this paper. We are able to provide additional information about this venerable old question because we have developed a way to directly probe the effect of disorder on the spatial structure of the microscopic magnetic domain configuration as a function of the applied magnetic field history. When we finished our experimental study, we discovered that our results could not be explained by any existing microscopic theories of magnetic hysteresis. So we developed several viable theoretical models. In this paper, we present our detailed experimental results and the theoretical models that we developed to explain them.

Magnetic hysteresis is fundamental to all magnetic storage technologies and consequently is a cornerstone of the

present information age. The magnetic recording industry deliberately introduces carefully controlled disorder into its materials to obtain the desired hysteretic behavior and magnetic properties. Over the past 40 years, such magnetic hardening has developed into a high art form. However, despite decades of intense study and significant recent advances, we still do not have a completely satisfactory microscopic understanding of magnetic hysteresis.

The exponential growth of computing power that fueled the information age has been driven by two technological revolutions: (1) The integrated circuit revolution and its exponential growth described by Moore’s law, and (2) the magnetic disk drive revolution and its exponential growth, which for the past decade has surpassed Moore’s law. Both of these mature technologies are rapidly approaching their fundamental physical limits. If the incredible growth rate of storage capacity in magnetic media is to continue, new advances in

our fundamental understanding of magnetic hysteresis are needed.

For the past 20 years, magnetic films with perpendicular anisotropy have been extensively studied for their potential to extend the limits of storage capacity. Early in 2005, the first commercial disk drives using perpendicular magnetic media became available. The system that we study here is a model for these perpendicular magnetic media. In this paper, we present our results on the effect of disorder on the correlations between the domain configurations in these systems.

To study the detailed evolution of the magnetic domain configuration correlations in our samples, we developed an x-ray scattering technique, coherent x-ray speckle metrology (CXSM). We illuminate our samples with coherent x rays tuned to excite virtual  $2p$  to  $3d$  resonant transitions in cobalt. The resulting resonant excitation of the cobalt provides our magnetic signal. The coherence of the x rays produces a magnetic x-ray speckle pattern. The positions and intensity of the speckles provide a detailed fingerprint of the microscopic magnetic domain configuration. Changes in the magnetic domain configuration produce changes in the speckle pattern. So by comparing these magnetic fingerprints versus the magnetic field history—by cross-correlating speckle patterns with different magnetic field histories—we obtain a quantitative measure of the applied-field-history-induced evolution of the magnetic domain configuration.

Here we report our results obtained by applying CXSM to investigate the effects of controlled disorder on the magnetic domain evolution in a series of Co/Pt multilayer samples with perpendicular anisotropy. We introduced disorder into the samples by systematically increasing the interfacial roughness of the Co/Pt multilayers during the growth process. We found that this disorder induces memory in the microscopic magnetic domain configurations from one cycle of the hysteresis loop to the next, despite taking the samples through magnetic saturation. Our lowest-disorder samples have no detectable cycle-to-cycle memory; their domain patterns are unique each time the sample is cycled around the major loop. As we increase the disorder, the cycle-to-cycle memory develops and grows to a maximum value, but never becomes perfect or complete at room temperature.

In this paper, we present our results for microscopic magnetic memory only along the major loop in the slow-field-sweep limit. In this limit, the measured hysteresis loop is the same over many decades of sweep rate. The hysteresis in this limit is often called rate-independent hysteresis, or quasi-static hysteresis. There are, of course, also interesting and important hysteresis effects that occur at high sweep rates. Our strategy was to study the simpler rate-independent hysteresis case before adding the additional physics, and complications, associated with high sweep rates. As we explain below, the disorder dependence of the rate-independent hysteresis in our system turned out to be remarkably rich and interesting. We do not discuss our results for rate-independent minor-loop memory in this paper, but we briefly reported them recently.<sup>1</sup>

The best modern microscopic disorder-based theories of magnetic hysteresis were built on the foundations of Barkhausen noise measurements.<sup>2</sup> Even in the rate-independent limit, the magnetization of a disordered ferro-

magnet does not change smoothly as the applied field is swept up and down. Instead, there are magnetic domain avalanches that produce magnetization jumps. These avalanches exhibit power-law size distributions indicating that many different size regions change their magnetization in jumps as the field is swept around the major hysteresis loop.

A comprehensive, recent review of Barkhausen noise studies—including a translation of Barkhausen's 1919 paper—is given in Ref. 3. For some materials in the rate-independent limit, the Barkhausen noise is independent of the magnetic sweep rate; these avalanches occur at fixed values of the applied field, independent of the sweep rate.<sup>4</sup>

Barkhausen measurements provide exquisite information about the time structure of the avalanches, but they usually do not provide any spatial information about the location of the avalanches. Because we directly measure the nanometer-scale spatial structure of the magnetic domain configuration changes, we obtain detailed information about the configuration evolution that cannot be obtained directly from the best classical Barkhausen noise studies or from their modern optical implementations.<sup>5</sup> Because there has been extensive theoretical work on Barkhausen noise, the corresponding field-history-dependent microscopic morphologies of the magnetic domain configurations have been indirectly inferred from the Barkhausen time signals via detailed computer simulations. For example, Sethna and co-workers have shown that the morphology for their random field Ising model (RFIM) is fractal in space. They provide a comprehensive review of their work in Ref. 2.

Taken together, the detailed fractal-in-time structure measured via the Barkhausen noise, and the extensive computer simulations by Sethna *et al.* imply that their magnetic domain configurations are fractal in space. Therefore, why not simply measure the correlations between the magnetic domain configurations directly? That is precisely what we do in this paper. There has been very little systematic, ensemble-level experimental work on the spatial evolution of the magnetic domain configurations,<sup>5,6</sup> but this information is readily available from the existing simulations. However, up until now almost all of the work has been done for pure RFIMs. Our experimental system and the new generation of perpendicular magnetic disk drive media have long-range dipole interactions. This means that new theories that include the dipolar interactions<sup>7</sup> will be required to understand these materials.

During our work, we unearthed three interesting aspects of our magnetic domain wall evolution. The first, called major-loop return-point memory (RPM), describes the magnetization for each point on the major loop. If this magnetization is precisely the same for each cycle around the major loop, then we have macroscopic major loop RPM. If, in addition, the microscopic magnetic domain configuration is also identical, then we have microscopic major-loop RPM. Our experiments show that our samples have perfect macroscopic major-loop RPM, but imperfect microscopic major-loop RPM at room temperature.

The second, called complementary-point memory (CPM), describes the inversion symmetry of the major loop through the origin. If the magnetization at field  $H$  on the descending branch is equal to minus the magnetization at field  $-H$  on the



ascending branch, then we have perfect macroscopic major-loop CPM. If, in addition, the magnetic domains are precisely reversed, then we have perfect microscopic major loop CPM. Our experiments show that our samples have perfect macroscopic major-loop CPM, but imperfect microscopic major-loop CPM at room temperature. In addition, we find that our measured values for the microscopic RPM are consistently a little larger than those for our microscopic CPM—thus the RPM-CPM symmetry is slightly broken.

The third, called half-loop memory (HLM), describes the degree of change in the magnetic domain configurations along a single branch of the major hysteresis loop. Our experiments show that disorder has a direct effect on how the domains evolve. The greater the disorder present in the sample, then the greater the observed changes in the domain configurations as the applied field is slowly adjusted to take the system along the major hysteresis loop. Our measured values for the HLM are consistently higher in the low-disorder samples than those present in the disordered samples.

We were inspired to do our experimental study by the beautiful work on the RFIM by Sethna *et al.*<sup>2</sup> We were therefore very surprised to discover that their model could not describe our experimental results. Their pure zero-temperature RFIM predicts perfect macroscopic and microscopic major-loop RPMs, but it does not agree with our experiments because it predicts essentially no microscopic major-loop CPM. It seems reasonable that their  $T > 0$  RFIM will predict perfect macroscopic RPM but imperfect microscopic RPM like that observed in our experiments, but this has not been tested. However, their model cannot predict our observed microscopic CPM and therefore it also cannot predict the slightly broken microscopic RPM-CPM symmetry that our experiments observe.

So, what physics is required to produce imperfect microscopic RPM and CPM with the slightly broken symmetry? There are two aspects to this question—the imperfection and the RPM-CPM symmetry breaking. Almost all models have perfect memory at  $T=0$  and imperfect memory for  $T > 0$ . And it seems likely that the imperfect memory that we observe could be caused by temperature effects, but this has not yet been established. On the other hand, no viable theoretical model for the slight RPM-CPM symmetry breaking existed. So we developed viable models. The key idea behind each of our models was to combine physics with spin-reversal symmetry with physics without spin-reversal symmetry. Then the spin-reversal-symmetric physics produces symmetric memory  $\text{RPM}=\text{CPM}$  and the nonsymmetric physics produces symmetry-broken memory  $\text{RPM} \neq \text{CPM}$ .

Within the standard RXIM models—viz., RAIM, RBIM, and RCIM, and RFIM where A denotes anisotropy, B denotes bond, C denotes coercivity, and F denotes field—the first three have spin-reversal symmetry, but the fourth (RFIM) does not. So one way to produce slightly symmetry-broken memory is to combine the RFIM with one of the symmetric models. Surprisingly, another way is to combine one of the symmetric models with vector spin dynamics because vector dynamics breaks the spin-reversal symmetry. We report our work on three viable models: Model 1 combines a pure RFIM with a pure RCIM; model 2 combines a

pure RAIM with vector spin dynamics; model 3 combines a pure RFIM with a pure spin-glass model.

We explored models 1 and 2 in the most detail. By tuning the model parameters, we were able to semiquantitatively match our experimentally observed disorder dependence and magnetic-field dependence of (i) the domain configurations, (ii) the shape of the major loops, (iii) the values of the RPM and CPM, and (iv) the slight RPM-CPM symmetry breaking.

Note that, in order to properly describe our observed magnetic domain configurations, we had to include the long-range dipolar interactions. In contrast to the Sethna *et al.* RFIMs that predict spatially fractal magnetic domain configurations,<sup>2</sup> our samples exhibit labyrinthine domain configurations due to their long-range dipolar interactions.

The remainder of this paper is organized as follows. Section II describes the physics of return-point memory and complementary-point memory. Section III describes our experiments, sample fabrication, structural characterization, magnetic characterization, and coherent x-ray speckle metrology characterization. Section IV describes our data analysis methodology. Section V describes the results of our data analysis. Section VI describes the theoretical models that we developed to account for the observed behavior of our system. Section VII presents our conclusions.

## II. MACROSCOPIC AND MICROSCOPIC RETURN-POINT MEMORY AND COMPLEMENTARY-POINT MEMORY

In his 1903 dissertation at Göttingen entitled “On the magnetization produced by fast currents and the operation of Rutherford-Marconi magnetodetectors,” Madelung presented his rules for magnetic hysteresis as illustrated in Fig. 1.

(1) *Major-loop return-point memory.* The magnetization of the sample at every point on the major loop is completely determined only by the applied field, and all first-order reversal curves starting from the major loop and going to saturation are uniquely determined by their starting point. The curve  $1 \rightarrow +S$  in Fig. 1 illustrates a first-order reversal curve.

(2) *Minor-loop return-point memory.* The magnetization of the sample at every point on the major loop is completely determined solely by the value of the applied field, even when the point on the major loop is reached starting from a point inside the major loop. This holds for every order reversal curve. The curve  $2 \rightarrow 1$  illustrates this property for a second-order reversal curve.

(3) *The memory deletion (wiping out) property.* The magnetization of the sample at every point on a reversal curve is precisely the same as that for its parent curve as soon the reversal curve returns to its parent. In this way, all memory of the previous field history between the initial departure from the parent and the return to the parent has been erased. This holds for every order reversal curve. The curve  $3 \rightarrow +S$  illustrates this for a third-order reversal curve.

(4) *The congruency property.* All return curves that start from reversal at the same value of the applied field have the same shape thereafter, independent of the entire previous applied field history.

(5) *The similarity property for initial magnetization*

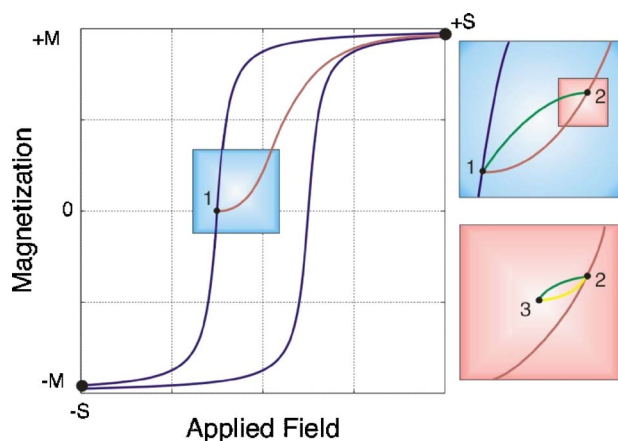


FIG. 1. (Color online) The topology of Madelung’s rules. (a) If the magnetization curves from point 1 to saturation are uniquely determined by the applied field at their departure point 1 from the major loop, then the system exhibits macroscopic major-loop return-point memory. If, after returning to point 1 on the major hysteresis loop, the system continues along the major loop, then the system exhibits macroscopic major-loop memory deletion (wiping out). (b) If the first-order reversal curve from point 2 back to the major loop arrives at its original departure point, then the system exhibits first-order macroscopic minor-loop return-point memory. (c) If the second-order reversal curve from point 3 back toward saturation passes through point 2, then the system exhibits second-order macroscopic minor-loop return-point memory. If thereafter it continues along the original curve from 1 to saturation, then the system exhibits macroscopic minor-loop memory deletion (wiping out).

curves. When any initial magnetization curve is reversed at point  $a$ , the reversed return curve to saturation will pass through the inversion symmetric point to  $a$  as it proceeds to saturation. As discussed below, we call the analogous property to the similarity property—for reversal curves that do not start from a point on the initial magnetization curve—the complementary-point memory property.

Madelung formulated his rules based on his careful experimental studies of different alloys of steel and published them in 1905 and 1912.<sup>8</sup> Because Madelung formulated his rules before the existence of magnetic domains was known, he considered only the macroscopic magnetization. Nevertheless, his rules still predict the macroscopic magnetization of “any typical” sample versus its applied field history. Madelung’s rules have truly been the foundation for all modern theories of hysteresis.

It is therefore surprising that Madelung’s rules are so rarely cited. Apparently this is because essentially all of the subsequent work has been focused on the Preisach model.<sup>9</sup> The obscurity of Madelung’s magnetic hysteresis work is particularly surprising because the Preisach model has been well known to be unphysical for a very long time due to its heavy reliance on phenomenology. There are however exceptions such as the recent work by Zirka and collaborators.<sup>10</sup>

Of course, Madelung’s rules do not apply to every magnetic system. For example, many systems exhibit accommodation, reptation, and magnetic viscosity effects, and all systems exhibit dynamic hysteresis effects. However, on the

other hand, Madelung’s rules do apply to an incredible number of magnetic systems under a vast range of conditions.

Now that we know that the microscopic magnetic domains are intimately involved in the production of magnetic hysteresis, we immediately come to the first question at the core of our investigation: How do the magnetic domains behave on the microscopic level. Do the domains remember—viz., return precisely to—their initial states, or does just the ensemble average remember? We show below that, at room temperature, some of the domains in our samples return to their original configurations and some do not, but nevertheless the macroscopic magnetization—set by the ensemble average—does return to its original value.

In other words, we find that our samples have perfect macroscopic RPM, but they have imperfect microscopic RPM at room temperature. In fact, our measured RPM values for each sample demonstrate a rich, complex behavior reflecting the fundamental physics of the magnetic domains. We quantitatively measured the fraction of the domains that remember and thereby demonstrated that the disorder has a profound impact on the microscopic RPM. As we tune the disorder, our samples develop microscopic RPM that starts from zero in the low-disorder limit and jumps to a saturated value in the high-disorder limit, but never becomes perfect at room temperature. Consequently, our experimental system is a finite-temperature realization of the “microscopic disorder-induced phase transition between no memory and perfect memory” predicted by Sethan and co-workers.<sup>2</sup>

The major loop for any typical magnetic system usually has an additional symmetry—it is symmetric about inversion through the origin. This inversion symmetry immediately raises the second question at the core of our investigation: How are the domains at the complementary points of the major loop related? Do the magnetic domains at the opposing points on the major loop evolve in a similar, but perhaps mirror correlated, fashion? We call this effect microscopic major loop CPM. The geometry of complementary-point memory is illustrated in Fig. 2.

Despite an incredible amount of effort since 1905, it has proven impossible to develop a simple, yet adequate, phenomenological model that can be used to treat all magnetic materials. We still do not have a phenomenological model for modern magnetic technology. In addition, although there has also been tremendous effort expended and progress achieved, it has similarly proven impossible to develop a general purpose micromagnetics model. We now know, based on recent theoretical work,<sup>2</sup> that the detailed magnetic hysteresis properties of real materials cannot be treated using standard mean-field methods. This is because the hysteresis depends on the interactions between each domain and a limited number of its neighbors, as well as between each domain and its local disorder. Consequently, our approach has been to determine to what extent the nanoscale domain-level physics of our experimental system obeys Madelung’s rules, and then to explore whether we can better understand the observed behavior using traditional (overly) simplified Ising models.

### III. EXPERIMENTAL ASPECTS

To measure the field-history-induced changes in the microscopic magnetic domain configurations, we developed co-

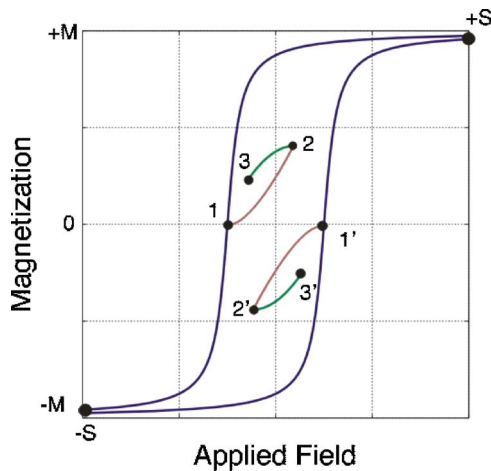


FIG. 2. (Color online) Geometry of complementary-point memory (CPM). (a) If the magnetization at point 1' is equal to that at point 1, then the system exhibits macroscopic major-loop CPM. If the domain configuration at point 1' is highly correlated with that at point 1, then the system exhibits microscopic major-loop CPM. (b) If the magnetization at point 2' is equal to that at point 2, then the system exhibits first-order macroscopic minor-loop CPM. If the domain configuration at point 2' is highly correlated with that at point 2, then the system exhibits first-order microscopic minor-loop CPM. (c) If the magnetization at point 3' is equal to that at point 3, then the system exhibits macroscopic second-order minor-loop CPM. If the domain configuration at point 3' is highly correlated with that at point 3, then the system exhibits second-order microscopic minor-loop CPM. In general, CPM can occur for any order of reversal.

herent x-ray speckle metrology.<sup>1,11,12</sup> Our CXSM experiments were performed at the Advanced Light Source at Lawrence Berkeley National Laboratory. A schematic diagram of the experimental apparatus is shown in Fig. 3. We used linearly polarized x rays from the third and higher harmonics of the beamline 9 undulator. The raw undulator beam was first reflected from a nickel-coated bremsstrahlung

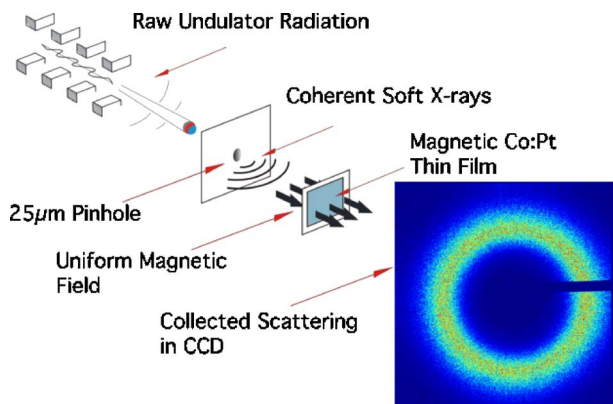


FIG. 3. (Color online) Schematic diagram of the experimental apparatus. Soft x rays from the undulator passed through a pinhole and were perpendicularly incident on the thin film samples. The x rays were scattered in transmission and were detected by a soft x-ray CCD camera. Not shown in this diagram is the electromagnet used to apply uniform magnetic fields perpendicular to the sample.

safety mirror and then passed through a water-cooled Be window to decrease unwanted light. The partially coherent incident beam from the undulator was passed through a 35  $\mu\text{m}$  diameter pinhole to select a transversely coherent portion. The sample was located 40 cm downstream of the coherence-selection pinhole. This provided transversely coherent illumination of about a 40  $\mu\text{m}$  diameter area of the sample. The transversely coherent x-ray beam was incident perpendicular to the sample surface and was scattered in transmission by the sample. The resonant magnetic scattering was detected by a soft x-ray charge-coupled-device (CCD) camera located 1.1 m downstream of the sample. Between the sample and the CCD camera we used a small blocker to prevent the direct beam from damaging the CCD.

The photon energy was set to the cobalt  $L3$  resonance at 778 eV. These photons resonantly excited virtual  $2p$  to  $3d$  transitions in the cobalt atoms and thereby provided our magnetic sensitivity. The intensity of the raw undulator beam was  $2 \times 10^{14}$  photons/s, the intensity of the coherent beam was  $2 \times 10^{12}$  photons/s, and the intensity of the scattered beam was  $2 \times 10^7$  photons/s. We typically measured each speckle pattern for 10–100 s, so the total number of photons in each CCD image was  $10^8$ – $10^9$ .

The applied magnetic field was provided by an in-vacuum water-cooled electromagnet allowing *in situ* adjustment of the magnetic field during the experiment. The return path for the electromagnet consists of an external soft Fe yoke that feeds field to vanadium permanent pole pieces that are integral to the vacuum chamber. The pressure inside the chamber during our experiments was typically  $10^{-8}$  Torr. The in-vacuum electromagnet provided magnetic fields up to 11 kOe.

#### A. Sample fabrication and structural characterization

Our thin-film samples were grown by magnetron sputtering in the San Jose Hitachi Global Storage Technology Laboratory on smooth, low-stress, 160-nm-thick silicon nitride membranes. The samples had 20-nm-thick Pt buffer layers, and 2.3-nm-thick Pt caps to prevent oxidation. Between the buffer layer and the cap, the samples had 50 repeating units of a 0.4-nm-thick Co layer and a 0.7-nm-thick Pt layer. While the six samples had identical multilayer structure they were grown at different argon sputtering pressures to tune the disorder in the samples. During growth, we adjusted the deposition times to keep the Co and Pt layer thicknesses constant over the entire series. For low argon pressures, the sputtered metal atoms arrive at the growth substrate with considerable kinetic energy which locally heats and anneals the growing film. This leads to smooth Co/Pt interfaces produced at a low sputtering pressure. For higher argon sputtering pressures, the sputtered atoms arrive at the growth substrate with minimal kinetic energy, thereby resulting in rougher Co/Pt interfaces. The resulting roughness is cumulative through the samples.<sup>13</sup> The magnetocrystalline anisotropy at the Co/Pt interface forces the magnetization to align perpendicularly to the surface of the film. Our samples were grown at six different sputtering pressures: 3, 7, 8.5, 10, 12, and 20 mTorr. Due to the important and interesting magnetic

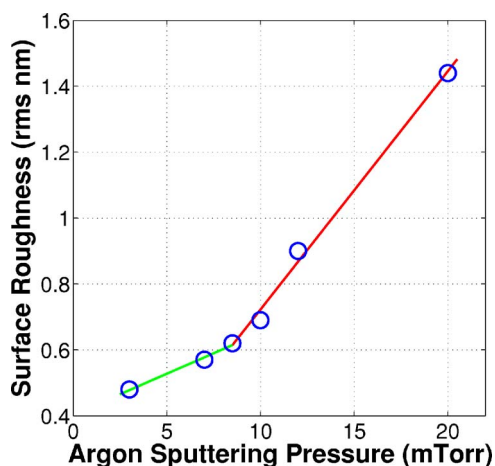


FIG. 4. (Color online) The measured rms roughness from AFM and x-ray reflectivity measurements plotted versus the argon sputtering pressures. The interfacial roughness increases as the sample growth pressure increases. Below 8.5 mTorr, the roughness increases slowly as indicated by the left (green) fit line. Above 8.5 mTorr the roughness increases much more rapidly as indicated by the right (red) fit line. This behavior is very similar to that observed by Ref. 13 in sputtered Nb/Si multilayers.

properties, these samples and others very similar in form and structure have been studied in different experiments.<sup>14,15</sup>

The rms roughness for the samples was measured in the Almaden Hitachi Global Storage Technology Laboratory using two different methods. First, we measured the roughness by scanning the sample surface with an atomic force microscope (AFM) and calculating the rms roughness from the AFM images (see Fig. 4). Since our samples have conformal roughness, the rms roughness of the surface is a reasonable measure of the internal rms roughness. However, to directly probe the internal rms roughness, we also did the x-ray reflectivity measurements shown in Fig. 5. The reflectivity data were fitted using a Debye-Waller factor to determine the roughness. Instead of the system possessing thermal fluctuations, the displacements from the average height are randomly distributed and fixed. The rms roughness values from the x-ray measurements agreed with those from the AFM measurements, confirming the conformal roughness of our samples. The rms roughness values are shown in Fig. 4 and are listed in Table I. We found that the rms roughness for the 3 mTorr sample is about 0.48 nm and that it increases to 1.44 nm for the 20 mTorr sample.

### B. Magnetic characterization

We measured the major hysteresis loops for all of our samples using both Kerr magnetometry at the San Jose Hitachi Global Storage Technology Laboratory and alternating gradient magnetometry (AGM) at the University of California—Davis. The measured major loops shown in Fig. 6 exhibit clear changes that are related to the increasing roughness. The two low-disorder films (3 and 7 mTorr) exhibited classic Kooy-Enz<sup>16</sup> soft loops with low remanence and abrupt nucleation transitions. Between 7 and 8.5 mTorr, there is an abrupt transition to loops that do not show a clear

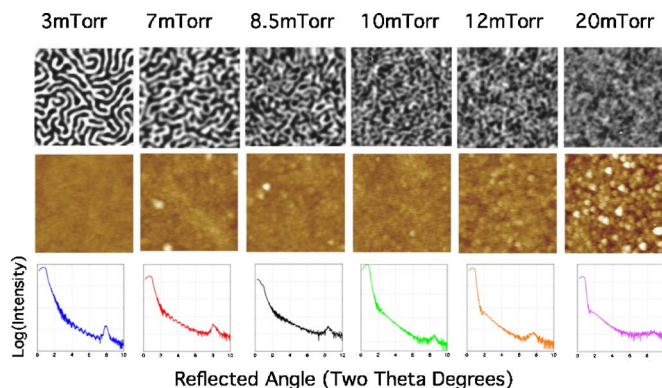


FIG. 5. (Color online) The measured MFM images, AFM images, and x-ray reflectivity curves for the six samples. The MFM images evolve from clear labyrinthine patterns for the low-rms-roughness samples to visually highly disordered patterns for the high-rms-roughness samples. However, the persistence of the annular shape of the speckle patterns—even for the highest roughness samples—reveals an underlying labyrinthine order. The MFM images show  $3 \times 3 \mu\text{m}^2$  areas. The AFM images show that the top surface of the samples becomes rougher at higher pressures. The AFM images show  $1 \times 1 \mu\text{m}^2$  areas. Both the x-ray reflectivity curves and the AFM images were used to determine the rms roughness for each sample.

nucleation region. Between 8.5 and 20 mTorr, the ascending and descending slopes of the loop remain approximately the same, but the loops gradually widen until the full magnetic moment is left at remanence. The values of the nucleation, coercive, and saturation fields each exhibit a roughly linear dependence upon the sample roughness. This behavior is shown in Fig. 7. In addition, we also found via magnetometry that all of our films exhibit perfect macroscopic *major-loop* and *minor-loop* RPM and CPM.

The AGM was used to measure the saturation magnetization of the samples. The measured saturation magnetizations are reported in Table I; they should be compared against the value of  $M_s = 1400 \text{ emu/cm}^3$  for pure cobalt. It is interesting to note that, with increasing interfacial roughness, the coercivity and saturation fields increase and the nucleation field

TABLE I. Measured magnetic characteristics of our six samples.

Sample <sup>a</sup>	$\sigma_{\text{rms}}$ <sup>b</sup>	$M_s$ <sup>c</sup>	$H_n$ <sup>d</sup>	$H_c$ <sup>e</sup>	$H_s$ <sup>f</sup>
3 mTorr	0.48	1360	1.58	0.16	3.7
7 mTorr	0.57	1392	0.64	0.68	5.0
8.5 mTorr	0.62	1136	1.68	1.42	5.5
10 mTorr	0.69	1069	1.45	1.87	6.5
12 mTorr	0.90	1101	1.23	2.74	9.5
20 mTorr	1.44	918	-1.81	5.89	14.2

<sup>a</sup>Our samples are labeled by their growth pressure in mTorr.

<sup>b</sup>The measured rms interfacial roughness in nanometers.

<sup>c</sup>The measured saturation magnetization of Co in  $\text{emu/cm}^3$ .

<sup>d</sup>The nucleation field measured from positive saturation.

<sup>e</sup>The measured coercive field in kOe.

<sup>f</sup>The measured saturation field in kOe.

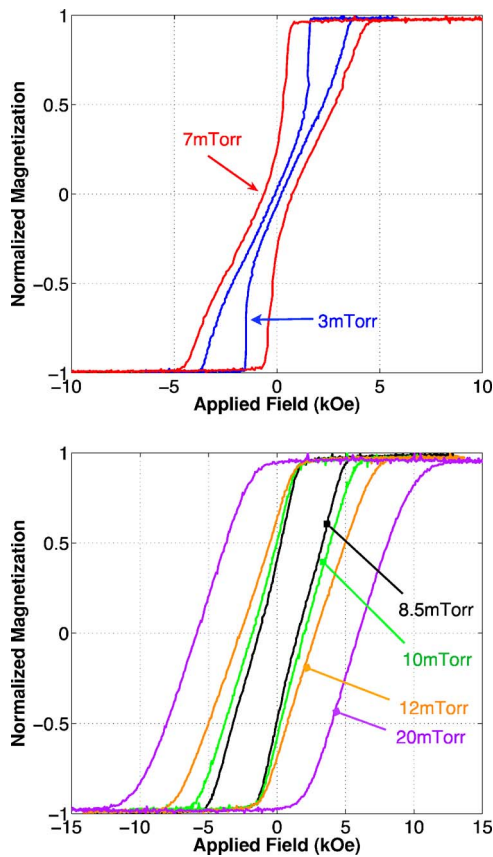


FIG. 6. (Color online) Measured magnetic hysteresis loops for our samples. Note that the shape of the major hysteresis loops change abruptly above the “critical roughness” value—which occurs between the 7 and 8.5 mTorr samples—and that the areas inside the major loop increase as the disorder increases past the critical roughness value. The two low-rms-roughness samples exhibit classic Kooy-Enz behavior characterized by a sharp nucleation region and low remanant magnetization, whereas the high-rms-roughness samples exhibit an almost constant slope.

decreases linearly with the roughness; the measured saturation magnetizations also decrease as the disorder increases.

### C. Coherent x-ray speckle metrology

To measure the field-history-induced changes in the correlations between the microscopic magnetic domain configurations, we developed coherent x-ray speckle metrology. The magnetic sensitivity of CXSM is provided by virtual  $2p$  to  $3d$  resonant magnetic scattering. We produce a transversely coherent beam by passing the partially coherent beam from the undulator through a  $35\ \mu\text{m}$  diameter circular pinhole to select a highly transversely coherent portion. The beam selected by the spatial filter is largely coherent over the entire illuminated area. Due to this large uniform transverse coherence, the resonant magnetic scattering produces the speckle patterns that we use to track the field-history-induced evolution of the magnetic domains. We explain our analysis methodology for the magnetic speckle patterns in the next section.

What information does x-ray speckle metrology provide about the magnetic domains, and why do we not simply

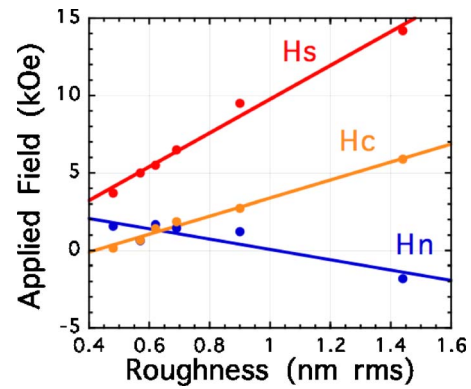


FIG. 7. (Color online) The measured magnetic characteristics for our samples plotted versus their measured rms roughness. The coercive, nucleation, and saturation fields are denoted by  $H_c$ ,  $H_n$ , and  $H_s$ , respectively. Note the apparently linear dependence of these properties on the rms roughness.

study the magnetic domains in real space? This is the venerable old question about diffraction versus microscopy. The conventional answer is that they are complementary: use conventional beam diffraction to obtain information about the ensemble average, and use microscopy to obtain information about the individual defects. There are two limiting cases of conventional diffraction studies. When the diffraction pattern consists of Bragg peaks, then the information that conventional diffraction provides is the ensemble average of the long-range order. When the diffraction pattern consists of diffuse scattering, then the information that conventional diffraction provides is the ensemble average of the short-range order. In our labyrinthine systems, there is no long-range magnetic order, and consequently the diffraction is diffuse. With an unfiltered beam we observe only a diffuse annulus which contains information about the strength (amplitude) of the magnetic domains, the mean spacing of the magnetic domains, and the correlation length of the magnetic domains. We have performed such studies already and the results will be presented elsewhere.

Fully coherent diffraction changes that paradigm because the precise configuration of the speckles provides detailed information about the defects, or in our case about the configuration of the magnetic labyrinths. In the Bragg case, the information is about the defects in the crystalline order. In the diffuse case, the information is about the defects in the short-range order. In fact, in two or three dimensions, if the speckle pattern is sampled with sufficient wave-vector resolution, then all of the real-space information is contained in the speckle pattern and can be recovered using oversampling speckle reconstruction.<sup>17</sup> However, no successful oversampling speckle reconstructions have yet been reported for magnetic domains, though holography methods have recently been demonstrated in similar systems.<sup>18</sup> Consequently, our objective was not to extract the complete real-space information, but instead to directly determine the changes between the correlations of the magnetic domain configurations prepared via different applied-field histories—specifically, without requiring the oversampling speckle reconstruction of our speckle image magnetic fingerprints.

So what information does our magnetic speckle metrology provide? We illuminate a 40  $\mu\text{m}$  diameter circle on the sample so our ensemble average is over that region. Consequently, each speckle in our speckle pattern consists of an Airy pattern with a characteristic size in reciprocal space of  $2\pi/40 \mu\text{m}^{-1}$ . The second important length scale in our problem is set by the width of the magnetic domains in the labyrinth state. This width is 200 nm, and consequently the corresponding characteristic size in reciprocal space is  $2\pi/200 \text{nm}^{-1}$ ; this sets the mean radius of our annular speckle patterns. In principle, our speckle patterns can provide spatial information down to  $\lambda/2=0.8 \text{nm}$ , but in practice—due to the strong disorder in our labyrinths—our speckle patterns really only contain information set by the region where the diffuse scattering is measurable, namely, between the inside and outside radii of the annulus. For our samples this was from about 110 to 260 nm in real space.

As argued above, all of the physical information that can be obtained using our incident wavelength is contained within the limited range that contains measurable scattering intensity. Our incident wavelength is fixed by the magnetic resonant scattering condition for cobalt so  $\lambda \approx 1.6 \text{nm}$ . For this wavelength, diffraction provides information ranging from 0.8 nm for backscattering with  $2\theta=180^\circ$  up to 40  $\mu\text{m}$  set by the illumination area. At our usual sample-to-camera separation, the pixel size of our camera translates into a real-space resolution of 13  $\mu\text{m}$  and the total coverage of the camera translates into a real-space resolution of 270 nm. The angular size of our beamstop translates into 70 nm. Since  $70 < 110 \text{nm}$ ,  $260 < 270 \text{nm}$ , and  $27 < 40 \mu\text{m}$ , our camera and our beamstop do not limit the spatial scales that we can access. Instead, the limits are set only by the disorder levels in our samples.

The intensity  $I(q_r, q_\theta)$  of each speckle located at position  $(q_r, q_\theta)$  is proportional to the square modulus  $|a_q|^2$  of the scattering amplitude  $a_q$  of the corresponding Fourier component of the magnetic density  $\rho_{\text{mag}}(q_r, q_\theta)$ . So by taking the square root of the intensity of our speckle pattern, we can first calculate and then visualize the result as a map of the magnetic density amplitudes for all of the most important Fourier components. Each component located at  $\mathbf{q}=(q_r, q_\theta)$  tells us the amplitude of an infinite-spatial-extent complex-valued exponential density component  $\exp(i\mathbf{q} \cdot \mathbf{r})$  multiplied by our illumination function, which is roughly equal to one inside the illumination circle and zero outside. Imagine a large number of these complex-valued oscillating exponentials, each one oriented along the direction  $\theta$  with amplitude  $\sqrt{I}$  and wave vector  $q_r$ .

So how many of these Fourier components do we measure? The area of our observed annulus in reciprocal space is given by

$$A_q = \pi q_{\text{max}}^2 - \pi q_{\text{min}}^2$$

and the area of each one of our speckles in reciprocal space is given by

$$A_{\text{speckle}} = \pi \delta q_{\text{speckle}}^2$$

so the number of speckles inside the annulus is given by

$$A_{\text{annulus}}/A_{\text{speckle}} \approx 30\,000.$$

In other words, we directly measure this many Fourier components of the magnetization density. Because the speckle intensity outside the annulus is negligible, the corresponding Fourier components outside the annulus are also negligible. So we directly obtain information about all of the non-negligible Fourier components of the magnetic density that produce the magnetic scattering within the speckled annular region that we measure.

On the other hand, modern computer control and computer image analysis should enable modern magnetic x-ray microscopy to obtain ensemble-averaged information about the magnetic domains. This is certainly worth pursuing, and we are just beginning such studies.

Speckle contrast, the normalized standard deviation of the intensity, is generally used as a measure of the quality of the produced speckle patterns. As the diffuse scattering envelope is azimuthally symmetric about  $q_r=0$ , it is correct to define the speckle contrast  $\sigma_{\text{con}}^2(q_r)$  as

$$\sigma_{\text{con}}^2(q_r) = \frac{1}{\langle I \rangle} \sqrt{\sum_k^N \frac{(I_k - \langle I \rangle)^2}{N-1}}$$

for small steps of  $q_r$  where the sum is carried out over all  $N$  (the number of data points included in each step). Using this calculation, the contrast present in our speckle patterns typically ranges from 0.6 to 0.4, with a small dip in values over the peak scattering. This interesting variation of the speckle contrast as it depends upon  $q_r$  is quite reminiscent of the speckle contrast studies by Retsch and McNulty<sup>19</sup> across absorption edges and could provide useful information if properly understood.

#### IV. DATA AND DATA ANALYSIS

The typical evolution of the speckle patterns for one-half cycle around the major hysteresis loop for the 3 mTorr sample is schematically illustrated in Fig. 8 and the corresponding measured speckle patterns are shown in Fig. 9. Starting at positive saturation there is no magnetic contrast—all the magnetic domains are aligned with the field—consequently there is no magnetic scattering. As we descend from positive saturation the magnetic domains nucleate and produce a magnetic speckle pattern that is shaped like a cookie (disk). When we reach zero applied field, the magnetic domains have grown so much that they fill the entire sample; in this limit they must interact, and their interaction produces the donut-shaped (annular) speckle pattern. When we reach the reversal region, the domain density is again low, and so the associated speckle pattern is again cookie shaped.

##### A. Correlation coefficients

To quantitatively compare the magnetic domain configurations versus the applied magnetic field history, we calculate the normalized correlation coefficients between pairs of our measured images acquired for different applied field histories. To date, our work has been primarily based on the nor-

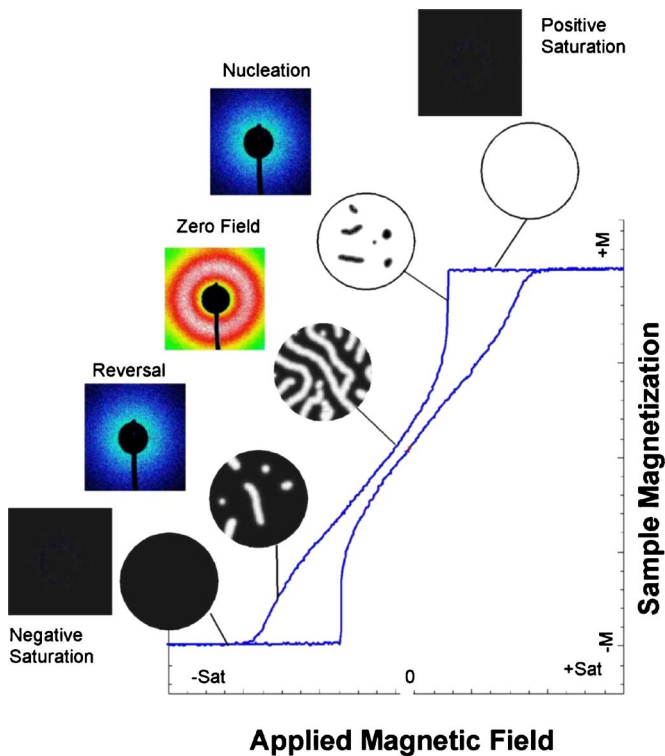


FIG. 8. (Color online) Measured major hysteresis loop for the 3 mTorr sample. The measured magnetic speckle patterns collected at different field values along the major loop are shown inside the square insets and an artist's rendition of the corresponding magnetic domain configurations are shown inside the circular insets.

malized cross correlation of these magnetic speckle patterns—our magnetic speckle fingerprints. However, this comparison can be done in reciprocal space—as we have primarily been doing up until now—or in real space as we are just beginning to do.

Some of our initial experimental work in real space is illustrated Fig. 10 which shows the magnetic domains in our 8.5 mTorr sample measured using x-ray magnetic microscopy.<sup>20</sup> These images were recorded at the Co L3 edge using XM-1 at the ALS and were taken on the descending major loop; the left panel shows the domains at  $H = -0.50$  kOe and the right panel shows the domains at  $H = -1.00$  kOe. The correlation coefficients obtained from our real-space normalized cross-correlation analysis of the domain patterns agree with our correlation coefficients obtained via our standard reciprocal-space normalized cross-correlation analysis of the corresponding speckle patterns. Therefore we believe that our real-space and reciprocal-space methods will prove to be complementary.

Our normalized cross-correlation analysis procedure in reciprocal space is illustrated in Figs. 11–13. Figure 11 shows the speckle fingerprints measured in reciprocal space; again the left panel shows the fingerprint at  $H = -0.5$  and the right panel shows the fingerprint at  $H = -1.0$  kOe. Figure 12 shows the calculated autocorrelation functions for these two speckle fingerprints. Note that both of these consist of a broad smooth “mountain” with a sharp “tree” on top of it.

The mountain corresponds to the diffuse scattering envelope from the short-range magnetic ordering and the tree

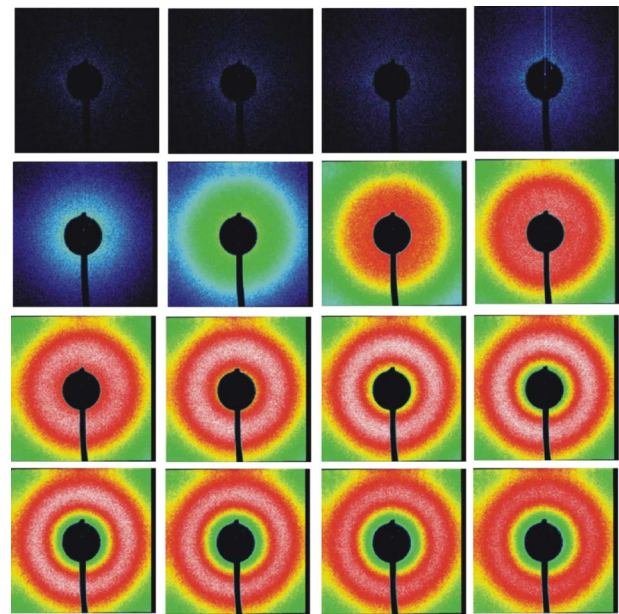


FIG. 9. (Color online) Measured CCD magnetic speckle images for about the first half of the ascending major loop for the low-disorder 3 mTorr sample. The dark region in the center is a blocker inserted to eliminate the direct beam from the image. These magnetic speckle patterns were collected at fixed values of the applied field as the field was monotonically increased in steps from negative saturation. The speckle images associated with the applied magnetic field values are shown—from left to right and from top to bottom—for the following applied field values:  $-3.0, -2.5, -2.0, -1.75, -1.5, -1.25, -1, -0.75, -0.5, -0.25, 0, 0.25, 0.5, 0.75, 1,$  and  $1.25$  kOe.

corresponds to the coherent scattering from the entire illuminated area. Figure 13 shows the calculated cross-correlation function for the two speckle fingerprints shown in Fig. 12. Again there is a diffuse mountain with a coherent tree on top of it.

We want to use the coherent components of these auto- and cross-correlation functions to compute the normalized correlation coefficient. We extract the volume ( $V$ ) of each tree and then we calculate the ratio

$$\rho(a, b) = \frac{V(a \otimes b)}{[V(a \otimes a)V(b \otimes b)]^{1/2}}$$

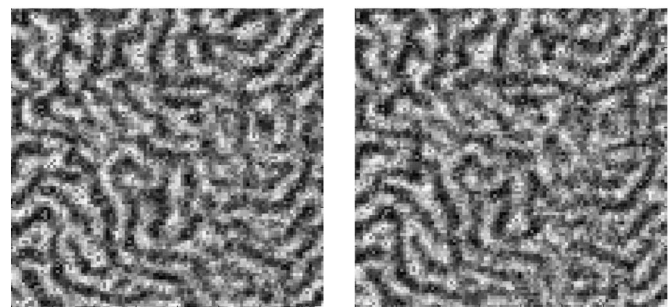


FIG. 10. Two representative magnetic x-ray microscopy images for our 8.5 mTorr sample at  $H = -0.50$  (Top) and  $-1.00$  kOe (Bottom). These images show  $2.2 \times 2.2 \mu\text{m}^2$  areas.

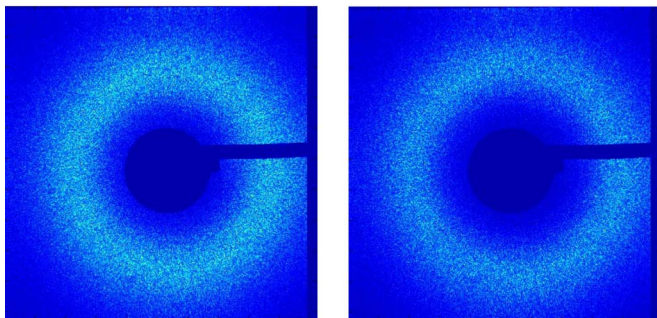


FIG. 11. (Color online) Two magnetic speckle patterns for our 8.5 mTorr sample shown for  $H = -0.50$  (Top) and  $-1.00$  kOe (Bottom).

The resulting normalized correlation coefficient  $\rho(a, b)$  measures the normalized degree of correlation between any two speckle patterns. We use it to quantify the degree of correlation between pairs of speckle patterns which in turn is our measure of the degree of correlation between the corresponding magnetic domain patterns. When  $\rho(a, b) = 1$  the two magnetic domain patterns are identical, and when  $\rho(a, b) = 0$  the two magnetic domain patterns are completely different.

In general, the value of  $\rho$  specifies the degree of correlation between the two speckle patterns which in turn are proportional to the Fourier coefficients of the magnetization density for the two magnetic domain configurations. Because our correlations are based on the intensity, we are unable to determine the sign of the correlations—we cannot distinguish correlation from anticorrelation. This is essentially Babinet's principle.

### B. Data analysis

We now sketch the details of our correlation coefficient calculations. To determine the correlation between two speckle patterns, we generalized the standard correlation coefficient for two random variables  $a$  and  $b$ , which is given by

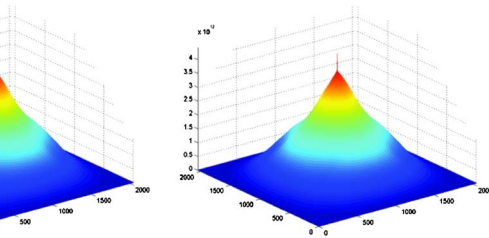
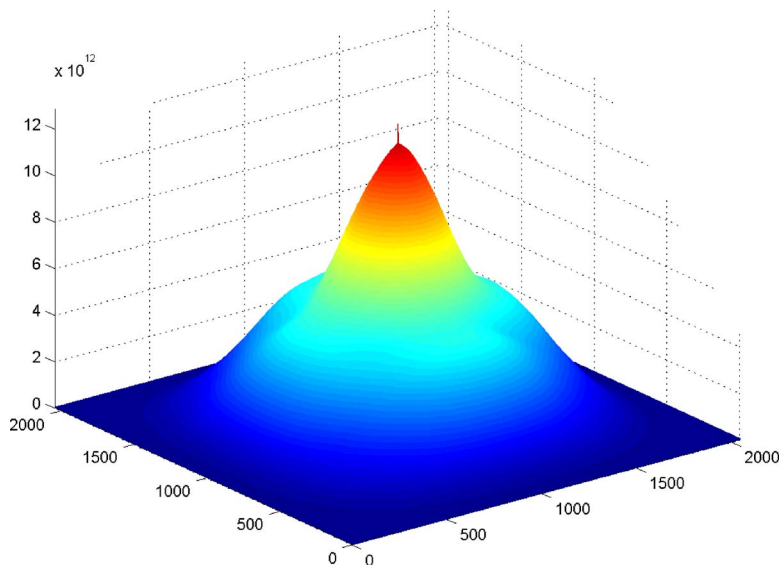


FIG. 12. (Color online) Two autocorrelation functions for the two magnetic speckle patterns shown in Fig. 11. The coherent speckle information is contained in the sharp peak that rides on the top of the large diffuse scattering signal. The autocorrelation functions are shown over the full  $2049 \times 2049$  pixel area. The vertical scale extends from 0 to  $4 \times 10^{12}$ .

$$\rho(a, b) = \text{Cov}(a, b) \times \{\text{Var}(a)\text{Var}(b)\}^{-1/2},$$

to the equivalent expression in terms of the background-subtracted cross-correlation function ( $\mathcal{F}_{\text{CCF}}$ ) and the background-subtracted autocorrelation functions ( $\mathcal{F}_{\text{ACF}}$ ) of the speckle pattern intensities  $I_a(q_x, q_y)$  and  $I_b(q_x, q_y)$

$$\rho(a, b) = \frac{\sum \mathcal{F}_{\text{CCF}}(a, b)}{\left(\sum \mathcal{F}_{\text{ACF}}(a) \sum \mathcal{F}_{\text{ACF}}(b)\right)^{1/2}}$$

where the sums run only over the trees so that the background-subtracted auto- and cross-correlation functions contain only coherent scattering contributions.

We used the standard fast Fourier transform (FFT) to calculate the auto- and cross-correlation functions, but we first verified that the FFT produces precisely the same results as slow, sliding cross correlation. Our speckle fingerprint images are  $1024 \times 1024$  pixels, so they produce cross-correlation images with  $2049 \times 2049$  points. The coherent speckle information, which is 2–3 pixels wide in the speckle patterns, is transformed into a peak 5–7 pixels wide in the correlation map. Figure 13 shows a typical cross-correlation map calculated using the two entire speckle patterns. Note that the shape of the mountain under the coherence tree is

FIG. 13. (Color online) Cross-correlation function between the two speckle patterns shown in Fig. 11. The coherent speckle information is contained in the sharp peak that rides on the top of the large diffuse scattering signal. The cross-correlation function is shown over the full  $2049 \times 2049$  pixel area. The vertical scale extends from 0 to  $4 \times 10^{12}$ .



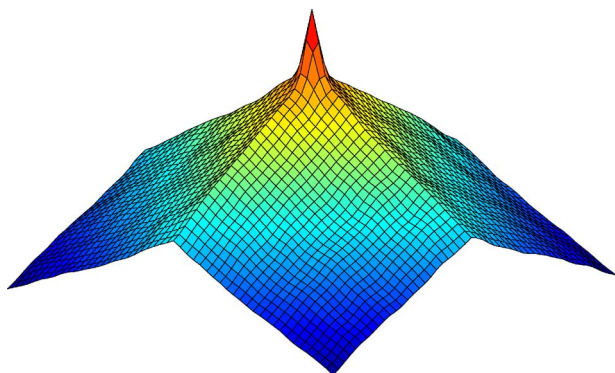


FIG. 14. (Color online) The cross-correlation function calculated by comparing small regions in the respective speckle images. The coherent speckle signal (the spike shown in yellow) is clearly visible and is located at the peak of the large diffuse background signal (the roof-shaped structure shown in blue).

shaped like a rounded cone. When the tree gets small—as the two speckle patterns become almost uncorrelated—the rounded shape makes it tricky to subtract the background properly.

To provide information about the quality of our normalized cross-correlation values, we divided the whole speckle pattern into 8–15 square regions containing  $100 \times 100$  pixels within which the intensity was nearly constant. In this way we removed the distortion produced by the shadow of the blocker and its support arm, and by camera defects and burns.

This piece-by-piece analysis made it much easier to separate the tree from the mountain. Because the variation in the average intensity over the small regions is much smaller than that over the entire image, the mountain now decays linearly away from the tree as shown in Fig. 14. Consequently, the small regions could always be reliably fitted with simple linear functions. This made it much easier and more reliable to subtract the background.

It is also very useful to note that this type of speckle analysis completely separates the coherent signal from the diffuse, incoherent scattering present in an image. Indeed, so long as the speckle signal is identifiable and separable, then any incoherent signal is eliminated. This calculation is capable of introducing some error; however, it is usually not sufficient to detract from the values obtained for the correlation coefficients. Even when the cross correlation becomes difficult to identify, the correlation coefficient  $\rho(a, b)$  is still normalized by the autocorrelation of each image which remains well defined and comparably large.

## V. EXPERIMENTAL RESULTS

As explained in the previous section, we used normalized correlation coefficients to extract information about the correlations between the magnetic domain configurations versus their applied-field history.

We addressed the following questions. Are the domains precisely the same each time we go around the major hysteresis loop? How are the domains related at the complemen-

tary points on the major loop? How are the domains related for different points within the same (ascending or descending) branch of the major loop? The first two questions are about major-loop microscopic RPM and CPM, or interloop correlations. The third question is about major-loop microscopic half-loop memory values that probe the intrabranched correlations. We present our answers to these questions in turn below.

### A. Major-loop microscopic return-point memory and complementary-point memory

The first question that we addressed was whether our samples exhibited major-loop microscopic RPM. To do so, we compared pairs of speckle patterns collected at the same point on the major loop, but separated by one or more full excursions around the major loop. The second question that we addressed was whether our samples exhibited major-loop microscopic CPM. To do so, we compared pairs of speckle patterns collected at one point on the major loop with the speckle patterns collected at the inversion-symmetric complementary point on subsequent cycles.

Our results for each sample are shown in Fig. 15, where the measured magnetic field dependence of the RPM and CPM correlation coefficients for each sample is shown. The data shown are for many excursions around each major loop. We did not observe any RPM or CPM for the 3 mTorr sample. The 7 mTorr sample exhibited an extremely small RPM and CPM—so small that we could not determine whether there was any RPM-CPM symmetry breaking. For all of our disordered samples, i.e., for 8.5 mTorr and above, we measured nonzero RPM and CPM values that had their RPM-CPM values slightly symmetry broken—our measured CPM coefficients are consistently a little smaller than the corresponding RPM coefficients. It is worth noting again that we verified with magnetometry that our samples demonstrated perfect macroscopic return-point memory.

In order to properly compare the memory of the different samples, it is helpful to plot them using the same scale. By dividing each actual measured magnetization value by the saturation magnetization for each sample we obtain a relative measure of the magnetization values. The value  $M/M_S$  is known as the reduced magnetization  $m$ . Figure 16 shows our major-loop microscopic RPM and CPM correlation coefficients, measured at room temperature for three values of the reduced magnetization  $m = -0.4, 0$ , (the coercive point), and  $+0.4$  for each sample. The RPM and CPM curves are plotted versus the sample's measured rms roughness. As noted above, our smooth samples have essentially zero RPM and CPM values. In contrast, all of our rough samples exhibit RPM and CPM correlation coefficients that increase and saturate as the roughness increases, but never grow to unity. This increase starts precisely where the major loops change from being nucleation dominated to being disorder dominated.

In addition, our measurements establish the following interesting trends about the RPM and the CPM.

(1) Neither correlation coefficient depends on the number of intermediate loops between the correlated speckle pat-

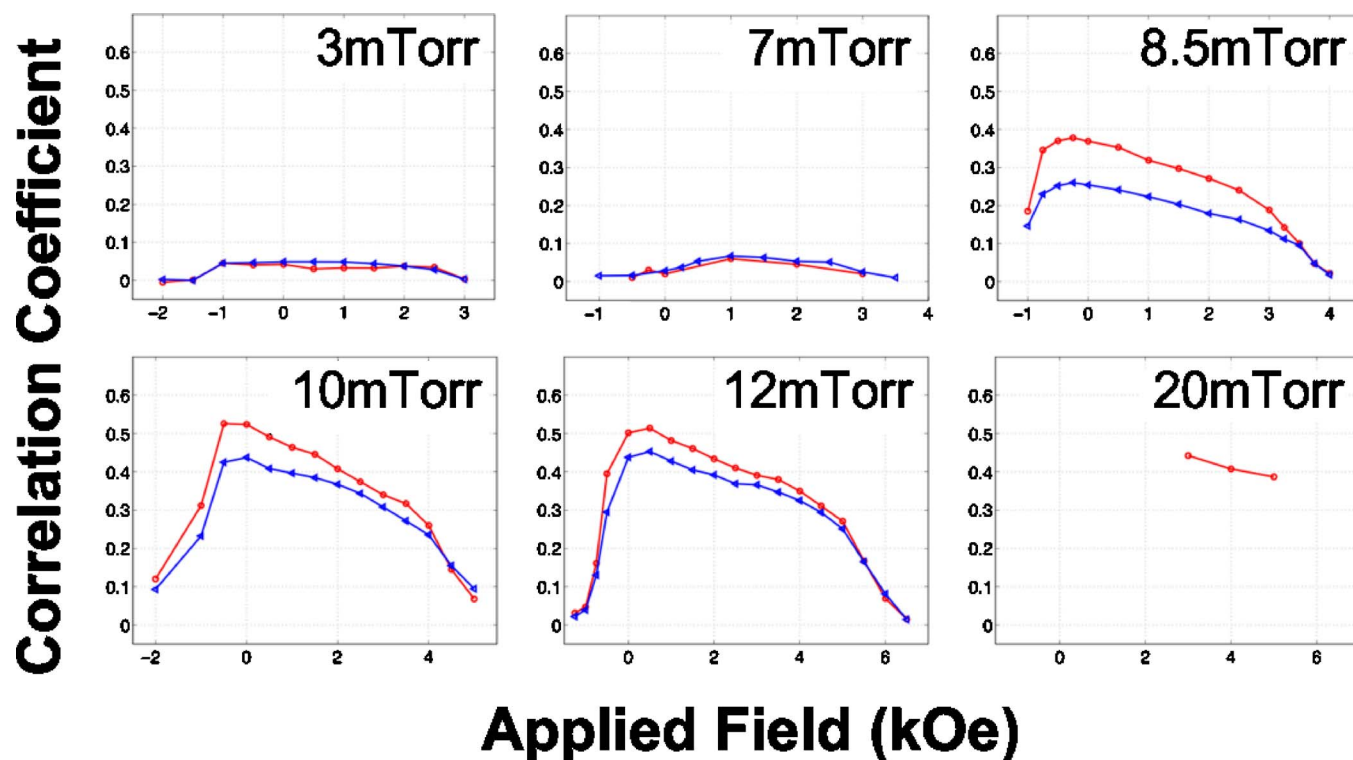


FIG. 15. (Color online) The measured RPM coefficients (red circles) and CPM coefficients (blue triangles) for all six of our samples along their major loop. The 3 mTorr sample (top left) shows no evidence of any memory effects. The 7 mTorr sample (top center) shows the possibility of an extremely small nonzero RPM and CPM. For each of the more disordered samples there is a sharp rise in the RPM and CPM that correlates with the initial domain growth followed by growth to a maximum value and then by a slow decrease as the sample is taken toward reversal.

terns. This indicates that the deterministic components of the RPM and CPM are essentially stationary. This implies that the deterministic component of the memory in our system is largely reset by bringing the sample to saturation. It also strongly suggests that the same disorder is largely producing at least the deterministic component of both the RPM and the CPM.

(2) The RPM correlation coefficients are consistently a little larger than the CPM correlation coefficients. This demonstrates that the system acts in nearly the same way under positive and negative magnetic fields. So this implies that much of the disorder must have spin-reversal symmetry. This might be produced by random anisotropy, random bonds, or random coercivity, but not by random fields. This also suggests that the right physics might be captured by combining a RFIM model (which has RPM but essentially no CPM) with any of the other microscopic models (RAIM, RBIM, and RCIM), which all predict identical RPM and CPM.

(3) The correlation coefficients are largest near the initial domain reversal region. This suggests that the subsequent decorrelation is produced by the domain growth.

(4) The correlation coefficients decrease monotonically to their minimum values near complete reversal. This suggests that the decorrelation is produced by the domain reversal.

### B. Half-loop memory: The domain configuration correlations within a single branch of the major loop

We next studied the correlations between the magnetic domain configurations within a single half loop—i.e., the

correlations within a single ascending, or a single descending, half loop. We looked for evidence that the evolution of the magnetic domains depended upon the disorder present in the sample. Does the level of the disorder influence how quickly or slowly the domain pattern evolves?

To study this question, we computed the normalized cross-correlation coefficient between the speckle patterns taken along a single ascending or descending half loop. As we cycled each sample from negative to positive saturation, we stopped many times at fixed field values to record the speckle patterns. By cross-correlating two speckle patterns collected on the same trip along the major hysteresis loop, we are able to determine how the domain configuration is changing.

Denoting the ordered set of descending speckle patterns by  $1, 2, 3, 4, \dots$ , we then calculated the correlation coefficients between all of the pairs of these speckle patterns:

$$\rho(1,1), \rho(1,2), \rho(1,3), \rho(1,4), \dots;$$

$$\rho(2,1), \rho(2,2), \rho(2,3), \rho(2,4), \dots;$$

$$\rho(3,1), \rho(3,2), \rho(3,3), \rho(3,4), \dots; \text{ etc.}$$

This allowed us to correlate each of the domain configurations against all of the previous and subsequent measured configurations within the same descending branch of the major loop.

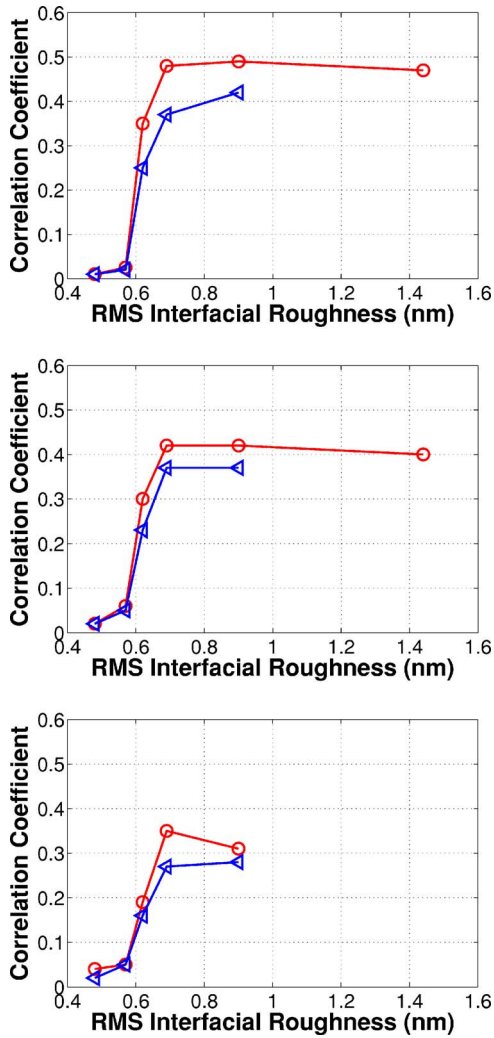


FIG. 16. (Color online) RPM (red circles) and CPM values (blue triangles) measured for different sample magnetizations plotted versus the respective measured rms roughness. The top figure shows the results obtained for the reduced magnetization  $m = -0.4$ . The middle shows the results for  $m = 0.0$  which is the coercive point. The bottom shows the results for  $m = +0.4$ . Note that the RPM and CPM exhibit similar rapid growth followed by apparent saturation independent of the value of  $m$ .

When the reference pattern was taken to be the image with its reduced magnetization  $m = -0.4$ , the resulting half-loop memory curves are shown versus the applied field in the top panel of Fig. 17; the bottom panel shows the same HLM curves plotted versus the reduced magnetization. Note the nice data collapse that occurs for the plots versus  $m$ .

We found that the  $m = -0.4$  HLM curves for our samples exhibit a subtle, but interesting, dependence on their disorder. Although the HLM curves in the bottom panel of Fig. 17 look remarkably similar, the low-disorder curves are systematically above the high-disorder curves. This indicates that the intraloop domain configurations in the low-disorder samples are a little more persistent than those in the high-disorder samples. This is consistent with the idea that the domain widths in the low-disorder samples can expand and contract as the applied field is changed, whereas the domains

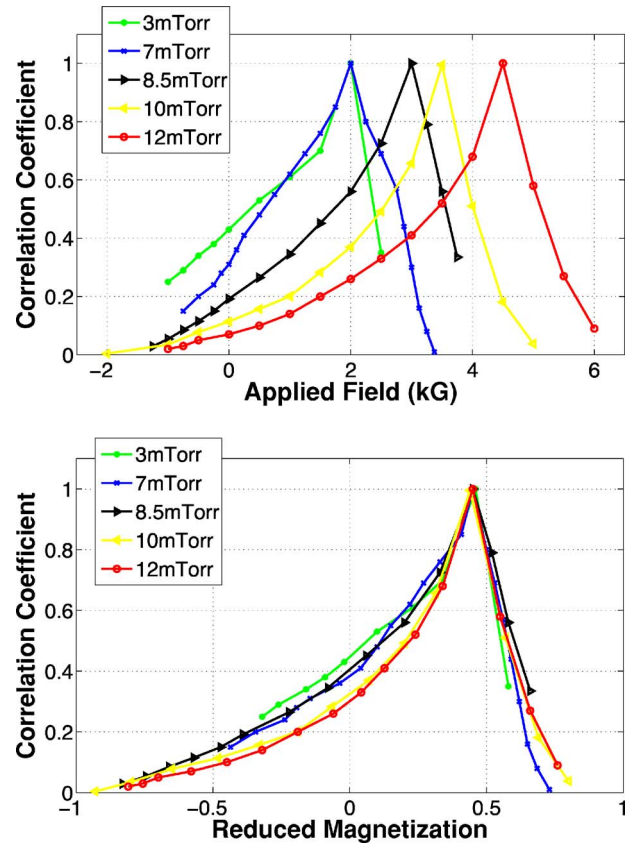


FIG. 17. (Color online) The half-loop memory (HLM) curves for  $m = -0.4$ . The top panel shows the HLM curves for the samples versus the applied field values. The bottom panel shows the HLM curves versus the reduced magnetization values. For each sample, a reference image is taken at  $m = -0.4$  and then cross-correlated with all previous and subsequent images collected on the same trip along one-half of the major hysteresis loop. Thus, the degree of correlation is determined between the speckle pattern from each image with the speckle pattern obtained at  $m = -0.4$  on the same trip along the major hysteresis loop.

in the high-disorder samples must break and reform.

Figure 18 shows the systematic evolution of our measured HLM curves versus each reference image for the 3, 7, 8.5, 10, and 12 mTorr samples. Up until now, there have been no analytic predictions or simulations for the shapes of, or the evolution of, these measured HLM curves.

## VI. OUR THEORETICAL MODELS

Our experimental results represent direct measurements of the effects of controlled disorder on microscopic return-point memory and complementary-point memory. How can we understand our experimental results in the light of the current microscopic disorder theories, and, in particular, how does nature produce the RPM-CPM symmetry breaking? For spin models that are bilinear in spin (excluding the external field term), one might expect that the microscopic evolution of spins from a completely saturated state would lead to the same speckle patterns (or, with thermal noise or dynamical instabilities, to the same distribution of speckle patterns),

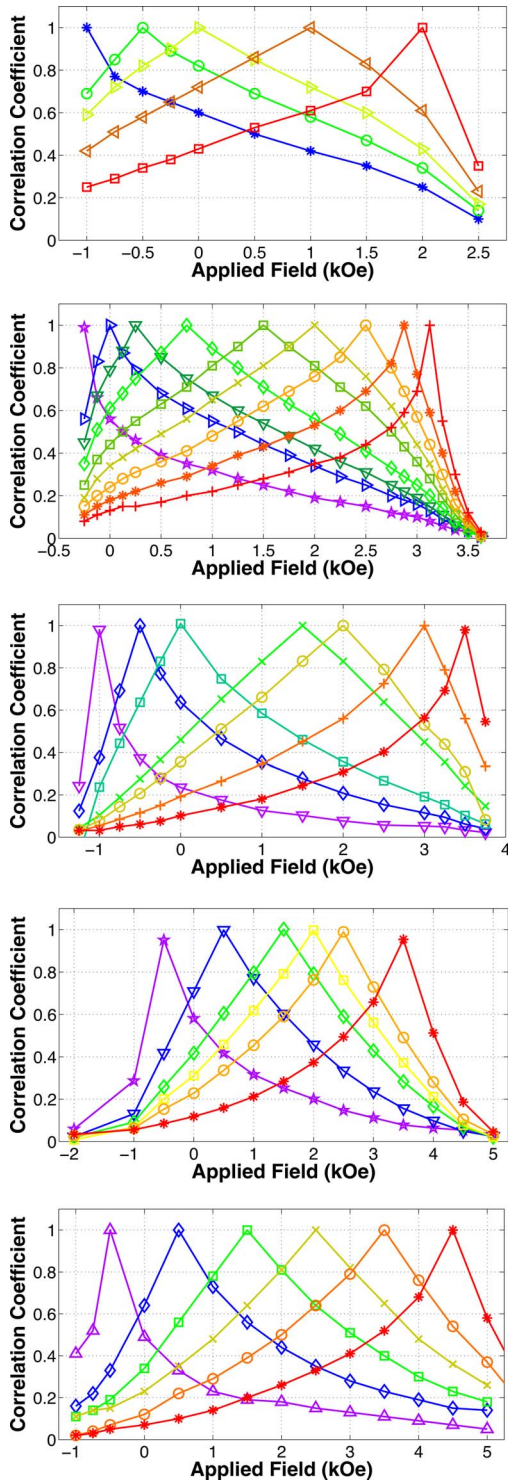


FIG. 18. (Color online) Our measured half-loop memory (HLM) curves plotted versus the applied field values. The HLM curves for each sample are shown for each possible reference speckle pattern for that sample, i.e., the magnetic speckle pattern for every measured applied field value is used as the reference pattern for one of the curves shown. The respective reference field values are easily identified as the points on the HLM curves where the HLM value is unity. From top to bottom, the panels show the 3, 7, 8.5, 10, and 12 mTorr sample HLM curves. In each case, the magnetization of the sample was increased from negative to positive saturation.

whether one starts from a very large positive or a very large negative applied field. As a consequence, the RPM and CPM correlation coefficients would be the same. Our experimental results show that this is not the case, and we have found that this apparent experimental small RPM-CPM symmetry breaking imposes strong constraints on any theory designed to describe the experiments.

In many theoretical descriptions of the magnetization process in systems with an easy anisotropy axis, the local magnetization is described as a scalar quantity, since it is assumed that to a good approximation the magnetization must point along this easy axis. Starting from this point, we can obtain a number of different models according to the additional ingredients that we add. The well-known Ising model is obtained by coupling neighboring spins ferromagnetically.

Many different microscopic disorder-induced memory systems have been constructed by introducing different types of disorder. The random anisotropy Ising model is produced by varying the local deviations from normal of the easy axis.<sup>21</sup> The random bond Ising model is produced by varying the strength of the ferromagnetic coupling between spins.<sup>22</sup> The random coercivity Ising model is produced by varying the coercive field that is necessary to flip each spin.<sup>23</sup> The Edwards-Anderson spin-glass (EASG) model is produced by randomly choosing the signs of the bonds. An additional interesting and extensively studied possibility is to consider disorder entering in the form of a random local field acting on each spin. In this case, the model is called the random field Ising model.<sup>2</sup> For compactness, below we will refer to the above models using the acronym RXIM.

There is an important distinction among the previous models. The RAIM, RBIM, and RCIM are all spin-inversion symmetric. So at zero temperature they show perfect RPM and CPM. If temperature is included, then both the RPM and CPM become less than 1, but they remain equal. The only model that is not spin symmetric, and can thereby explain the experimentally observed difference between RPM and CPM, is the RFIM. The RFIM alone is too drastic because for all but extremely high disorder it has essentially no CPM. This suggests one possible approach to explain our results: a theory that combines the RFIM with one of the other RXIMs possessing full CPM could produce a system that possesses slightly symmetry-broken RPM and CPM. Another possible route to the broken RPM-CPM symmetry is via spin-glass models. The standard spin-glass model has perfect RPM and CPM at  $T=0$ , but when coupled to random fields it exhibits imperfect CPM. Some of the relevant properties are summarized in Table II.

We have explored the first two models, denoted models 1 and 2 below, in the most detail. Specifically we tuned the model parameters to make the simulations behave as closely as possible like our experimental results. Both models were able to semiquantitatively match our experimentally measured behavior for (i) the domain configuration morphology, (ii) the shape of the major loops, (iii) the values of the RPM and CPM coefficients, and (iv) the small RPM-CPM symmetry breaking, versus both the disorder level and the magnetic-field history.

We also explored one more model that was designed to produce the observed small RPM-CPM symmetry breaking

TABLE II. Symmetries and memories of our microscopic disorder-based hysteresis models.

Disorder model	RPM	CPM	Spin-inversion symmetry	Time-reversal symmetry
RAIM	Perfect	Perfect	Yes	Yes
RBIM	Perfect	Perfect	Yes	Yes
RCIM	Perfect	Perfect	Yes	Yes
RFIM	Perfect	Small	No	Yes
EASG	Perfect	Perfect	Yes	Yes

with the minimum physics: model 3 combines the RFIM with a spin-glass model. However, for this model, we have not yet tried to tune the model parameters to match the detailed experimental behavior. So we present it here as a minimal model that can produce a small RPM-CPM symmetry breaking that is qualitatively similar to that observed in our experiments.

Model 1 combines a pure RFIM with a pure RCIM.<sup>24,25</sup> The essential idea was to produce a theory that combines the pure RFIM—with perfect zero-temperature RPM but essentially no CPM—with one of the other random Ising models possessing full CPM to thereby produce a model that possesses the experimentally observed slightly symmetry-broken RPM and CPM.

Model 2 explores the consequences of the type of dynamics used by the simulations to change the orientation of a spin.<sup>26</sup> All of the typical RXIM simulations use selection and update methods which are unchanged under a global spin flip. The next level of sophistication beyond simple scalar spin flips is to use the vector Landau-Lifschitz-Gilbert (LLG) equation to describe the classical dynamics of the magnetic spins. However, this equation of motion is not spin symmetric. Consequently, the system will evolve differently than it does for simple spin-flip dynamics. In fact, we found that the major loop for model 2 does not exhibit perfect complementary symmetry.

Model 3 explores the consequences of mixing a RFIM with a spin-glass model.<sup>27</sup> Once again, because the RFIM has RPM but essentially no CPM, and the spin-glass model has both RPM and CPM, this model can be adjusted to exhibit a small RPM-CPM symmetry breaking.

The underlying symmetries and the predicted zero- and finite-temperature behavior of the RPM and CPM for the standard RXIMs and for the EASG model are shown in Table II. The entries in this table show the memories for the zero-temperature models. For the corresponding finite-temperature models, all of the “perfect” memories should be replaced by “imperfect.” The label “small” for the CPM represents the fact that at very high disorder the RFIM will show imperfect CPM. Our three models are presented and discussed one by one in more detail below.

### A. Model 1: RCIM plus RFIM

The first model that we explored simulates localized magnetic moments that lie in a plane and point perpendicular to

it. The local magnetization is taken to be a scalar variable  $\phi$ . We include in model 1 the long-range dipolar interactions, the short-range exchange interactions, and some sort of quenched disorder to simulate the effect of the interfacial roughness. In order to obtain more realistic results within a reasonable computational time, we used a continuous variable  $\phi$ , instead of an Ising-like discrete variable. The numerical advantages provided by a continuous variable have previously been discussed in detail in Ref. 24.

The total Hamiltonian for model 1 is

$$H = \alpha \int d\mathbf{r} \left( -\frac{\phi(\mathbf{r})^2}{2} + \frac{\phi(\mathbf{r})^4}{4} \right) - h \int d\mathbf{r} \phi(\mathbf{r}) + \beta \int d\mathbf{r} \frac{|\nabla\phi(\mathbf{r})|^2}{2} + \gamma \int d\mathbf{r} d\mathbf{r}' \phi(\mathbf{r})\phi(\mathbf{r}')G(\mathbf{r},\mathbf{r}'). \quad (1)$$

For more details see Ref. 24.

The first term gives the local energy of the magnetic dipoles, favoring (but not forcing) the values  $\phi = \pm 1$ . The second term includes the effect of an external magnetic field  $h$ , and the third term provides the continuum version of a local ferromagnetic interaction. The dipolar interaction kernel  $G$  is defined on a discrete numerical lattice by  $G(\mathbf{r},\mathbf{r}') = 1/|\mathbf{r} - \mathbf{r}'|^3$  for  $\mathbf{r} \neq \mathbf{r}'$ , whereas  $G(\mathbf{r},\mathbf{r}) \equiv 0$ . It has been shown that this particular regularization adopted at short distances does not play a crucial role in the results.<sup>25</sup>

Disorder is included through the random spatial variation of  $\alpha$ , namely,  $\alpha(\mathbf{r}) = \bar{\alpha}[1 + \omega_0\eta(\mathbf{r})]$ , where  $\eta(\mathbf{r})$  is a random spatial variable uniformly distributed between +1 and -1. Consequently, the constant  $\omega_0$  controls the overall strength of the disorder. This way of introducing disorder corresponds to that in the RCIM. Other forms of introducing disorder in the system (particularly random anisotropy and random bond) should also be explored.

As anticipated above, model 1 is spin symmetric, and consequently it will always predict RPM values equal to its CPM values. To explore the possibility that they could become different due to the existence of some symmetry-breaking field we introduced disorder in the field through  $h(\mathbf{r}) = \bar{h}[1 + \omega_1\eta(\mathbf{r})]$ . We always set  $\omega_1 \ll \omega_0$ , so that the amount of disorder in the RFIM component was always much smaller than that in the RCIM component. The time evolution of the system is obtained through overdamped dynamics of the type

$$\frac{\partial\phi(\mathbf{r})}{\partial t} = -\frac{\delta H}{\delta\phi(\mathbf{r})} + \sqrt{2k_B T}\xi(t) \quad (2)$$

where for convenience time has been rescaled and  $\xi(t)$  is an uncorrelated white noise that simulates the effects of a temperature  $T$  on the system.

Through a rescaling procedure, two of the coefficients in the Hamiltonian can be forced to take fixed values. In fact, we will assume that by appropriate time, space, and field rescaling, the coefficients of the ferromagnetic and dipolar interactions (namely,  $\beta$  and  $\gamma$ ) have been made equal to fixed values. For convenience in the simulations, these values were taken to be  $\beta=2$  and  $\gamma=0.19$ . The new parameters on

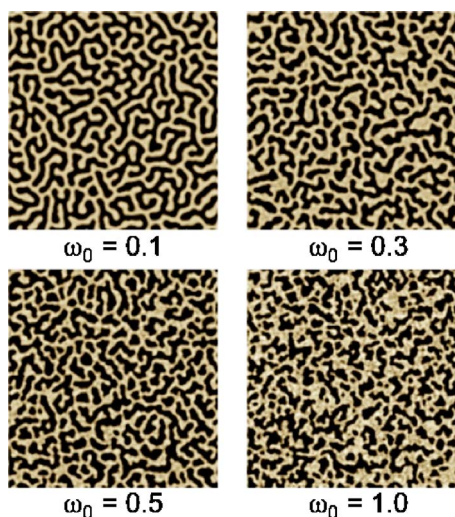


FIG. 19. (Color online) Simulated magnetic domain patterns for model 1 showing four different values of  $\omega_0$  at the coercive point. The simulation was started with a large applied field to saturate the magnetization in the positive direction. Then the applied field was slowly reversed in small steps to the coercive point, allowing the domain configuration time to come to equilibrium after each step.

which the model depends are now the rescaled values of  $\alpha$ ,  $h$ , and  $T$ . The results presented below correspond to simulations with  $\alpha=1.8$  and  $k_B T=2 \times 10^{-4}$  for different values of the disorder set by  $\omega_0$  and  $\omega_1$ , and as a function of the external field  $h$ .

We tuned the model parameters to reproduce the experimental conditions. We started at magnetic saturation by applying a large external field  $h$ , so that all the local moments point in the same direction. We then reduced the external field in small steps and obtained the “equilibrium configuration” by numerically solving the Hamiltonian equation until stationarity was obtained. Of course, the resulting equilibrium configuration is actually metastable. An example of the simulated magnetic domain configurations is shown in Fig. 19 for different applied fields.

By using our scalar model with a ratio between the random field component and the random coercivity component of  $\omega_1/\omega_0=0.04$ , we obtained the disorder-dependent correlation coefficients shown in Fig. 20. They were calculated using the domain configurations obtained from the simulation.

### 1. Effects of combined coercivity disorder and field disorder on memory

Now that we have demonstrated that a combined RCIM plus RFIM can be tuned to describe the results of our experiment quite well, it is natural to ask about the generic behavior of this combined model. In particular, how does its memory depend on its two disorders—the disorder in the coercivity and the disorder in the random field? We used a simple discrete-spin simulation to explore this question for both zero and finite temperature. Our simulations were performed on a  $64 \times 64$  grid of dipolar Ising spins. In dimensionless units, where the near-neighbor interaction energies are unity,  $J=1$ , our parameters were as follows: the random

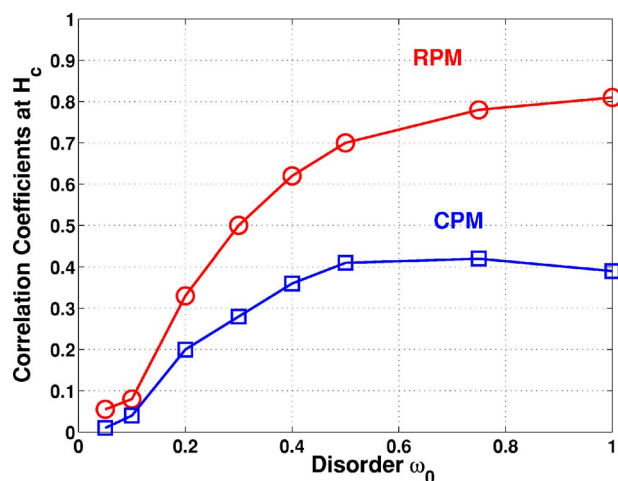


FIG. 20. (Color online) The calculated RPM (red circles) and CPM (blue squares) values versus disorder for model 1 at finite temperature. Note that the simulated evolution for model 1 is very similar to that of the experimentally measured RPM and CPM values. See Fig. 16 for comparison with experimental results.

field disorder was distributed normally with mean 0 and standard deviation  $x/3$ ; the random coercivity disorder was distributed normally with mean 0 and standard deviation  $y$ . Note that  $x$  and  $y$  are the horizontal and vertical scales in Fig. 21.

Our results for  $T=0$  are shown in Fig. 21. Note that the RPM is perfect for both the RFIM and the RCIM, and that it is also perfect for any linear combination of the RFIM and RCIM. The CPM is perfect for the pure RCIM for all values of the random coercivity disorder, but the CPM is imperfect for the pure RFIM for all nonzero values of the random field disorder. The perfect CPM for both the pure Ising model and pure RCIM have perfect negative CPM values,  $\rho_{\text{CPM}}=-1$ . Consequently the magnetic domains at the complementary point are perfectly anticorrelated with the magnetic domains at the return point.

Our results for  $T=0.1$  also are shown in Fig. 21. Note that the RPM for the pure Ising model is near zero, and that the RPM for the pure RFIM increases as the random field disorder is increased—it grows from zero with no random field disorder to about 1.0 at the highest disorders we explored. The RPM for the pure RCIM also increases as the random coercivity disorder is increased—it grows from zero with no random field disorder to 1.0 at the highest disorders we explored. The CPM for the pure Ising model is near zero. The CPM for the pure RFIM increases as the random field disorder is increased—it grows from zero with no random field disorder to about +0.4 at the highest disorders we explored. The CPM for the pure RCIM increases as the random coercivity disorder is increased—it grows from zero with no random field disorder to  $-1.0$  at the highest disorders we explored. It is interesting to note that the magnitude of the correlations and anticorrelations is larger for the RCIM than the RFIM over the same range. The spin-inversion symmetry of the RCIM pushes the system toward anticorrelation, favoring the same microscopic spin evolution on both sides of the major hysteresis loop. In contrast, because the RFIM

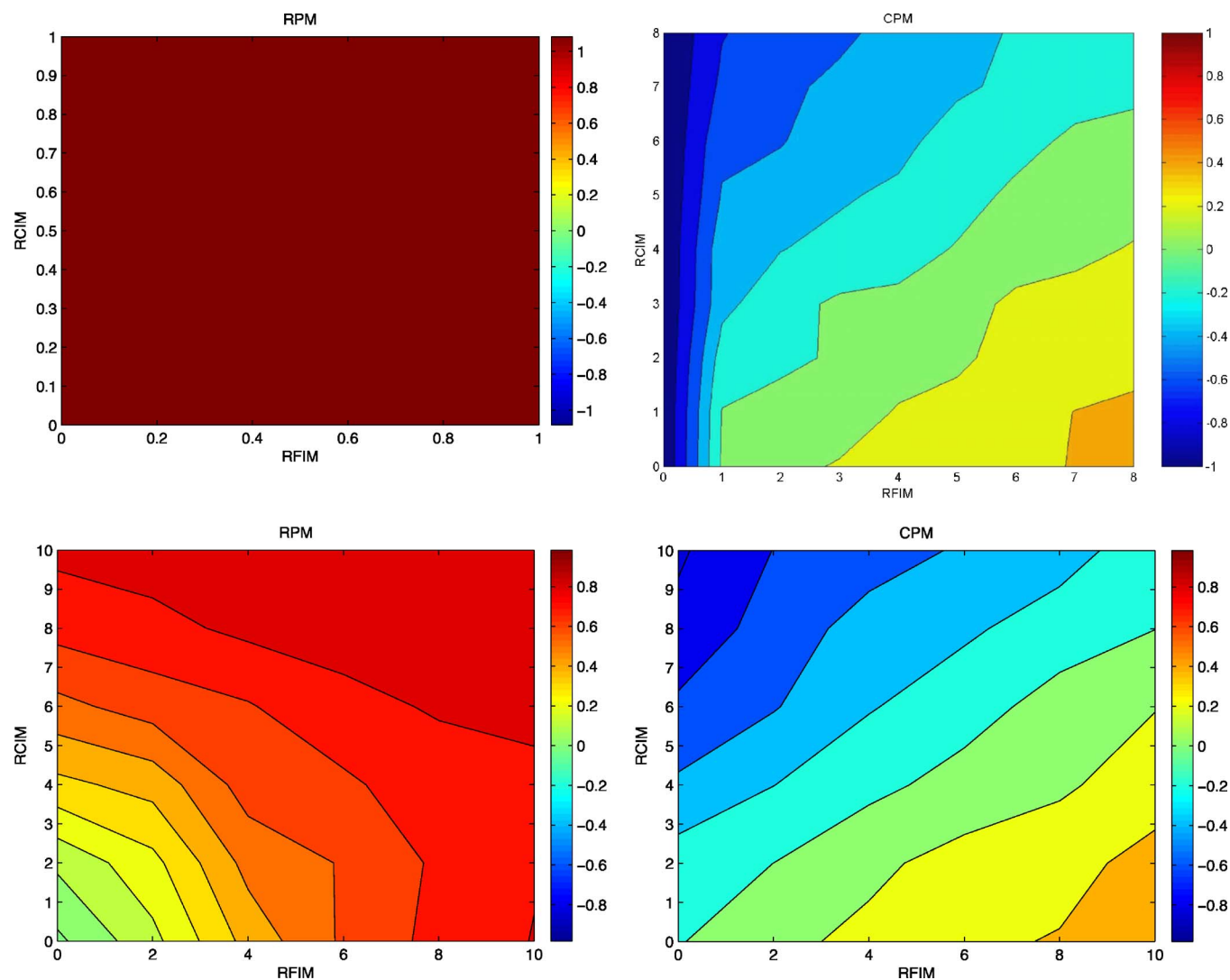


FIG. 21. (Color online) Contour plots of the calculated RPM and CPM values for the simplified RCIM plus RFIM simulation. The RPM values are shown on the left and the CPM values are shown on the right; the  $T=0$  values are shown on the top and the  $T=0.1$  values are shown on the bottom. The random coercivity disorder is plotted vertically and the random field disorder is plotted horizontally.

does not possess spin-inversion symmetry, the random field can only drive the system toward positive correlation. Both of these compete to determine the sign and magnitude of the correlation coefficients. In the range where the contributions from the RCIM and RFIM are roughly equal, the CPM is uncorrelated while the RPM increases with the magnitude of each.

Although we have used a very simple discrete-spin simulation done on a  $64 \times 64$  grid of dipolar Ising spins, note that we obtain very similar behavior to that produced by our much more sophisticated and realistic model presented earlier.

### B. Model 2: RAIM plus LLG dynamics

There is another fundamental explanation for the observed RPM-CPM asymmetry.<sup>26</sup> Even when the Hamiltonian is constructed to possess spin-inversion symmetry, the dynamics describing how the magnetization changes does not

have to be symmetric. In fact, the dynamics of the standard Landau-Lifschitz-Gilbert equation breaks spin-inversion symmetry:

$$\frac{ds}{dt} = -\mathbf{s} \times (\mathbf{B} - \gamma \mathbf{s} \times \mathbf{B}). \quad (3)$$

The first term describes the velocity with which a spin precesses about the magnetic field. The second term describes the damping of the precessional motion produced as the spin aligns along the magnetic field.

Under LLG dynamics, the spins undergo damped precessional motion about their local magnetic fields. When both the external field and all the spins are reversed, the orientation of each spin and its precession are reversed. The precessional motion of the spins (i.e., their motion perpendicular to their local fields) is not reversed, whereas the relaxational motion (parallel to the local fields) is reversed. As a consequence, for a disordered system, the evolution of the mag-

netic domains when starting from a large negative field is not the mirror image of the evolution starting from a large positive field.

Therefore the spin-inversion symmetry of the Hamiltonian that completely determines the equilibrium static properties does not control the nonequilibrium dynamics that are relevant for magnetic hysteresis. We first observed this effect for a vector spin model using the LLG equations to describe a set of magnetic nanopillars.<sup>26</sup> There we found that the major hysteresis loop was not symmetric under inversion of the applied field and the magnetization despite the fact that the Hamiltonian displayed this symmetry.

Model 2 that we describe below attempts to capture the physics of the magnetic domains in our experimental CoPt layered system and it has many parallels with the scalar approach described for model 1 above. We will assume that (1) the films are disordered on the scales relevant to pattern formation, but are strongly anisotropic; (2) the easy axis has small random deviations away from the direction perpendicular to the film.

From electron micrographs of similar sputtered films, we see that the layers become increasingly rough and nonplanar as the disorder is increased.<sup>13</sup> Consequently, even though the physics of the perfect material dictates a strong anisotropy, the local direction of the easy axis will no longer be precisely perpendicular to the film. Because it varies randomly in space, we write the anisotropic contribution to the Hamiltonian as

$$\mathcal{H}_{\text{ani}} = -\alpha \sum_i (\mathbf{s}_i \cdot \hat{\mathbf{n}}_i)^2, \quad (4)$$

where  $\alpha$  is a model parameter. Higher-order corrections that are even in  $s_i$  are also possible, but they are not necessary to obtain qualitative agreement with our experiments.

Disorder is included through random variation in the easy axis  $\hat{\mathbf{n}}_i$  for each block of spins. To adjust the effects of the disorder, a weighting factor  $w_{\text{ani}}$  was included that controls the variation from the perpendicular axis. For small values of  $w_{\text{ani}}$  the variation is small and there is little disorder. At larger values, the disorder is heavily weighted and has a large influence.

We have also included the short-range ferromagnetic coupling  $J$ . Because we are attempting to model this system as a continuum, we take the usual approach of minimizing effects of the grid by writing this ferromagnetic interaction in terms of  $\mathbf{s}_{\mathbf{k}}$ , the Fourier transform of the spins,

$$\mathcal{H}_{\text{el}} = J \sum_{\mathbf{k}} k^2 s_{\mathbf{k}}^2. \quad (5)$$

As in the scalar case, it is also crucial to include the long-range dipolar interaction

$$\mathcal{H}_{\text{dip}} = -w_{\text{dip}} \sum_{i,j \neq i} \frac{3(\mathbf{s}_i \cdot \mathbf{e}_{ij})(\mathbf{e}_{ij} \cdot \mathbf{s}_j) - \mathbf{s}_i \cdot \mathbf{s}_j}{r_{ij}^3}, \quad (6)$$

where  $\mathbf{r}_{ij}$  is the displacement vector between spins  $i$  and  $j$ ,  $\mathbf{e}_{ij}$  is the unit vector along this direction, and  $w_{\text{dip}}$  represents the strength of the dipolar coupling.

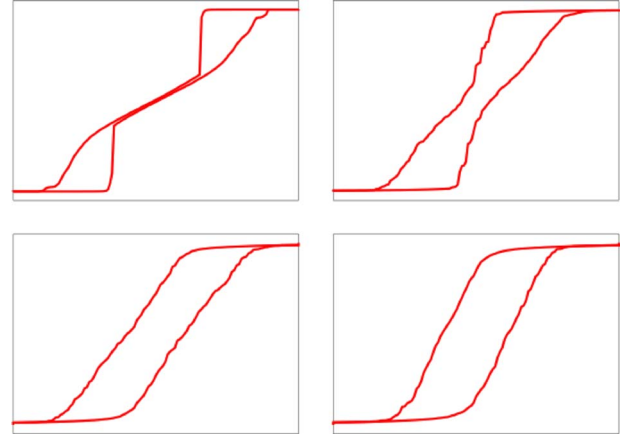


FIG. 22. (Color online) Simulated evolution of the major hysteresis loops versus the disorder for model 2. Note that this behavior qualitatively agrees with that of the experimental samples shown in Fig. 6.

Although this is correct for point dipoles, we are modeling blocks of spins and must include this effect in this interaction. In particular, the short-range behavior is smoothed out by integration in the vertical direction.<sup>28</sup> We implement this as a  $k$ -space cutoff by multiplying the dipolar interaction in  $k$  space by a Gaussian  $\exp(-k^2 d^2/2)$  where  $d$  is a parameter comparable to the thickness of the sample.

Finally, we include the usual interaction with the external field

$$\mathcal{H}_{\text{ext}} = -B_e \sum_i s_i^z. \quad (7)$$

All of the terms in the Hamiltonian are bilinear in the spins and the external field but, as discussed above, the LLG equations are not. Because of the symmetry breaking produced by the LLG dynamics, model 2 can be tuned to produce a small RPM-CPM symmetry breaking similar to that measured by our experiments.

We have chosen the relaxation time to be of the order of the precessional period near saturating fields, that is,  $\gamma=1$ . Although this quantity has not been measured for our CoPt films, it has been measured for other similar materials. Experiments on NiFe films show that it is very large, approximately 100.<sup>29</sup> If it were so large in our CoPt system, it would only accentuate the memory asymmetry further. Work on CoCrPt systems<sup>30</sup> has indicated that the precessional period is comparable to the relaxation time and if this is also true for our films, then our  $\gamma=1$  assumption is reasonable.

Summarizing model 2, we have coarse-grained vector spins evolving via the LLG equations with thermal noise. The Hamiltonian incorporates local ferromagnetic coupling, long-range dipolar forces, disordered anisotropy modeled by a random easy axis, and coupling to the external field. We found a range of model parameters that produced comparable behavior to that of our experimental samples.

First, we examine the evolution of the major hysteresis loops versus the disorder. The evolution of the simulated major loops is shown in Fig. 22. The disorder increases from



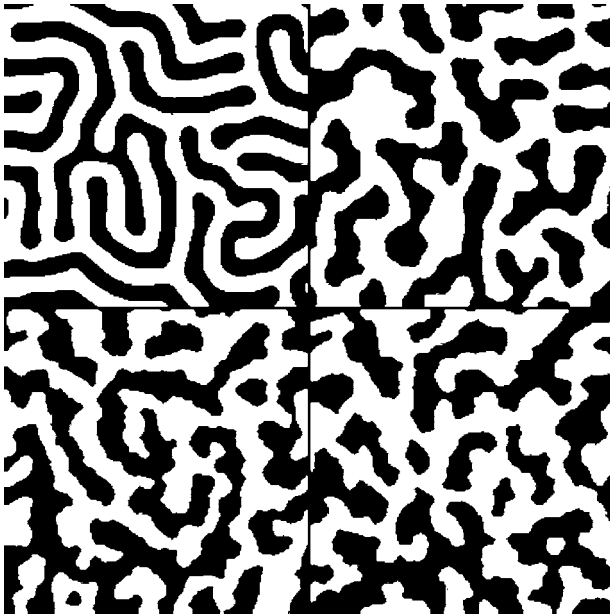


FIG. 23. Simulated evolution of the domain configurations versus the disorder for model 2. Note that this behavior qualitatively agrees with that of the experimental samples as shown in Fig. 5. The anisotropy disorder weighting parameters  $w_{\text{ani}}$  are 0.001, 0.091, 0.24, and 0.33, while the dipole strengths  $w_{\text{dip}}$  are 0.15, 0.105, 0.08, and 0.06, respectively.

left to right and from top to bottom; the simulated loop shape for the lowest disorder is shown in the upper left panel and the simulated loop shape for the highest disorder is shown in the lower right panel.

The simulated domain configurations for different amounts of disorder at a finite temperature are shown in Fig. 23. Again the disorder increases from left to right and from top to bottom. The evolution of our simulated domain configurations versus disorder qualitatively agrees with that observed in the experimental samples.

For low disorder when lowering the external field from saturation, our simulations show that there is suddenly spontaneous growth of domain lines that fill up the system at a

critical value of the field; this happens at constant field. For our simulations with low disorder the domain morphology looks labyrinthine at remanence. The simulated morphology and growth of the domains are very similar to those of our experiments.

For low disorder, the simulated hysteresis loops look quite similar to those for the 3 mTorr samples: corresponding to the onset of domain growth in the simulation, there is a cliff in the hysteresis loop because the magnetization decreases substantially during this phase of growth. When the disorder is high, it pins the domains by destroying translational invariance. This happens suddenly in our simulations in a similar fashion as that in the experiments, suggesting a critical disorder.<sup>2</sup> For this critical disorder and above, the spontaneous cliff-producing growth of the domains disappears, and the domains at remanence no longer look labyrinthine, but instead are much more disordered. After losing their clifflike shape, the simulated hysteresis loops are smooth. The qualitative similarities between the experimental major loops and the simulated major loops for model 2 can be seen by a comparison of Figs. 22 and 6.

We explored the memory effects in model 2 by calculating the correlation between pairs of domain configurations. Because we had direct access to the complete domain configurations, we calculated the correlations in real space. The simulated RPM and CPM values for model 2 at the coercive point as a function of the disorder are shown in Fig. 24. The RPM-CPM symmetry breaking is clearly visible. As the temperature is increased, both curves lower in value but the RPM curve still remains slightly above the CPM curve. These curves clearly grow rapidly past the critical disorder point where the simulated and experimental loops change from clifflike to smooth.

The observed memory behavior in model 2 can be explained as follows. For low disorder, the spontaneous growth of the domains is very susceptible to thermal fluctuations. If we observe the growth of the domains for several cycles around the major loop, we find that, although the initial nucleation points are precisely the same, the evolution past that point is different every time. For low disorder, it appears that the thermal fluctuations produce different domain pat-

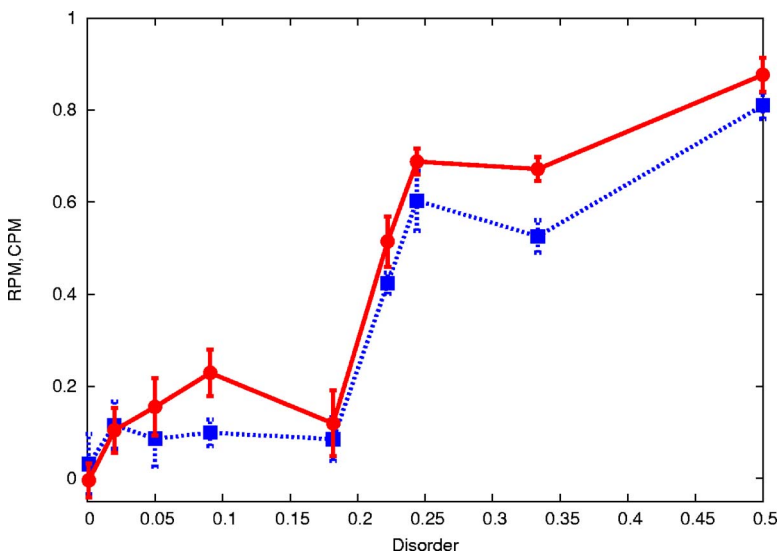


FIG. 24. (Color online) RPM (red circles) and CPM (blue squares) values predicted by model 2 plotted versus the disorder. Note the qualitative agreement with the experimental measurements shown in Fig. 16.

terns during each cycle. However, for high disorder, the pinning produced by the disorder appears to constrain the domain growth and leads to significant similarity from cycle to cycle of the domain configurations at the coercive point.

In summary, model 2 simulated CoPt thin films using a spin-symmetric Hamiltonian with LLG dynamics. Unlike in our other scalar models, the LLG vector *dynamics* is the mechanism for breaking the RPM and CPM symmetry. In addition to this asymmetry, model 2 was also able to successfully simulate both the major hysteresis loops and the evolution of the domain configurations in qualitative agreement with our experimental results.

### C. Model 3: A spin-glass model plus the RFIM

Motivated by the above experimental and theoretical results, we attempted to determine the minimal model that would capture the essential physics of the observed memory effects. In this section, we explore the following four questions: (1) What is the minimal model that exhibits these memory effects? (2) Do these memory effects persist at finite temperatures? (3) How do these memory effects depend on the disorder? and (4) Does the RPM-CPM symmetry breaking convincingly exceed the error bars? We assert that it is of general interest to study the RPM and CPM for simple paradigmatic models, such as the Edwards-Anderson Ising spin glass and the RFIM.<sup>2,31</sup>

#### 1. Ingredient 1: Edwards-Anderson spin glass

We start with the Hamiltonian for the Edwards-Anderson<sup>32</sup> spin glass given by

$$\mathcal{H}_{\text{EASG}} = - \sum_{\langle i,j \rangle} J_{ij} S_i S_j - H \sum_i S_i. \quad (8)$$

The spins  $S_i = \pm 1$  lie on the vertices of a square lattice in two dimensions (2D) of size  $N=L^2$  with periodic boundary conditions. The interactions  $J_{ij}$  are Gaussian distributed with zero mean and standard deviation  $\sigma_J$ . Our simulations were performed by first saturating the system by applying a large external field  $H$  and then reducing  $H$  in small steps to reverse the magnetization.

For finite temperatures, we performed a Monte Carlo simulation and equilibrated until the average magnetization was independent of time for each field step. For zero temperature, we used Glauber dynamics<sup>33</sup> where randomly chosen unstable spins—pointing against their local field  $h_i = \sum_{\langle i,j \rangle} J_{ij} S_j + H$ —were flipped until all spins were stable for each field step. These simulations converged rapidly and showed essentially no size dependence past  $L=20$ .

We quantified the simulated RPM and CPM with  $\rho_r(H)$ , the overlap in real space of the spin configuration at a field  $H$  with the configuration at a field with the same magnitude  $|H|$  after an  $n=1/2$  cycle for CPM and  $n=1$  cycle for RPM

$$\rho_r(H) = \frac{(-1)^{2n}}{N} \sum_{i=1}^N S_i(H) S_i^{(n)}(H). \quad (9)$$

Our results for the EASG show that this system exhibits nearly complete RPM and CPM throughout the entire field

range for  $T=0$ . The strong CPM can be attributed to the spin-inversion symmetry of the system: upon reversing all spins  $S_i$  and the magnetic field  $H$ , the Hamiltonian transforms into itself. The observation of robust RPM and CPM answers question 1 by establishing the EASG as a minimal model displaying these memory effects. However, the simulated memory effects were not perfect even at  $T=0$ . This was probably due to the stochastic nature of the updating: during each field sweep, the spins were selected randomly for updating. Therefore, even at  $T=0$ , the spin configurations did not evolve entirely along the same valleys of the energy landscape. Our simulations at finite temperatures show that the RPM and CPM decreased with increasing temperature and remained finite, even though it would seem natural for the thermal fluctuations to completely wash out the microscopic memory, rendering it macroscopic only.

By varying the disorder strength  $\sigma_J$  in our EASG model we showed that the RPM and CPM increase dramatically with increasing disorder, in good agreement with the experiments. The physical reason behind this result lies in the fact that when the disorder is high the energy landscape develops a few preferable valleys and the system evolves along these optimal valleys. This is not the case for small disorder where several comparable shallow valleys without a single optimal path are present. Finally, in relation to question 4 it is noted that in the EASG the differences between the RPM and CPM are immeasurably small.

#### 2. Ingredient 2: Pure random field Ising model

Next, we study the same memory effects in the 2D random field Ising model

$$\mathcal{H}_{\text{RFIM}} = -J \sum_{\langle i,j \rangle} S_i S_j - \sum_i [H + h_i] S_i; \quad (10)$$

here the random fields  $h_i$  were chosen from a Gaussian distribution with zero mean and standard deviation  $\sigma_h$  ( $J=1$ ). The main differences between the RFIM and the EASG are that the RFIM does not have frustration and does not have spin-inversion symmetry. We find that this RFIM model also shows memory effects that are again stable with respect to thermal fluctuations.

Regarding question 4, the RFIM deviates from the EASG results and correlates with the experiments: in the RFIM, the RPM and CPM are different. The RPM is larger than the CPM for all temperatures due to the lack of spin-inversion symmetry in the Hamiltonian. For intermediate to large values of the disorder, the CPM is negligible and, in the proximity of the coercive field, the CPM correlation is even negative. In contrast, the RPM is large in the RFIM. In particular, for  $T=0$  the RPM is perfect due to the “no-crossing property” of the RFIM.<sup>34</sup> Consequently, the RPM-CPM symmetry breaking is large over much of the parameter space. Just as for the EASG, the RFIM memory increases due to the valleys in the energy landscape becoming more pronounced with increasing disorder.

#### 3. Combined spin-glass model plus the RFIM

Because of the way that our simulations for the pure EASG model and for the pure RFIM do not agree with the

experiments, the following question immediately arises: Can a combined EASG and RFIM yield results comparable to the experiments—increasing memory with increasing disorder, together with the RPM-CPM symmetry breaking?

In order to test this, we introduced random fields into the EASG that act only on a small fraction (5%) of the spins in order to break the spin-inversion symmetry of the Hamiltonian [Eq. (8)]:

$$\mathcal{H}_{\text{SG+RF}} = - \sum_{\langle i,j \rangle} J_{ij} S_i S_j - \sum_i [H + h_i] S_i. \quad (11)$$

The random bonds  $J_{ij}$  were chosen from a Gaussian distribution with zero mean and standard deviation  $\sigma_J$ . The random fields were chosen from a Gaussian distribution with zero mean and standard deviation unity.

Since the dipolar interactions in our perpendicular anisotropy films are antiferromagnetic, they introduce extensive frustration into the system; this is the key ingredient for spin glasses. Our experimental system also contains several possible sources of random fields: spins frozen in by the local shape anisotropies produced by the locally deformed environments, unusually large crystal-field anisotropies, or by frozen-in reversed bubbles, as reported in the same experimental system by Davies *et al.*<sup>15</sup> Consequently, it is easy to imagine that all of the necessary ingredients for the combined EASG plus RFIM are likely to be present in our experimental samples. Results from Model 3 are shown in Fig. 25 and clearly resemble the experimental results presented earlier.

#### 4. Summary for model 3

We now summarize our results for model 3. We have found that our pure EASG model, our pure RFIM, and our combined EASG model plus RFIM all exhibit both RPM and CPM, in which both memory effects persist to finite temperatures and both memory effects increase with increasing disorder. For our pure EASG model, the simulated RPM and CPM are identical because of the spin-inversion symmetry. For our pure RFIM, the RPM is always much larger than the CPM because of the lack of spin-inversion symmetry. Our combined EASG and RFIM, a spin glass with diluted random fields that break the spin-inversion symmetry, reproduces the essential experimental results—it exhibits both RPM and CPM, both memory effects increase with increasing disorder, and the model can be tuned so that the RPM is a little bit larger than the CPM. All of these properties are present in Fig. 25. It will be exciting to see if experimentally realizable spin-glass systems can be shown to have these properties.

## VII. CONCLUSIONS

Our experimental results represent direct measurements of the effects of controlled microscopic disorder on the magnetic memory of an ensemble of magnetic domains in such perpendicular magnetic materials. We identified and studied three different aspects of the domain-level memory: microscopic return-point memory, microscopic complementary-

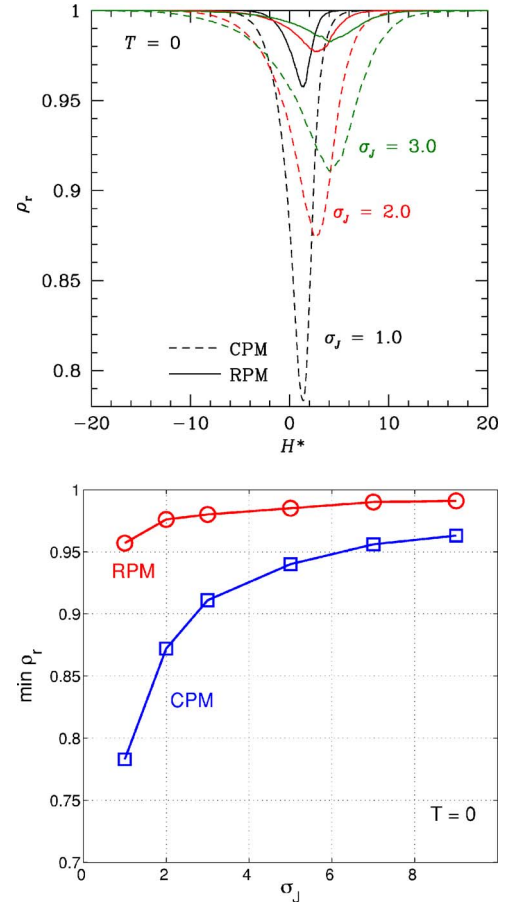


FIG. 25. (Color online) RPM and CPM values predicted by model 3. The field dependence for model 3 is shown in the top panel where the predicted RPM values (solid lines) and CPM values (dashed lines) are shown for different disorder strengths. The disorder dependence for model 3 at the coercive point is shown in the bottom panel. Note that both memory effects increase with increasing disorder and that the RPM (red circles) is always larger than the CPM (blue squares), in agreement with the experiments shown in Fig. 16. The error bars are the size of the symbols and thus have been neglected.

point memory, and microscopic half-loop memory. Because our experimental observations could not be described by any existing microscopic-disorder-based theory, we developed theories that do account for the behavior of our experimental system. Our combined experimental and theoretical work sets benchmarks for future work.

We found a very rich behavior of these memory properties in our system of perpendicular-anisotropy multilayer CoPt samples. At the domain level, we found disorder-induced partial RPM and CPM, and we also found a small RPM-CPM symmetry breaking where the RPM was consistently slightly larger than the CPM.

At the domain level, we found that the HLM versus the sample magnetization was very similar for all of our samples. There was only a subtle effect—the low-disorder samples had slightly higher microscopic HLM than the high-disorder samples. It was surprising to us that the HLM effects were nearly sample independent whereas the RPM and CPM effects were extremely sample dependent.

Our observed RPM and CPM are independent of the number of major loops separating the pairs of magnetic speckle fingerprints. This shows that the deterministic components of the RPM and CPM are essentially stationary, and implies that the deterministic memory in our system is largely reset by bringing the sample to saturation. It also strongly suggests that the same disorder is producing both the deterministic RPM and CPM.

Our measured RPM is consistently higher than our CPM. This slightly broken symmetry imposes severe limitations on the possible theoretical models. The evolution of the RPM and CPM with disorder is also very interesting. Both the RPM and CPM have their largest values just after the initial domain nucleation takes place and then diminish toward a minimum as saturation is approached. At room temperature, the memory is imperfect—the maximum measured RPM and CPM values are less than 1. We suspect that this is due to the thermal fluctuations in our samples, but have not yet demonstrated this experimentally.

As we increase the disorder in our samples, there is initially little change in the memory, then at the same level of disorder there is a rapid increase in both the RPM and the CPM, followed by apparent plateaus with the RPM slightly larger than the CPM. This is reminiscent of the disorder-induced transition predicted by the Sethna *et al.* RFIM work where the major-loop shape changes from a gradual loop to a sharp loop at a critical value of the disorder. At the corresponding critical disorder transition in our system, our loops also change shape, but more interestingly, and perhaps more importantly, both the RPM and CPM suddenly jump from zero to their maximum values.

Two possible explanations for RPM being greater than the CPM in the disordered samples have been presented. Within the current experimental framework, it is not possible to determine which of these two methods is a more accurate description of our system.

There are potential physical mechanisms that would introduce random fields into our samples. Due to defects in the disordered samples, quenched spins may be present that do not reverse their direction even under the highest magnetic fields we were able to apply. In effect, even though the

major-loop hysteresis curve appears to be constant and unchanging, there may still be spins which persist in their original direction. These could be due to large crystal anisotropy, shape anisotropy because of the rough interfaces, or small, persistent magnetic bubbles due to incomplete saturation. In order to test for this scenario, it would be necessary to repeat the RPM and CPM measurements after saturating the samples under very high applied fields sufficient to saturate even the most stubborn spins.

In contrast, our dynamical model does not require the existence of these random fields. Instead it requires precessional motion to be present in the system. We know that spins precess in the presence of a magnetic field. However, we do not know the extent of precession relative to damping. Measurements of the ratio of the precessional and damping terms off the LLG equation on similar systems<sup>29,30</sup> have shown that precessional motion is quite significant. More experiments will be necessary to determine if this is also the case for Co/Pt multilayer films. These two suggested experiments, study under very high applied fields and determination of the precessional to damping ratio, should shed light on the true mechanism for spin-inversion symmetry breaking in this system.

There are very few direct, detailed studies of microscopic RPM, CPM, and HLM in either longitudinal or perpendicular magnetic materials and even fewer domain-level ensemble studies of such properties. It will be extremely interesting to see what our coherent x-ray speckle metrology technique—together with our complementary x-ray magnetic microscopy studies—will teach us about the domain-level-ensemble memory in both of these technologically important and scientifically fascinating magnetic memory systems.

#### ACKNOWLEDGMENTS

We gratefully acknowledge the support of our work by the U.S. DOE via Grants No. DE-FG02-04ER46102, No. DE-FG06-86ER45275, and No. DE-AC03-76SF00098, by the NSF via Grant No. EAR-0216346, by the American Chemical Society via Grant No. ACS-PRF 43637-AC10, and via the Alfred P. Sloan Foundation (K.L.).

<sup>1</sup>M. S. Pierce, R. G. Moore, L. B. Sorensen, S. D. Kevan, O. Hellwig, E. E. Fullerton, and J. B. Kortright, *Phys. Rev. Lett.* **90**, 175502 (2003).

<sup>2</sup>J. P. Sethna, K. A. Dahmen, and O. Perkovic, in *The Science of Hysteresis*, edited by G. Bertotti and I. Mayergoyz (Academic Press, San Diego, 2006), Vol. II, Chap. 2.

<sup>3</sup>G. Durin and S. Zapperi, in *The Science of Hysteresis* (Ref. 2), Vol. II, Chap. 3.

<sup>4</sup>G. Durin and S. Zapperi, *Phys. Rev. Lett.* **84**, 4705 (2000).

<sup>5</sup>Recently a number of groups have developed optical-microscopy-based Barkhausen apparatuses. See, for example, S. Yang and J. L. Erskine, *Phys. Rev. B* **72**, 064433 (2005); E. Puppini, *Proc. SPIE* **5843**, 23 (2004); D. H. Kim *et al.*, *ibid.* **5843**, 40 (2004); A. Schwartz and M. Liebmann, *ibid.* **5843**, 52 (2004); K.

Szielasko *et al.*, *ibid.* **5892**, 105 (2004); O. M. Korpusov *et al.*, *J. Magn. Magn. Mater.* **272-276**, 2035 (2004); and references therein. However, because these instruments use visible light, they cannot be used to study the suboptically-sized magnetic domains in our samples or in modern magnetic media.

<sup>6</sup>There has been some interesting work on memory properties, magnetic domains, and reversal done in different systems by very different techniques. For a microscopy study, see J. Ferré, V. Grolier, P. Meyer, S. Lemerle, A. Maziewski, E. Stefanowicz, S. V. Tarasenko, V. V. Tarasenko, M. Kisielewski, and D. Renard, *Phys. Rev. B* **55**, 15092 (1997). For memory properties studied with magnetic wave forms, see J. R. Hoinville, R. S. Indeck, and M. W. Muller, *IEEE Trans. Magn.* **28**, 3398 (1992).

<sup>7</sup>K. De'Bell, A. B. MacIsaac, and J. P. Whitehead, *Rev. Mod.*

- Phys. **72**, 225 (2000).
- <sup>8</sup>E. R. Madelung, Ann. Phys. **17**, 861 (1905); Phys. Z. **13**, 486 (1912).
- <sup>9</sup>F. Preisach, Z. Phys. **94**, 277 (1935). For more recent work, see I. D. Mayergoyz and G. Friedman, J. Appl. Phys. **61**, 4022 (1987); I. D. Mayergoyz, A. A. Adly, and G. Friedman, *ibid.* **67**, 5373 (1990).
- <sup>10</sup>S. E. Zirka and Y. I. Moroz, IEEE Trans. Magn. **31**, 3509 (1995); **35**, 2090 (1999); S. E. Zirka, Y. I. Moroz, and E. Della Torre, *ibid.* **41**, 2426 (2005).
- <sup>11</sup>M. S. Pierce, C. R. Buechler, L. B. Sorensen, J. J. Turner, S. D. Kevan, E. A. Jagla, J. M. Deutsch, T. Mai, O. Narayan, J. E. Davies, K. Liu, J. H. Dunn, K. M. Chesnel, J. B. Kortright, O. Hellwig, and E. E. Fullerton, Phys. Rev. Lett. **94**, 017202 (2005).
- <sup>12</sup>B. Hu, P. Geissbuhler, L. B. Sorensen, S. D. Kevan, E. E. Fullerton, and J. B. Kortright, Synchrotron Radiat. News **14**, 11 (2001).
- <sup>13</sup>E. E. Fullerton, J. Pearson, C. H. Sowers, S. D. Bader, X. Z. Wu, and S. K. Sinha, Phys. Rev. B **48**, 17432 (1993).
- <sup>14</sup>O. Hellwig, G. Denbeau, J. B. Kortright, and E. E. Fullerton, Physica B **336**, 136 (2003).
- <sup>15</sup>J. E. Davies, O. Hellwig, E. E. Fullerton, G. Denbeaux, J. B. Kortright, and Kai Liu, Phys. Rev. B **70**, 224434 (2004).
- <sup>16</sup>C. Kooy and C. Enz, Philips Res. Rep. **15**, 7 (1960).
- <sup>17</sup>J. Miao, Y. Nishino, Y. Kohmura, B. Johnson, C. Song, S. H. Risbud, and T. Ishikawa, Phys. Rev. Lett. **95**, 085503 (2005); J. W. Miao, H. N. Chapman, J. Kirz, D. Sayre, and K. O. Hodgson, Annu. Rev. Biophys. Biomol. Struct. **33**, 157 (2004), and references therein.
- <sup>18</sup>S. Eisebitt, J. Lüning, W. F. Schlotter, M. Lörger, O. Hellwig, W. Eberhardt, and J. Stöhr, Nature (London) **432**, 885 (2004); O. Hellwig, S. Eisebitt, W. Eberhardt, J. Lüning, W. F. Schlotter, and J. Stöhr, J. Appl. Phys. **99**, 08H307 (2006).
- <sup>19</sup>C. C. Retsch and I. McNulty, Phys. Rev. Lett. **87**, 077401 (2001).
- <sup>20</sup>P. Fischer, T. Eimüller, G. Schütz, G. Denbeaux, A. Pearson, L. Johnson, D. Attwood, S. Tsunashima, M. Kumazawa, N. Takagi, M. Köhler, and G. Bayreuther, Rev. Sci. Instrum. **72**, 2322 (2001).
- <sup>21</sup>For the RAIM, see, for example, E. Vives and A. Planes, Phys. Rev. B **63**, 134431 (2001).
- <sup>22</sup>For the RBIM see E. Vives and A. Planes, J. Magn. Magn. Mater. **221**, 164 (2000).
- <sup>23</sup>For the RCIM see O. Hovorka and G. Friedman, cond-mat/0306300 (unpublished).
- <sup>24</sup>E. A. Jagla, Phys. Rev. E **70**, 046204 (2004).
- <sup>25</sup>E. A. Jagla, Phys. Rev. B **72**, 094406 (2005).
- <sup>26</sup>J. M. Deutsch, T. Mai, and O. Narayan, Phys. Rev. E **71**, 026120 (2005); J. M. Deutsch and T. Mai, *ibid.* **72**, 016115 (2005).
- <sup>27</sup>H. G. Katzgraber and G. T. Zimányi, Phys. Rev. B **74**, 020405(R) (2006).
- <sup>28</sup>S. A. Langer, R. E. Goldstein, and D. P. Jackson, Phys. Rev. A **46**, 4894 (1992).
- <sup>29</sup>G. M. Sandler, H. N. Bertram, T. J. Silva, and T. M. Crawford, J. Appl. Phys. **85**, 5080 (1999).
- <sup>30</sup>A. Lyberatos, G. Ju, R. J. M. van de Veerdonk, and D. Weller, J. Appl. Phys. **91**, 2236 (2002).
- <sup>31</sup>K. Binder and A. P. Young, Rev. Mod. Phys. **58**, 801 (1986); N. Kawashima and H. Rieger, in *Frustrated Spin Systems*, edited by H. T. Diep (World Scientific, 2005), Chap. 9, p. 491.
- <sup>32</sup>S. F. Edwards and P. W. Anderson, J. Phys. F: Met. Phys. **5**, 965 (1975).
- <sup>33</sup>H. G. Katzgraber, F. Pázmándi, C. R. Pike, K. Liu, R. T. Scalettar, K. L. Verosub, and G. T. Zimányi, Phys. Rev. Lett. **89**, 257202 (2002).
- <sup>34</sup>A. A. Middleton, Phys. Rev. Lett. **68**, 670 (1992).

# Michael Faraday Quotes

## On his discovery of induction:

**Queen Victoria:** "But Mr. Faraday, of what use is it?"

**Michael Faraday:** "But Your Highness, of what use is a newborn baby?"

**William Gladstone:** "But what is the use of it?"

**Michael Faraday:** "One day sir you may tax it."

## On science:

**"Nothing is too wonderful to be true."**

## **Random Walk Applets**

<http://math.furman.edu/~dcs/java/rw.html>

<http://polymer.bu.edu/java/java/2drw/RandWalk2D.html>

<http://www.rbyter.com/java/randomWalkDescription.html>

## **Ising Model Applets**

<http://physics.ucsc.edu/~peter/ising/ising.html>

<http://www.pha.jhu.edu/~javalab/ising/ising.html>

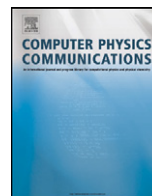
<http://www.ibiblio.org/e-notes/Perc/ising.htm>

<http://www-reynal.ensea.fr/applets/spin-models/en/afising.html>



Contents lists available at ScienceDirect

## Computer Physics Communications

[www.elsevier.com/locate/cpc](http://www.elsevier.com/locate/cpc)

## Simulating spin models on GPU

Martin Weigel

Institut für Physik, KOMET 331, Johannes Gutenberg-Universität Mainz, Staudinger Weg 7, 55128 Mainz, Germany

## ARTICLE INFO

## Article history:

Received 18 June 2010

Accepted 29 October 2010

Available online xxxx

## Keywords:

Monte Carlo simulations

GPU

Spin models

## ABSTRACT

Over the last couple of years it has been realized that the vast computational power of graphics processing units (GPUs) could be harvested for purposes other than the video game industry. This power, which at least nominally exceeds that of current CPUs by large factors, results from the relative simplicity of the GPU architectures as compared to CPUs, combined with a large number of parallel processing units on a single chip. To benefit from this setup for general computing purposes, the problems at hand need to be prepared in a way to profit from the inherent parallelism and hierarchical structure of memory accesses. In this contribution I discuss the performance potential for simulating spin models, such as the Ising model, on GPU as compared to conventional simulations on CPU.

© 2010 Published by Elsevier B.V.

## 1. Introduction

Owing to a combination of an improved toolset of simulational machinery and methods of data analysis and the exponential increase in available computer power observed over the past four decades, computer simulations such as the Monte Carlo method have at least drawn level with the more traditional perturbative approaches for studying a plethora of problems in statistical physics [1], ranging from critical phenomena [2] over the physics of disordered systems [3] to soft matter and biological problems [4]. This success notwithstanding, a range of notoriously hard problems appear to create an insatiable appetite for more powerful computational devices to finally settle a number of long-standing questions. Among such problems are, for instance, the quest of understanding the nature of the spin glass phase [5] or the protein folding problem. To achieve results beyond the reach of the available standard computational resources of the time, there has been a tradition of designing special purpose computers, e.g., for calculations in lattice field theory [6] or the simulation of spin models [7,8].

Since the design and programming of such dedicated machines regularly require a large effort in terms of monetary and human resources, recently scientists have started to adopt the use of graphics processing units for general purpose computational tasks in the hope of harvesting their nominally vast computational power, on par with some devices based on FPGAs, without the need of time-consuming work at and near the hardware level [9–11]. By design, GPUs are optimized for manipulating a large number of graphics primitives in parallel, which often amounts to simple, floating-point matrix calculations. In contrast to current CPUs, they are

not designed to cope with “unexpected” branches in the code, or for executing a single-threaded program as fast as possible. While this makes GPUs not well suited as drop-in replacements for CPUs for interactive computing, their highly parallel architecture might well be taken advantage of in scientific calculations with an often high degree of vectorizable or parallelizable code. Their original design for graphics calculations, however, entails certain design features which are not necessarily optimal for scientific computational tasks, such as a special hierarchy of memory organization or a restriction to (efficient) floating-point calculations only in single precision arithmetics, which only has been alleviated in the very latest generation of cards.

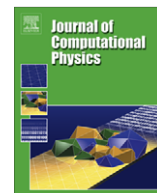
While the first applications of general purpose computing on GPUs were performed directly in graphics programming languages such as OpenGL [9], access to these devices for scientific applications has been considerably simplified with the advent of language extensions such as NVIDIA CUDA [12] and OpenCL [13] for performing general purpose computing on GPUs. The application presented here was coded on the NVIDIA architecture using the CUDA framework, which is a high-level extension to the C language family.

## 2. Relevant features of GPU architecture

Fig. 1 shows a schematic representation of the NVIDIA GPUs used in the work presented here. A GPU consists of a number of multiprocessors, each composed of a number of single processing units which concurrently work with the same code on different parts of a common data set. Of utmost importance to the efficient performance of GPU programs is the organization of GPU memory, which comes in a number of flavors:

E-mail address: [weigel@uni-mainz.de](mailto:weigel@uni-mainz.de).





# GPU accelerated Monte Carlo simulation of the 2D and 3D Ising model <sup>☆</sup>

Tobias Preis <sup>a,b,\*</sup>, Peter Virnau <sup>a</sup>, Wolfgang Paul <sup>a</sup>, Johannes J. Schneider <sup>a</sup>

<sup>a</sup> Department of Physics, Mathematics and Computer Science, Johannes Gutenberg University of Mainz – Staudinger Weg 7, D-55099 Mainz, Germany

<sup>b</sup> Artemis Capital Asset Management GmbH – Gartenstr. 14, D-65558 Holzheim, Germany

## ARTICLE INFO

### Article history:

Received 9 December 2008

Received in revised form 11 March 2009

Accepted 12 March 2009

Available online 25 March 2009

### MSC:

65Z05

65C05

82C20

### Keywords:

Monte Carlo simulation

GPU computing

Ising model

Phase transition

Finite size scaling

## ABSTRACT

The compute unified device architecture (CUDA) is a programming approach for performing scientific calculations on a graphics processing unit (GPU) as a data-parallel computing device. The programming interface allows to implement algorithms using extensions to standard C language. With continuously increased number of cores in combination with a high memory bandwidth, a recent GPU offers incredible resources for general purpose computing. First, we apply this new technology to Monte Carlo simulations of the two dimensional ferromagnetic square lattice Ising model. By implementing a variant of the checkerboard algorithm, results are obtained up to 60 times faster on the GPU than on a current CPU core. An implementation of the three dimensional ferromagnetic cubic lattice Ising model on a GPU is able to generate results up to 35 times faster than on a current CPU core. As proof of concept we calculate the critical temperature of the 2D and 3D Ising model using finite size scaling techniques. Theoretical results for the 2D Ising model and previous simulation results for the 3D Ising model can be reproduced.

© 2009 Elsevier Inc. All rights reserved.

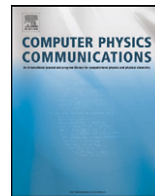
## 1. Introduction

The Ising model, which is named after Ising [1], is a standard model of statistical physics and provides a simplified microscopic description of ferromagnetism. It was introduced to explain the ferromagnetic phase transition from the paramagnetic phase at high temperatures to the ferromagnetic phase below the Curie temperature  $T_C$ . A large variety of techniques and methods in statistical physics have originally been formulated for the Ising model and were generalized and adapted to related models and problems [2]. Supported by his results for a one dimensional spin chain, in which no phase transition occurs, Ising initially proposed in his doctoral thesis that there is also no phase transition in higher dimensions which turned out to be a misinterpretation. The Ising model on a two dimensional square lattice with no magnetic field was then analytically solved by Onsager in 1944 [3]. The critical temperature at which a second order phase transition between an ordered and a disordered phase occurs can be determined analytically for the two dimensional model ( $T_C = 2.269185$  [3]). Despite much effort, an analytic solution for the three dimensional Ising model still remains one of the great challenges in statistical physics. However, computer simulations in combination with finite size scaling techniques [4–7] are able to determine  $T_C \sim 4.5115$  [2] and the rest of the phase diagram with good accuracy. Since 1944, the Ising

<sup>☆</sup> The consumer graphics card GeForce GTX 280 from NVIDIA is used as graphics processing unit (GPU).

\* Corresponding author. Address: Department of Physics, Mathematics and Computer Science, Johannes Gutenberg University of Mainz – Staudinger Weg 7, D-55099 Mainz, Germany.

E-mail address: [preis@uni-mainz.de](mailto:preis@uni-mainz.de) (T. Preis).



# Multi-GPU accelerated multi-spin Monte Carlo simulations of the 2D Ising model<sup>☆</sup>

Benjamin Block<sup>\*</sup>, Peter Virnau, Tobias Preis

Department of Physics, Mathematics and Computer Science, Johannes Gutenberg University Mainz, Staudingerweg 7, D-55128 Mainz, Germany

## ARTICLE INFO

### Article history:

Received 17 March 2010  
 Received in revised form 10 May 2010  
 Accepted 17 May 2010  
 Available online 24 May 2010

### Keywords:

Monte Carlo simulation  
 GPU computing  
 Ising model  
 Phase transition  
 Finite size scaling

## ABSTRACT

A Modern Graphics Processing unit (GPU) is able to perform massively parallel scientific computations at low cost. We extend our implementation of the checkerboard algorithm for the two-dimensional Ising model [T. Preis et al., Journal of Chemical Physics 228 (2009) 4468–4477] in order to overcome the memory limitations of a single GPU which enables us to simulate significantly larger systems. Using multi-spin coding techniques, we are able to accelerate simulations on a single GPU by factors up to 35 compared to an optimized single Central Processor Unit (CPU) core implementation which employs multi-spin coding. By combining the Compute Unified Device Architecture (CUDA) with the Message Passing Interface (MPI) on the CPU level, a single Ising lattice can be updated by a cluster of GPUs in parallel. For large systems, the computation time scales nearly linearly with the number of GPUs used. As proof of concept we reproduce the critical temperature of the 2D Ising model using finite size scaling techniques.

© 2010 Elsevier B.V. All rights reserved.

## 1. Introduction

Various scientific disciplines profited by GPU computing in recent years and are reporting impressive speedup factors in comparison to single Central Processor Unit (CPU) core implementations. GPU stands for Graphics Processing Units which are high-performance many-core processors that can be used to accelerate a wide range of applications. In the meantime, significant savings of computing time have been reported by a huge variety of fields: GPU acceleration can be used in astronomy [1] and radio astronomy [2]. Soft tissue simulation [3], algorithms for image registration [4], dose calculation [5], volume reconstruction from X-ray images [6], and the optimization of intensity-modulated radiation therapy plans [7] are examples for the numerous applications in medicine. Furthermore, DNA sequence alignment [8], molecular dynamics simulations [9–11], quantum chemistry [12], multipole calculations [13], density functional calculations [14,15], air pollution modeling [16], time series analysis focused on financial markets [17,18], and Monte Carlo simulations [19–22] benefited from GPU computing. For many applications, the accuracy can be comparable to that of a double-precision CPU implementation, such as in [23]—the latest generation of GPUs support not only single precision but also double precision floating point operations. The adaption of many computational methods is still in progress, e.g. the analysis of switching processes in financial markets [24,25]. Unfortunately, not all algorithms can be ported efficiently onto a GPU architecture. Particularly, serial algorithms are not suited for GPU computing (for an example see e.g. [26]).

Another crucial limitation is the lack of scalability as current programs typically utilize only single GPUs. As graphics processing hardware is targeted at a broad consumer market—the games industry—, graphic cards can be produced at low cost. On the other hand, to keep production costs low, the global memory is not upgradable and typically limited to 1 GB for consumer cards and 4 GB for Tesla GPUs. Using a recent consumer graphics card, we accelerated Monte Carlo simulations of the Ising model [22]. In [22], a 2D square spin lattice of dimension up to  $1024^2$  spins could be processed on a consumer GPU. The Ising model as a standard model of statistical physics provides a simple microscopic description of ferromagnetism [27]. It was introduced to explain the ferromagnetic phase transition from the paramagnetic phase at high temperatures to the ferromagnetic phase below the Curie temperature  $T_C$ . A large variety of techniques and methods in statistical physics have originally been formulated for the Ising model and were generalized and adapted to related models and problems [28]. Due to its simplicity, which can be embodied by the possibility to use trivial parallelization approaches [29], the two-dimensional Ising model is well suited as a benchmark model since its properties are well studied [30–32] and many physical systems belong to the same universality class. The Ising model on a two-dimensional square lattice with no magnetic field was analytically solved

<sup>☆</sup> Source code of our implementations for GPU clusters will be published on <http://www.tobiaspreis.de> after acceptance. In addition, the code can be downloaded from the Google Code project *multigpu-ising*.

<sup>\*</sup> Corresponding author.

E-mail addresses: [lhyamor@gmail.com](mailto:lhyamor@gmail.com) (B. Block), [virnau@uni-mainz.de](mailto:virnau@uni-mainz.de) (P. Virnau), [mail@tobiaspreis.de](mailto:mail@tobiaspreis.de) (T. Preis).